

2014

# Quantum Monte Carlo studies of quantum criticality in low-dimensional spin systems

---

<https://hdl.handle.net/2144/14301>

*"Downloaded from OpenBU. Boston University's institutional repository."*

BOSTON UNIVERSITY  
GRADUATE SCHOOL OF ARTS AND SCIENCES

Dissertation

**QUANTUM MONTE CARLO STUDIES OF QUANTUM CRITICALITY IN  
LOW-DIMENSIONAL SPIN SYSTEMS**

by

**YING TANG**

B.A., Wuhan University, 2007

M.A., Boston University, 2009

Submitted in partial fulfillment of the  
requirements for the degree of  
Doctor of Philosophy

2014

Approved by

First Reader

---

Anders W. Sandvik, Adviser, Ph.D.  
Professor of Physics

Second Reader

---

David K. Campbell, Ph.D.  
Professor of Physics

*For my wonderful parents  
for their constant love and support*

# Acknowledgments

These six years at BU are undoubtedly the most exciting years of my life so far. It is mainly because I have met remarkable people around, who have helped me in many ways to make the completion of this doctoral thesis possible.

First and foremost, I would like to express my immense gratitude to my adviser Prof. Anders Sandvik, for having me involved in interesting research projects and guiding me through my PhD research with unceasing advice, encouragement and support. I am deeply humbled by his broad knowledge in quantum spin systems and great intuition combined with strong technical skills in solving challenging problems. His passion and strong motivation in understanding fundamental science have always stimulated me. He is a great mentor to me. Without Anders's generous help, I would not be able to accomplish my thesis work. I am truly grateful and proud that I have worked with him as his PhD student.

I am also very grateful to have my committee members, Prof David Campbell, Prof Claudio Chamon, Prof Emanuel Katz and Prof Richard Averitt, for their helpful advice and support in my dissertation work through past few years. In addition, I want to thank my group members: Chen Liu, Songbo Jin, Chengwei Liu, Na Xu, Hidemaro Suwa, Ling Wang, Jie Lou and Thomas Lang, for their help and interesting discussions together. I have learned a lot from each of them. I especially want to express my thankfulness to our former postdoctor Arnab Sen for giving me great guidance and triggering my interests in quantum spin systems in my early research years. I also want to express my thanks to my fellow physics friends in the department: Luca D'Alessio, Armin Rahmani, Alex Lang, Javad Noorbakhsh, Kipton Barros, Joel Tenenbaum, Claudia De Grandi, Jingdi Zhang, Wei

Zhang, Xuqing Huang, Kun Gen, Yiming Xu, Xiao Luo, Jiayuan Luo, Wei Li, Duan Wang, Zhiqiang Su, Qian Li, Elsa Abrue and Rachele Dominguez for their friendship and fun time together. It also gives me great pleasure in acknowledging the support and help from all staff members at Boston University. Their dedicated work has provided tremendous support for my PhD study. Especially I want to thank Mirtha Cabello and Winna Somers for their important administrative help, and Guoan Hu for his excellent technical support.

My gratitude goes outside BU community too. I feel very fortunate that I have great collaborators around the world through Anders. In particular, I want to thank Christopher Henley (Cornell University), for his nice collaboration on my first project. I am very impressed by his expertise in the classical dimer model and feel honored to have learned the height model from him. I also want to thank Yu-cheng Lin (National Chengchi University) for her hospitality in hosting me in Taiwan in both 2010 and 2013. I am also grateful for her nice collaboration on the paper about correlated valence-bond states. My gratitude goes to Daoxin Yao (Sun Yet-Sen University) as well, for hosting me at Sun Yet-Sen University for several summers and giving me much encouragement and advice during my study. Furthermore, a special thank-you to Roger Melko (University of Waterloo), who has shown me a very cool and inspiring way of doing physics. I feel very lucky to have learned the algorithm for computing the renyi entanglement entropy from him and his amazing group members, Ann Kallin and Stephen Inglis. I was also very lucky to attend Boulder Summer School in 2010, where I have built great friendship with fun people. I especially want to thank gang member: Ann Kallin, Stephen Inglis, Hyejin Ju, Nan Lin, Yuan-ming Lu, Hongchen Jiang, Bo Yang, Kaiyu Yang, Huaixiu Zheng, Xin Wang for their friendship and support. It is always a great time to have the reunion with the boulder gang and share physics and life together.

My Phd life was made so enjoyable is also due to my friends and groups outside the physics community, who I see as my adopted family in Boston already. Especially, I want to thank Poliana Lemos for always giving me support, understanding and sometimes reminders as a great friend and sister. I am indebted to my lovely roommates: Timothy Li, Huijing

Lin, Manjie Wang and Zhen Wang for giving me sweet times together. My life also has been enriched by the Ruggles Baptist Church and City Outreach Ministry of Chinese Bible Church in Greater Boston. I have received tremendous physical and spiritual support from them. In particular, I want to thank Pastor Juta Pan and Chaoluan Kao, Pastor Larry Showalter and Lois Showalter, Chris and Nanan Coughlin, Fengming Cui, Min Cao, Kerena Huang, Fish Yu, Xiao-lei Tang, Lanhui Chou, Shin-jong Chung, Cynthia Lee, Christine Chan, Jennifer Cheng, Yu-fang Chang, Panle Jia and John Barwick, Mengyao Guo, Ling Li, Erika Cheng, Samuel Chang, En-ping Fu, Albert Chang, Jonathan Leu, Ju Yao, Vickie Chen, Hongying Zhang and Chia-yu Chen for their friendship and fellowship. I am very blessed to have them in my life. I especially want to thank Dr. Chiayu (Cookie) Chen for his company during the final stage of my dissertation work.

Last but not least, I want to thank my family, my father Xiaosu Zhu, mother Yan Tang, stepmother Jianping Gong, auntie Hong Tang, uncle Han Wang, cousin Shu Wang, grandparents Yubin Hu, Xiulan Huang and Chengkui Tang for always loving me and supporting me in my ups and downs. They have raised me up and brought me to where I am now. I love them very much!

I think my acknowledgment list can just go on and on. It is truly a great experience as a PhD student at BU. Let me end my acknowledgment with a big thank-you to God, for His faithfulness and sufficient grace upon me.

# QUANTUM MONTE CARLO STUDIES OF QUANTUM CRITICALITY IN LOW-DIMENSIONAL SPIN SYSTEMS

(Order No.            )

**YING TANG**

Boston University Graduate School of Arts and Sciences, 2014

Major Professor: Anders W. Sandvik, Professor of Physics

## ABSTRACT

Strongly correlated low-dimensional quantum spin models provide a well-established framework to study magnetic properties of insulators, and are of great theoretical interest and experimental relevance in condensed-matter physics. In this thesis, I use quantum Monte Carlo methods to numerically study quantum critical behavior in low-dimensional quantum spin models and wavefunctions.

First, I study spinons—emergent spin-1/2 bosonic excitations—at certain one- and two-dimensional quantum phase transitions (QPTs) in spin models, by characterizing their size and confinement length quantitatively. In particular, I focus on the QPT from an antiferromagnetic (AFM) phase into a valence-bond solid (VBS) phase, which is an example of a violation of the standard Landau-Ginzburg-Wilson paradigm for phase transitions. This transition in two dimensions (2D) is instead likely described by a novel theory called “deconfined quantum criticality” (DQC). According to the theory, spinons should be deconfined. The degree of deconfinement is quantified in my calculations.

Second, I present a comprehensive study of so-called short-bond resonating-valence-bond (RVB) spin liquids in 2D, which have been suggested as a good starting point for understanding the spin physics of high-temperature cuprates. I find that these RVB states can also be classified as quantum-critical VBS states, which indicates that RVB is less disordered than expected. This work suggests a possible mapping from the quantum RVB

states to classical dimer models via a classical continuum field theory—the height model. This map explicitly bridges well-established classical results to future quantum studies.

Third, I consider 1D amplitude product (AP) states, which are generalized versions of RVB states, with different wavefunction weightings of bonds according to their lengths. AP states constitute a good ansatz for certain Hamiltonians and are of broad interest in quantum magnetism. I study phase transitions from AFM–VBS phases in AP states by tuning their amplitudes, and obtain continuously varying critical exponents. In addition, I classify the 1D AP states through entanglement entropy calculations of the central charge in (1+1)D conformal field theory. This new classification could serve as guide for AP states as trial wavefunctions to search for ground states of corresponding quantum spin models.

# Contents

<b>1</b>	<b>Introduction</b>	<b>1</b>
1.1	Classical and quantum phase transitions . . . . .	2
1.2	Deconfined quantum criticality . . . . .	6
1.3	Emergent spinons . . . . .	8
1.4	Spin liquids . . . . .	10
1.5	Entanglement entropy . . . . .	13
1.6	Thesis outline . . . . .	15
<b>2</b>	<b>Quantum Monte Carlo Methods and Measurements</b>	<b>17</b>
2.1	Sampling of valence bond states . . . . .	18
2.1.1	Valence bond basis . . . . .	19
2.1.2	Transition graphs . . . . .	20
2.1.3	Correlation functions . . . . .	22
2.1.4	Monte Carlo sampling of valence bond states . . . . .	23
2.2	Projector Monte Carlo with valence bond states . . . . .	29
2.2.1	Basic ideas of Projector Monte Carlo . . . . .	29
2.2.2	Steps in PMC method . . . . .	32
2.2.3	Measurement of observables . . . . .	36
2.2.4	Generalization to $J - Q_3$ model . . . . .	37
2.2.5	Application to spinon characterization . . . . .	39
2.3	Renyi entanglement entropy measurement . . . . .	40

<b>3</b>	<b>Characterizing Spinons as Emergent Elementary Particles</b>	<b>42</b>
3.1	Introduction . . . . .	42
3.2	Methods and calculated observables . . . . .	45
3.2.1	Generalized VB basis for $S > 0$ . . . . .	45
3.2.2	Characterization of spinons in the VB basis . . . . .	47
3.3	Deconfined spinons in uniform spin chains . . . . .	49
3.3.1	Results for the $J-Q_3$ chain . . . . .	50
3.3.2	Break-down of spinons as quasi-particles of a Néel state in one dimension	58
3.4	Spinon confinement arising from modulated couplings . . . . .	61
3.5	Heisenberg ladders . . . . .	65
3.6	Detecting spinons in spin correlations . . . . .	67
3.7	Summary and discussion for 1D chains . . . . .	71
3.8	RVB Spin Liquid . . . . .	72
3.9	2D $J-Q$ model . . . . .	74
3.10	Revisit 1D deconfinement . . . . .	76
3.11	Conclusion and discussion for the deconfinement of spinons in 2D . . . . .	77
<b>4</b>	<b>Properties of Resonating Valence Bond Spin Liquids and Critical Dimer Model</b>	<b>79</b>
4.1	Introduction . . . . .	79
4.1.1	Correlations in RVB and dimer states . . . . .	81
4.1.2	Height representation and topological sectors . . . . .	83
4.1.3	Outline of the chapter . . . . .	85
4.2	Results . . . . .	86
4.2.1	Sector probabilities . . . . .	86
4.2.2	Probabilities results . . . . .	87
4.2.3	Spin correlations in the RVB state . . . . .	88

4.2.4	Dimer correlations . . . . .	90
4.2.5	Correlations with nonzero winding number . . . . .	96
4.2.6	Monomer distribution . . . . .	101
4.2.7	Including longer bonds . . . . .	103
4.3	Height model interpretation . . . . .	105
4.3.1	Four ways to extract stiffness . . . . .	105
4.3.2	Summary of the stiffness estimates . . . . .	110
4.4	Order-parameter distribution . . . . .	111
4.5	Summary and discussion . . . . .	114
<b>5</b>	<b>Amplitude Product States in 1D Chains</b>	<b>118</b>
5.1	Introduction . . . . .	118
5.1.1	Amplitude-product states . . . . .	119
5.1.2	Spin and dimer correlations . . . . .	120
5.1.3	Outline of the chapter . . . . .	122
5.2	Phase Diagram in 1D . . . . .	122
5.3	Rényi Entanglement Entropy Calculations . . . . .	129
5.3.1	Fitting method . . . . .	129
5.3.2	Results . . . . .	132
5.4	Summary and future work . . . . .	135
<b>6</b>	<b>Conclusion</b>	<b>137</b>
6.1	Summary of highlights . . . . .	137
6.2	Future prospects . . . . .	138
	<b>Appendices</b>	<b>140</b>
<b>A</b>	<b>Four-spin correlators in the valence-bond basis</b>	<b>141</b>

<b>B</b>	<b>Calculations based on height representation</b>	<b>146</b>
B.1	Relation of height field and dimer operators . . . . .	147
B.2	Effects of long dimers . . . . .	148
B.3	Dimer correlations: dipolar term . . . . .	148
B.4	Dimer correlations: Critical term . . . . .	149
B.5	Topological (monomer) defects and their correlations . . . . .	150
B.6	Sector probabilities . . . . .	151
B.7	Correlation modulation due to winding number . . . . .	152
B.8	Anisotropic effects due to winding number . . . . .	152
	<b>Bibliography</b>	<b>158</b>
	<b>Curriculum Vitae</b>	<b>174</b>

# List of Tables

4.1	Dimer-dimer and monomer exponents obtained for the CDM and RVB systems at different fugacities $Z_2$ for the next-shortest bonds (of length $\sqrt{5}$ ). . .	104
4.2	Stiffness parameter $K_P$ in the infinite CDM and RVB systems inferred from the winding-number sector probabilities (from data in Fig. 4.3) according to Eq. (4.7). . . . .	106
4.3	Stiffness estimates obtained from the four kinds of measurements discussed in the text; $Z_2$ is the fugacity for dimers of length $\sqrt{5}$ . . . . .	108

# List of Figures

1.1	Schematic phase diagrams of (a) water molecules $H_2O$ , and (b) the Ising model in a magnetic field. Both diagrams have first-order phase transitions between (a) liquid and gas, and (b) between two ferromagnetic phases. Solid green lines are coexistence curves of first-order transition points. Continuous phase transitions take place at the critical point, shown here as the dark solid circles. . . . .	3
1.2	(a) The density of water molecules $\rho$ changes continuously when $T \geq T_c$ and $P \geq P_c$ , and changes discontinuously below $T_c$ and $P_c$ . Similarly, (b) the magnetic order parameter (magnetization $M$ ) changes continuously above $T_c$ and discontinuously below $T_c$ . The discontinuous change corresponds to first-order transitions, which end at the critical point. At $T_c$ the behavior is still singular, while for $T > T_c$ , the phase transition is replaced by smooth changes. . . . .	4
1.3	A schematic phase diagram for Quantum Phase Transition (QPT). A QPT is driven by quantum fluctuations tuned by some parameter $g$ at zero temperature. The parameter could be pressure, magnetic field, chemical substitution etc. The curved lines together with the critical point $g_c$ form the quantum critical “fan” region below certain temperature, where quantum fluctuations still affect finite temperature properties of the system. . . . .	5

1.4	An illustration of a dimerized 2D spin model with two different coupling strengths between nearest spin pairs. When $J_1/J_2$ is big, system is a quantum paramagnet; when $J_1/J_2$ is small, system has AFM order. . . . .	7
1.5	A schematic picture of an antiferromagnetic (AFM) configuration. Spin rotational symmetry is broken in this state and the long-range magnetic order is demonstrated in the alternating up and down spins. . . . .	8
1.6	A schematic picture of a valence bond solid (VBS) configuration. The (blue) ellipses represent entangled pairs — singlets. These singlets form the crystal-like structure, therefore this state is referred as “solid”. . . . .	8
1.7	A schematic picture to describe four degenerate states (a)-(d) in a VBS. . .	9
1.8	A schematic picture of emergent spinons in valence bond solid states (a-b) and the disordered state (c). A pair of spinons could emerge by breaking one singlet and form the triplet pair as shown in red arrows in (a). This pair of spinons could separate in the system and cause a path of misaligned valence bonds in the ordered state (b). Spinons become deconfined and move like free quasi-particles in the disordered state (c). . . . .	10
1.9	A possible configuration of resonating valence bond (RVB) spin liquids. Generally speaking, spin liquids are superpositions of all possible valence bond configurations. . . . .	12
1.10	A schematic figure showing a system divided into two subsystems $A$ and $B$ .	13
1.11	An illustrative sketch to explain variables in the scaling function of the Renyi entanglement entropy in Eq.(1.9) on a 2D square lattice. The periodic boundary condition is applied in both directions. . . . .	15

2.1 Two valence-bond states (left and right) in two dimensions and their transition graph formed by superimposing the two bond configurations (center). One of the spin configurations compatible with the transition graph is also shown, with open and solid circles for  $\uparrow$  and  $\downarrow$  spins. Each loop has two such allowed staggered spin configuration, and the overlap of two valence-bond states is thus  $\langle V_\beta | V_\alpha \rangle = 2^{n_{\alpha\beta} - N/2}$ , here with the number of loops  $n_{\alpha\beta} = 4$  and the number of spins  $N = 16$ . . . . . 20

2.2	<p>Monte Carlo updates for the RVB state in the combined spin-bond basis. Open and solid circles represent <math>\uparrow</math> and <math>\downarrow</math> spins. In the basic moves (a) and (b), only one of the two two valence bond configurations is affected at a time.</p> <p>(a) A simple two-bond update. Choosing two sites on the same sublattice, the two bonds connected to them can be reconfigured in a unique way. If the spins are compatible with the <math>\uparrow, \downarrow</math> singlet restriction, this update can be accepted.</p> <p>(b) Loop-cluster update. Choosing an arbitrary starting site (in this example in the left-upper corner) two defects (a site with no dimer or two dimers connected to it, both indicated with an <math>\times</math>) are generated by moving the end of the dimer on the initial site to another site which satisfies the bond-length constraint (here, in the extreme short-bond RVB, the length is always one) and the spin-singlet compatibility (anti-parallel spins on the bond). The dimer that was previously connected to this site is then moved away from the double-bond defect to another site. This process continues until a bond returns back to “annihilate” the original empty-site defect, which here happens already after two bond moves [the last step in (b)]. In both (a) and (b), we only show the bonds of the configuration involved in this update.</p> <p>(c) Monomer update. Monomers are shown as larger circles and must appear in the same locations in the state <math> V_\alpha\rangle</math> and <math> V_\beta\rangle</math>, the bonds of both of which are shown here (as solid and dashed lines). In addition to the two-bond or loop update of the bonds, monomers can move to a site on the same sublattice by also moving a bond which is common to the two valence bond states. . . . .</p>	26
2.3	<p>An illustration of how the singlet projector (the red rectangle) works. In the top panel I, singlet projector <math>C_{ab}</math> acts on the singlet <math>(a, b)</math> and leave the configuration unchanged. In the bottom panel II, singlet projector acts on sites <math>c</math> and <math>b</math>, and projects out the singlet <math>(c, b)</math> with the rearrangement of new bond <math>(a, d)</math>. The weight of this reconfiguration is <math>1/2</math>. . . . .</p>	30

- 2.4 An illustration of some key steps in projector Monte Carlo algorithm with the loop update. The open and solid circles represent down and up spins. The open and solid rectangles represent diagonal and off-diagonal operators. Operator strings  $S_l^e$  and  $S_r^f$  operate on states from the left and right ends for  $m$  times, to project the ground state out at around the midpoint of the path. For the demonstration purpose, here we only have  $m = 2$ . (a) We initialize valence bond states and spin configurations at boundaries. We insert diagonal operators on antiparallel spins. We then connect operator vortices to each other and also to the valence-bond states at boundaries to construct loops. (b) We choose loops to flip by probability  $1/2$ . We label flipped loops in red dashed lines and un-flipped loops in black solid lines. The spins at boundaries are updated with corresponding loops. The operators located between two different types of loops switch their types as well — from diagonal to off-diagonal and vice versa. (c) The last step is to treat diagonal and off-diagonal operators as singlet projectors, in order to propagate bonds from two ends to the middle and carry out the observable measurements. We also update spins in the intermediate states according to operator types. We could also update diagonal operators to new legal positions as well, which is not shown in this figure. This is called one MC sweep. . . . . 33
- 2.5 The measurement of  $C(\mathbf{r})$  at  $r = (L/4, L/4)$  versus the number of propagation steps for 2D Heisenberg model on a square lattice with edge length  $L = 32$ .  $m$  is the number of propagation steps and  $N$  is the system size. The ratio  $m/N$  is plotted in a logarithmic scale.  $C(L/4, L/4)$  is not converged until  $m/N$  reaches 16. . . . . 36

- 2.6 An illustration of loop updates in PMC for the  $J - Q_3$  model on a 8-size spin chain. Similarly as the Heisenberg model in Fig.2.4, we connect all operator vortices together with valence-bond states on boundaries to form closed loops. Since the  $Q_3$  term has 3 singlet operator vortices, it has 12 legs. Each operator could be updated independently from the other two, in order to sample 8 combinations of diagonal (open rectangle) and off-diagonal (solid rectangle) operators. We use *bits* to record the operator information, as listed in the bottom of the figure. The first three bits correspond to the type of operators, 0 for diagonal and 1 for off-diagonal. The last bit distinguishes the operator group, 0 for  $J$  term and 1 for  $Q$  term. . . . . 38
- 2.7 An illustration of PMC simulations for triplet states. We sample valence-bond states with two  $S = 1/2$  spinons (bigger blue solid circles) in the system. In the PMC simulation, we treat the triplet (blue dashed line) as singlet. The only difference from the ground state ( $S = 0$ ) simulation is that we never flip the loop containing spinons. . . . . 39
- 2.8 We use a 6-site spin chain to illustrate the swap operator and improved ratio trick. In (a), we have two copies of the system (upper and lower), with different VB state configurations. The red (lower) VB states are for reference and swap operator acts on black (upper) VB states. In (b), as we divide the system into two regions, A and B, the swap operator exchanges all VB state connections in region A between two copies. (c) illustrates that with first region swapped, the ratio measurement only operates on the region difference  $A_{i+1} - A_i$ . As we discussed in the text, this ratio trick will improve the statistical performance significantly. . . . . 41

3.1	Transition graph formed by bra (upper, black) and ket (lower, green) valence bond states on a spin chain. Part (a) shows an $S = 0$ state on an even number of sites. In (b) the number of sites is odd and there is an unpaired spin in both the bra and the ket state. Part (c) shows an $S = 1$ configuration, where there are two unpaired spins. In VBPQMC simulations, the distance distribution of the unpaired spins in (b) gives information on the size of an individual spinon, while the size of an $S = 1$ bound state of two spinons is reflected in the distance distribution of unpaired spins on different sublattices in (c). . . . .	46
3.2	Single spinon overlap distribution in the $J - Q_3$ chain. (a) Exponential decays indicating well-defined quasi-particles in VBS states at different values of $g = Q_3/J$ . The size $\lambda$ of the spinon (the inverse of the slopes of the lines on the lin-log plot) diverges as the critical point is approached. Panel (b) shows that spinon is marginally defined at the critical point, with the overlap decaying as a power-law with exponent $\alpha = 0.500(2)$ . The even-odd oscillations are due to the frustration caused by the single-spinon defect in a periodic chain (with the odd- $r$ contributions only possible in a bipartite system). The effects of frustration diminish as the chain size increases. . . .	51
3.3	(a) Single-spinon distribution function at the VBS transition point and inside the critical phase. (b) The data at $g_c$ rescaled such that data collapse is achieved. The lines correspond to the $r^{-1/2}$ form. . . . .	52
3.4	Two-spinon distance distribution in VBS states of the $J-Q_3$ chain at (a) fixed $g = 4$ and different chain lengths, (b) fixed chain length $N = 256$ and different coupling ratios. The $x$ - and $y$ -axis has been rescaled with $N$ and $1/N$ , respectively, in order to achieve data collapse in (a). The distributions in (b) show that the effective spinon-spinon repulsion becomes weaker as system approaches the the transition point ( $g_c = 0.1645$ ). . . . .	54

3.5	Distribution of spinon separations in $S = 1$ states at and below the VBS transition point $g_c$ . The lines going through the $g_c$ points have slope 0.7. . .	56
3.6	The same-sublattice distribution function for $S = 1$ states at three different values of the coupling ratio. The corresponding distributions $P_{AA}(r)$ for the $S = 1/2$ states at the same couplings are shown in lighter (brown) color and they coincide very closely with the $S = 1$ functions (thus, demonstrating that the single-spinon size can be obtained also from the $S = 1$ simulations). The system size here is $N = 1024$ for $S = 1$ and 1025 for $S = 1/2$ . . . . .	57
3.7	Same-sublattice distribution functions for $S = 1$ states in the critical phase. (a) shows results for different coupling ratios for fixed system size $N = 512$ , while in (b) results at $g_c$ are re-scaled to achieve data collapse for several system sizes. The lines have slope $1/2$ and $1$ for small and large $r$ , respectively.	59
3.8	Size-scaled spinon overlap function in a Néel-ordered chain with total $S = 1/2$ . The asymptotically flat (with even and odd- $r$ branches) distribution shows that the spinon is not a well-defined quasi-particle in the Néel state, as expected. . . . .	60
3.9	Spinon distribution functions in the $J_1$ - $J_2$ - $Q_3$ chain with $Q_3 = 4$ and several values of the modulation parameter $\rho = J_2/J_1$ . (a) shows exponential decays, $P_{AA}(r) \sim e^{-r/\lambda}$ , of the single-spinon distribution function of the $S = 1/2$ state, demonstrating well-defined spinons with finite intrinsic size $\lambda$ . The data points plotted with light brown symbols are the corresponding results for the same-sublattice distribution $P_{AA}^*$ computed in the $S = 1$ state. In (b), spinon confinement for $\rho \neq 1$ is demonstrated in the spinon-distance distribution function; $P_{AB}(r) \sim e^{-r/\Lambda}$ . The size of the bound state (the confinement length-scale) decreases as the coupling modulation is increased. Data for $\rho = 1$ are graphed for comparison—in this case the spinons are deconfined and the distribution function does not decay with the separation.	62

3.10	The same quantities as in Fig. 3.9 but with the ratio $Q_3/J_1 = g_c = 0.1645$ . Here the tuning of the modulation parameter $\rho$ toward 1 corresponds to approaching a critical point. . . . .	63
3.11	Spin correlation function in 2-Leg Heisenberg ladder systems. Here the intra-chain coupling $J_1 = 1$ and results are shown for several values of inter-chain couplings $J_2$ . $C(x, 0)$ decays exponentially when $J_\perp \neq 0$ and exhibits the power-law decay of the isolated chain when $J_\perp = 0$ . In the inset, the correlations are large distances on a log-log scale at $J_2 = 0$ and $J = 0.1$ . Because here the system length $L$ is smaller than the correlation length it is not yet possible to observe the exponential decay. . . . .	66
3.12	Spinon distribution functions in $S = 1$ states of Heisenberg ladders with different run couplings $J_2$ . Both distribution functions are exponentially decaying for $J_2 = 0.5, 1$ , and $2$ , while for $J = 0.1$ the system size is not sufficiently large for observing the expected asymptotic exponential decay. The forms for the critical system at $J_2 = 0$ were discussed in Sec.3.3. . . . .	68
3.13	Absolute value of the spin correlation function in the $S = 1/2$ and $S = 1$ state, after subtraction of the $S = 0$ correlation function according to Eq. (3.14). (a) is for a $J$ - $Q_3$ chain with $Q_3/J = 4$ and (b) is for a $J_1$ - $J_2$ - $Q_3$ chain with $J_2/J_1 = 1.1$ and $Q_3/J_1 = 4$ . In both cases the chain length is $N = 512$ . The sharp dips where the error bars are large for the $S = 1$ quantities correspond to phase shifts. In (b) the even- $r$ and odd- $r$ branches are graphed in different colors to show the even-odd effects, while in (a) these effects are small. All lines correspond to exponential fits. . . . .	70
3.14	Spin correlation difference for Heisenberg ladder systems in the $S = 1$ sector. The lines show exponential fits. . . . .	71

3.15	Spinon distributions and correlations along the diagonal lattice direction of the RVB spin liquid. Black circles show the single-spinon overlap $P_{AA}(r)$ in an $S = 1/2$ state on a $65 \times 65$ lattice. The exponential decay (fitted line) gives the spinon size $\lambda = 2.96(1)$ lattice spacings. Red squares show the two-spin distribution $P_{AB}(\mathbf{r})$ in the $S = 1$ state on a $64 \times 64$ lattice, fitted to $\sim 1/r^\alpha$ with $\alpha \approx 0.6$ . The green triangles show the absolute value of the difference $\Delta_S(r)$ between the spin correlations in the $S = 1$ and $S = 0$ systems. This quantity exhibits both a spinon-size effect (exponential short-distance decay) and deconfinement (weak power-law decay at long distances). There is a phase shift at $r \approx 9\sqrt{2}$ . . . . .	73
3.16	Spinon distributions for the 2D $J$ - $Q_3$ model on $L = 128$ and $129$ lattices at $g = 3$ (VBS) and $g_c = 1.5$ (critical). The lines are exponential fits for the $g = 3$ VBS, giving the single-spinon size $\lambda = 6.4$ extracted from $P_{AA}(r)$ in the $S = 1/2$ state and the confinement length $\Lambda = 3.1$ extracted from $P_{AB}(r)$ in the $S = 1$ state. Both lengths diverge as $g \rightarrow g_c$ , where the distributions decay algebraically. . . . .	74
3.17	The confinement length $\Lambda$ , the correlation length $\xi$ , and the spinons size $\lambda$ in the VBS phase and approaching the critical point ( $g_c = 1.50$ ) of the $J$ - $Q_3$ model. The calculations were done with $L = 128$ and $129$ . The power-law fits (solid curves) are discussed in the text. . . . .	75
3.18	Spinon distributions in the $J_1$ - $J_2$ - $Q_3$ chain with $Q_3/J_1 = 0.1645$ (the critical point when $J_1 = J_2$ ) for three ratios $\rho = J_2/J_1$ . The straight lines for $\rho > 1$ are exponential fits and the curves for $\rho = 1$ are power-law fits. . . . .	77

4.1	Configurations in different winding number sectors, $W = (W_x, W_y)$ . Here $W_y$ is given by the number of bonds crossing the line drawn in the $y$ -direction (since those bonds are at even $y$ —shifting the bond configuration by one step in the $y$ -direction leads to $W_y \rightarrow -W_y$ ). The last case is the unique configuration in its winding number sector and constitutes the staggered state of the QDM. . . . .	84
4.2	(a) Reference state used here for defining the winding number. The direction of the dimers is from sublattice B (open circle) to sublattice A (solid circle). (b) An arbitrary valence bond state, with dimers drawn in the opposite direction, from sublattice A to sublattice B. (c) The transition graph formed by the reference states in (a) and the arbitrary state in (b). The winding numbers correspond to the net fluxes (in units of the system length $L$ ) defined by traversing the loops formed along the arrows; here $\Phi_x = 1$ and $\Phi_y = 0$ , or $\Phi = (1, 0)$ , which corresponds to winding number $W = (0, 1)$ in the definition of Fig. 4.1 . . . . .	85
4.3	Winding number probabilities obtained in simulations with the loop algorithms for the RVB and CDM (with only the shortest bonds, as in Fig. 2.2). Results for several low- $W$ sectors of the CDM (lower panel) and RVB (upper panel) are shown versus the lattice size on a lin-log scale. In the RVB, the probability of the off-diagonal sector $W = (0, 1; 0, 0)$ vanishes exponentially with $L$ , reflecting the orthogonality (when $L \rightarrow \infty$ ) of states in different winding number sectors. . . . .	88
4.4	Spin correlations versus lattice distance $r$ in the short-bond RVB in the sector of winding numbers $W = (0, 0)$ (top panel) and $W = (0, 3L/7)$ (bottom panel) computed using $L \times L$ lattices with $L = 48$ . Results are shown for the separation $(x, y)$ taken along the two axis, $(r, 0)$ , $(0, r)$ , as well as on the diagonal, $(r/\sqrt{2}, r/\sqrt{2})$ . . . . .	89

4.5	Dimer-dimer correlation function difference (4.4) at the maximal distance versus the lattice size. The upper panel shows results for the quantum RVB in different topological sectors as well as in the grand canonical ensemble (including all winding number sectors, in which case the fluctuations between sectors becomes very slow for large systems, as reflected in the large error bar for $L = 48$ ). All correlations converge to the same power-law decay as system size increases. The power, based on the $W = (0, 0)$ data for large $L$ , is $\alpha = 1.191(6)$ . The lower panel shows results for the CDM, which are consistent with $\sim 1/r^2$ (shown with the solid line) for all winding number sectors. . . . .	91
4.6	Fourier transform $\mathbf{S}(\mathbf{q})$ of the dimer-dimer correlation function $D_{xx}(\mathbf{r})$ for systems of size $L = 32$ . The squares represent the full reciprocal space $q_x, q_y \in [0, 2\pi]$ . Results in winding number sectors $W = (0, 0)$ , $W = (0, 1)$ , and $W = (0, 8)$ are shown for the RVB (left) and CDM (right). The location of the broad (“incommensurate”) peak in both cases is $\mathbf{Q} = (\pi, 2\pi W_y/L)$ . The sharp peak at $(\pi, \pi)$ is due to a nonzero average staggered dimer order induced by a nonzero winding number. This peak has been removed in the graphs $W = (0, 8)$ in order to make the other features of the correlations better visible. The height of the peaks as a function of the system size is analyzed in Fig. 4.7. . . . .	93

4.7	Peak values of the dimer structure factor, where $\mathbf{Q} = (\pi, 2\pi W_y/L)$ , versus the system size in sectors with different winding $W_y$ . The modified definition $S'(\mathbf{Q})$ for the RVB is given in Eq.(4.5). Note the different $y$ -axis scales used for the two models (logarithmic for the RVB and linear for the CDM). In the CDM (lower panel) the behavior is consistent with a log divergence (as shown with fitted lines) for small winding numbers, but for larger $W$ it appears that the behavior is instead governed by a power law (which then may be the case for all $W_x/L > 0$ for sufficiently large systems). The curve through the $W = (0, 3L/7)$ data shows $S(\mathbf{Q}) \propto L^{0.48}$ . In the RVB (upper panel) the exponent of the power-law divergence decreases slightly with increasing winding number. The legends with $(S)$ correspond to the peak values of the full structure factor $S(\mathbf{Q})$ . . . . .	94
4.8	Dimer correlation differences versus $x$ [where the separation $\mathbf{r} = (x, x)$ ] along the diagonal lattice direction for systems of different size. The winding number is $W = (0, 2)$ , and therefore two phase shifts are seen (corresponding to a total of four domains). Note that the overall magnitude of these correlations is much larger in the RVB (upper panel) than in the CDM (lower panel). . . . .	97

4.9	Correlation patterns obtained from the dimer correlator $D_{xx}(x, y)$ by subtracting a constant and dividing the result by the leading power-law form $r^{-\alpha}$ (with $\alpha = 1.2$ for the RVB and $\alpha = 2$ for the CDM). The $(\pi, \pi)$ contribution was also removed for the $W \neq 0$ sectors (by going to Fourier space as in Fig. 4.6). Black and red (gray) bars represent positive and negative values (i.e., stronger and weaker dimer correlations), respectively. In the $W = (0, 0)$ sector, a dominant columnar pattern is visible, while in the $W = (0, 1)$ sector the correlations shift from weak-strong weak-strong to strong-weak strong-weak over a window of distances $\propto L$ , corresponding to two nodal lines as stated in text. The origin is at lower left corner, and one quadrant ( $L/2 \times L/2$ ) is shown of the possible separations. In the $W = (1, 1)$ sector, correlations shift twice in a row, corresponding to the presence of two pairs of nodal lines.	98
4.10	Monomer distribution function in the RVB state on an $L = 512$ lattice. The straight line is a fit to the power-law form $1/r^\beta$ with $\beta = 0.830(9)$ .	101
4.11	Dimer-dimer correlation function difference $D_{xx}(r)$ for RVB systems in the $W = (0, 0)$ sector with different fugacities $Z_2$ of long (fourth-neighbor) bonds (with the short-bond fugacity $Z_1 = 1$ ). The decay exponents grows with the long-bond fugacity. The values are given in Table 4.1.	102
4.12	Monomer distribution function $M(r)$ for RVB states with a small fraction of fourth-neighbor bonds on a lattice of size $L = 256$ . The straight lines are fits giving deconfinement exponents which decrease with increasing long-bond fugacity. The exponents are listed in Table 4.1.	103
4.13	$K_P$ value calculated in the $W = (0, 1)$ sector according to Eq. (4.7) for systems with fugacity $Z_2 = e^{-2}$ for long bonds and different lattice sizes. RVB and CDM results are shown in the upper and lower panel, respectively, as a function of the inverse system size $1/L$ . The curves are second-order polynomial fits, not including the linear term.	107

4.14	VBS order parameter distribution function $P(D_x, D_y)$ in the space of point pairs $(D_x, D_y)$ generated in the Monte Carlo simulations of the RVB state (left) and CDM (right) for systems of size $L = 64$ . We are only concerned here with the shapes of these distributions (a ring with depleted weight in the center for the RVB and a broad central peak for the CDM) and have therefore not labeled the graphs with the range of $(D_x, D_y)$ or the actual values of the probability density. . . . .	112
4.15	VBS order parameter distribution function $P(D_x, D_y)$ for $L = 48$ systems in the grand-canonical winding number ensemble (left) and with winding number $W = (0, 1)$ (right). Here the range of $D_x, D_y$ values is the same in both cases, i.e., the distribution for $W = (0, 1)$ is much narrower. . . . .	113
5.1	The upper panel shows the crossing behavior of the Binder cumulant $U(\kappa)$ defined in Eq. (5.4) for several different chain lengths $L$ when $\lambda = 1$ . The approach to 1 for small $\kappa$ and 0 for large $\kappa$ corresponds to the presence and absence of Néel order, respectively. The crossing point approaches the critical value of $\kappa$ . The lower panel demonstrates extrapolations to the thermodynamic limit of the critical $\kappa_c$ by fitting crossing points of $(L, 2L)$ pairs to the power-law correction (5.12). . . . .	123
5.2	Phase diagram of 1D AP states with tuning parameters $\kappa$ and $\lambda$ , as defined in Eq. (5.11). The circles are calculated transition points and the curve is a guide to the eye representing approximately the boundary between the long-range ordered Néel (below) and VBS (above) phases. The inset exemplifies long-distance spin correlation functions inside the phases and at the critical point when $\lambda = 1$ ; the black squares correspond to $\kappa = 1.6$ (inside VBS phase) and the green triangles are for $\kappa = 1.4$ (in the Néel phase). The red circles show the behavior at the critical point. . . . .	125

5.3	Staggered spin-spin (upper panel) and dimer-dimer (lower panel) correlations of 1D AP states at the largest distance, graphed versus the chain length at $\kappa = \kappa_c$ for different short-bond amplitudes $\lambda$ . All lines are fits to the form $aL^{-b}$ . . . . .	126
5.4	The continuously varying spin ( $\alpha$ ) and dimer ( $\beta$ ) decay exponents of the 1D AP state (5.11) as a function of the short-bond amplitude $\lambda$ . The exponents correspond to the power-law decay of the correlation functions; $C(r) \sim r^{-\alpha}$ , $D^*(r) \sim r^{-\beta}$ . The points are calculated values and the curves are guides to the eye. . . . .	128
5.5	Second Rényi entanglement entropy calculated by using the DMRG method for the 1D Heisenberg chain. The solid line is the fit by the scaling function in Eq. (5.15). . . . .	131
5.6	Second Rényi entanglement entropy calculated by QMC for AP states. The solid lines are fits done by the scaling function in Eq. (5.16). The oscillation increases with increasing $\lambda_c$ . . . . .	132
5.7	Second Rényi entropy versus the chord length $[L_x/\pi \sin(\pi l/L_x)]$ when $l$ is an even number. Solid lines are fitting lines in the form of Eq.(5.14). In the top panel, all fits are done together with the same central charge $c = 1.04(1)$ and different $d_2$ on different sizes at $\lambda = 1$ . In the lower panel, the fitting function works well for all $\lambda$ , with different $c$ and $d_2$ values. All $c$ values are plotted in Fig. 5.8. . . . .	133
5.8	Central charge values versus the short-bond amplitude $\lambda$ . The $c$ values calculated from single-branch fittings are represented by red circles, and $c$ values calculated from double-branch fittings are shown in green squares. Both values agree with each other within error bars. We find $c = 1$ for $\lambda > 0.2$ , and $c > 1$ for $\lambda \leq 0.2$ . When $\lambda$ is near zero, $c \approx 3/2$ . . . . .	134

A.1	Action of a singlet projection operator in two different cases; (a) when the sites $b, c$ are on different sublattices and (b) when $b, d$ belong to the same sublattice. The arrows indicate the order of the spins in a singlet; $(a, b) = ( \uparrow_a \downarrow_b\rangle -  \downarrow_a \uparrow_b\rangle)/\sqrt{2}$ , and, in the case of spins on different sublattices, conforms with the definition (2.1) of bipartite valence bond states. . . . .	142
A.2	Illustration of the equivalence (A.5), due to overcompleteness, between a state formed by two non-bipartite valence bonds and a superposition of two states involving only bipartite bonds. . . . .	142
A.3	Operations for evaluating the four-spin matrix element $\langle V_\beta   (\mathbf{S}_k \cdot \mathbf{S}_l) (\mathbf{S}_i \cdot \mathbf{S}_j)   V_\alpha \rangle$ when all the sites $i, j, k, l$ are in the same loop of the transition graph. The thin lines connecting labeled sites refer to the operator components $S_k^z S_l^z$ and $C_{ij}$ in (A.8). The solid and dashed bonds belong to $ V_\alpha\rangle$ and $\langle V_\beta $ , respectively. . . . .	144
A.4	Subloops of a valence-bond loop with respect to two sites $i, j$ . The “cuts” splitting the loop into subloops are at the solid bonds connected to $i$ and $j$ (which belong to the ket $ V_\alpha\rangle$ ; the state on which $C_{ij}$ acts), irrespective of the two possible locations of $i, j$ within these bonds. When $i, j$ are sites in the same bond in $ V_\alpha\rangle$ , there is only a single subloop (the whole loop). . . .	145

# List of Abbreviations

AFM	Antiferromagnet
AP	Amplitude Product
CAP	Correlated Amplitude Product
CMD	Classical Dimer Model
DMRG	Density Matrix Renormalization Group
DQC	Deconfined Quantum Criticality
LGW	Landau-Ginzburg-Wilson
QDM	Quantum Dimer Model
QMC	Quantum Monte Carlo
QPT	Quantum Phase Transition
REE	Renyi Entanglement Entropy

RVB Resonating Valence Bond

VB Valence Bond

VBPQMC Valence Bond Projector Quantum Monte Carlo

VBS Valence Bond Solid

# Chapter 1

## Introduction

Since the first discovery in 1986 [1], high-temperature superconductivity (also called high- $T_c$  superconductivity, with the critical temperature  $T_c > 30K$ ) has been an intensely researched topic in physics, engineering and material sciences. However, still today, the mechanism of high- $T_c$  superconductivity has not yet been explained successfully, due to difficulties in treating strong correlations among electrons in theoretical models. One important aspect of explaining high- $T_c$  is to understand how the insulating antiferromagnetic (AFM) parent phase is destroyed and superconductivity sets in as the doping fraction increases. There are several interesting phase transitions and crossovers in this process, not only in the electronic properties, but also in the magnetic properties. For instance, Anderson has claimed that the physics of high- $T_c$  is related to an underlying spin liquid state, which has no AFM order and could be realized in the 2-dimensional (2D) Heisenberg model with frustrated interactions [2–4]. Inspired by the rich physics of high- $T_c$  cuprates and the important issue of the suppression of AFM order, in this thesis work I am interested in quantitatively studying quantum phase transitions involving the loss of AFM order in several different spin-1/2 models. The relationship to the high- $T_c$  problem is that an appropriate “deconfined” critical magnetic state may upon doping lead to a “strange metal” state (an unusual metallic state where standard metallic properties such as the temperature dependence of the resistivity break down), and eventually superconductivity. Characterizing various quantum-critical spin states and studying signatures of deconfinement at phase transitions, which I focus on

here, may therefore be keys to eventually solving the high  $T_c$  problem [5].

In this introduction chapter, I will first explain a few central concepts in condensed matter physics which are essential to my research presented in later chapters, and then present an overview of the thesis.

## 1.1 Classical and quantum phase transitions

Phase transitions take place in our universe very frequently. The high  $T_c$  example discussed above may sound distant from our daily life. The most familiar example of phase transitions may be boiling water, which we face almost everyday. As we increase the temperature, thermal fluctuations among water molecules increase as well. Once the temperature reaches the boiling temperature  $T = 373K$ , thermal fluctuations are strong enough to overcome the Van der Waals bonds between water molecules and thereby release molecules into gas form. The transition from liquid to gas is a classical *first-order* phase transition, because the first derivative of the Gibbs free energy in this process is discontinuous. In Fig. 1.1(a), we use solid lines to label coexistence curves, which consist of first-order transition points in the phase diagram. The liquid–gas coexistence curve ends at fixed  $T = T_c$  when there is no separation between liquid and gas. The temperature and pressure above which liquid water and gas become indistinguishable is called the critical temperature ( $T_c = 647K$ ) and the critical pressure ( $P_C = 22$  MPa) respectively. Exactly at the point  $(T_c, P_C)$  the phase transition is *continuous* because the first derivative of Gibbs free energy is continuous. A similar phase transition also exists in the Ising model, which is used among other things to describe some ferromagnets. The phase diagram of the Ising model is depicted in Fig. 1.1(b). In this case, there is a special line  $H = 0$ , where the system has a higher symmetry. Under the Currie temperature, the phase transition between two symmetry-broken ferromagnetic states is a first-order phase transition. At the Currie temperature  $T_c$ , this transition becomes *continuous*.

Phase transitions can be characterized by **order parameters**. An order parameter is a physical quantity that measures the degree of order in a state. In many phase transitions,

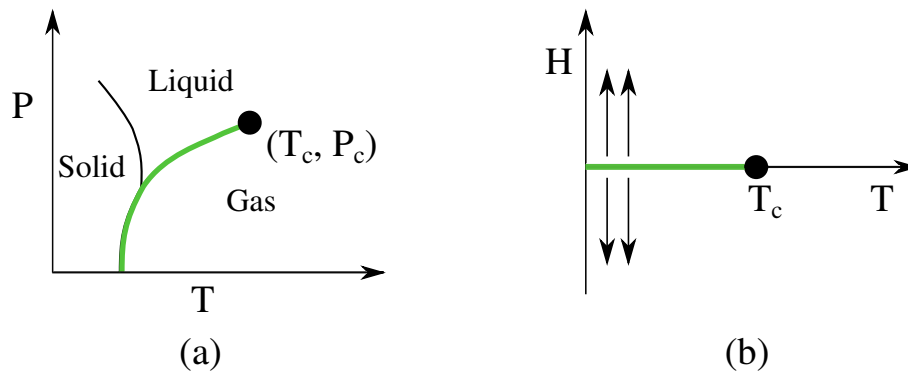


Figure 1.1: Schematic phase diagrams of (a) water molecules  $H_2O$ , and (b) the Ising model in a magnetic field. Both diagrams have first-order phase transitions between (a) liquid and gas, and (b) between two ferromagnetic phases. Solid green lines are coexistence curves of first-order transition points. Continuous phase transitions take place at the critical point, shown here as the dark solid circles.

such as the Ising Model at  $H = 0$ , a symmetry is broken when entering the ordered state, therefore the order parameter will change from zero to a nonzero value in this transition. In the case of the liquid–gas transition, there is no symmetry breaking but the density can be used as the order parameter to distinguish two phases. Order parameters can be calculated by taking the first derivative of the free energy with respect to some external fields, such as the magnetic field in the Ising model. As shown in Fig. 1.2, the sudden change of the density  $\rho$  under  $T_c$  and  $P_c$  indicates a first-order phase transition, and the continuous but singular change exactly at  $T_c$  and  $P_c$  implies a second-order phase transition. The magnetization  $M$  in Ising model corresponds to the density  $\rho$  in water. However, please note that, these two phase transitions are not exactly equivalent: at the critical point, there is no symmetry broken in the liquid–gas transition, while there is a spontaneous spin rotational symmetry broken in ferromagnets. Nevertheless, with the order parameter of the gas–liquid defined as the difference in density between the liquid and the gas, and that of the Ising model being the magnetization  $M$ , the symmetries of these order parameters are the same and, according to universality, the critical points are therefore associated with the same kinds of singularities (the same critical exponents).

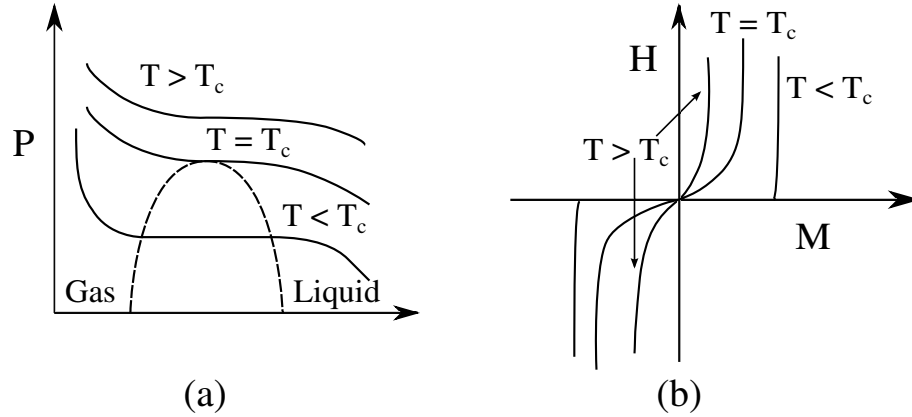


Figure 1.2: (a) The density of water molecules  $\rho$  changes continuously when  $T \geq T_c$  and  $P \geq P_c$ , and changes discontinuously below  $T_c$  and  $P_c$ . Similarly, (b) the magnetic order parameter (magnetization  $M$ ) changes continuously above  $T_c$  and discontinuously below  $T_c$ . The discontinuous change corresponds to first-order transitions, which end at the critical point. At  $T_c$  the behavior is still singular, while for  $T > T_c$ , the phase transition is replaced by smooth changes.

Similar to the classical phase transitions, there are *first order* and *second order* phase transitions in quantum systems as well. A **Quantum Phase Transition** (QPT) is a phase transition taking place between two distinct ground states (i.e., at temperature  $T = 0$ ) with tuning parameters like pressure, magnetic field, chemical substitution and so on at zero temperature [6–9]. A schematic phase diagram is shown in Fig.1.3, where  $g$  is the tuning parameter. Classical phase transitions are driven by thermal fluctuations. Analogously, the driving source of QPTs are provided by *quantum fluctuations*, which arise from competing (non-commuting) interactions in the Hamiltonian of the system. Strictly speaking, QPTs take place only at zero temperature, however, the quantum fluctuations still affect system properties at a certain range of finite temperatures, where the energy scale of the quantum fluctuations is similar to the thermal fluctuations. Quantum effects are still dominant when mode frequencies of the system are below the quantum-to-classical crossover frequency  $\frac{k_B T}{\hbar}$  [10].

The established theoretical framework for explaining both classical phase transitions and QPTs is Landau-Ginzburg-Wilson (LGW) paradigm. The central concept of LGW theory

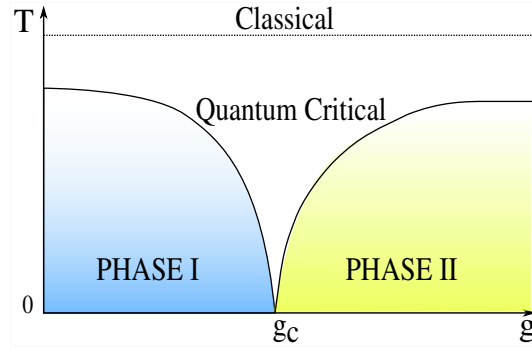


Figure 1.3: A schematic phase diagram for Quantum Phase Transition (QPT). A QPT is driven by quantum fluctuations tuned by some parameter  $g$  at zero temperature. The parameter could be pressure, magnetic field, chemical substitution etc. The curved lines together with the critical point  $g_c$  form the quantum critical “fan” region below certain temperature, where quantum fluctuations still affect finite temperature properties of the system.

is to use order parameter fields and their gradients to construct an effective free energy and obtain solutions using various approximations (such as mean-field theory) [11]. For studying the second order phase transitions, Renormalization Group methods (RG) [12] can be used to explain and study the singularities. LGW and RG methods have been successfully used to explain many QPTs.

In this thesis, we are particularly interested in continuous phase transitions, where the order parameter vanishes at some critical point  $g_c$  at  $T = 0$ . In addition to the vanishing order parameter, some physical properties, such as the characteristic length  $\xi$  (e.g. the correlation length), the susceptibility and the specific heat (in some cases) diverge at the critical point as  $|g - g_c|^{-p}$ , where  $p$  is the corresponding critical exponent. The critical exponents have *universal* values — values depending only on symmetries and the dimensionality of the system. We will consider quantum spin models in which the non-magnetic phase has an excitation gap. The characteristic energy, for example, the energy gap between the first excited state and the ground state (for the gapped system), vanishes as a power-law decay of the characteristic length with the dynamic exponent  $z$ , as  $\Delta \propto \xi^{-z}$ . The critical state abides at or near  $g_c$ , where the competition between two phases is the strongest. In

some quantum models, this critical state might be the long-sought-for *Spin Liquid* [13–16], which might be related to the superconducting states in high  $T_c$  superconductors and can also exist in certain classes of insulators with localized spin [5, 17, 18]. We will discuss spin liquid states more in Sec.1.4.

## 1.2 Deconfined quantum criticality

The well-established LGW theory associates singularities at the critical point with the low-energy long-range fluctuations of the order parameter fields. Behaviors of low-energy long-range fluctuations can be predicted by  $(d+1)$  classical models with the renormalization of parameters [19, 20]. For instance, 2D dimerized Heisenberg models, such as the columnar  $J_1 - J_2$  model depicted in Fig. 1.4, can be described by a quantum field theory called the  $(2+1)$  non-linear  $\sigma$ -model. By the argument of symmetries, the QPT in the field theory and in the dimerized  $J_1 - J_2$  model belongs to the universality class of the 3D classical Heisenberg model, where the transition versus temperature is continuous. This prediction also agrees with many numerical studies of the QPT between the AFM and a quantum paramagnet. In the columnar model in Fig. 1.4, this transition takes place at the critical ratio  $J_1/J_2 \approx 1.9$  [21]. The quantum paramagnet forms due to a high density of singlets at the  $J_1$  bonds, and this state therefore looks like a valence-bond-solid (VBS). However, the VBS order parameter has no singularity at the transition, only a cross-over from weak to strong. The loss of the AFM order into a quantum paramagnet characterizes this transition fully.

For the phase transition between the AFM state and a spontaneously formed VBS (i.e., which is not forced by interactions to form the singlets at certain bonds but can form in several ways, e.g., with horizontal or vertical valence-bonds) with the parent Hamiltonian conserving all spin and lattice symmetries, the story will be very different. LGW theory, with two different order parameter fields (two different spontaneous symmetry-broken states) in the model, predicts a first order QPT [12]. This prediction is in contrast to recent numerical studies, which have strongly supported a *continuous* phase transition in

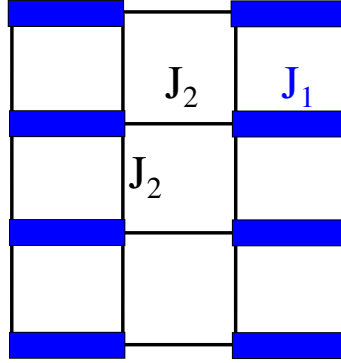


Figure 1.4: An illustration of a dimerized 2D spin model with two different coupling strengths between nearest spin pairs. When  $J_1/J_2$  is big, system is a quantum paramagnet; when  $J_1/J_2$  is small, system has AFM order.

this case [22–25]. In addition to the discrepancy in the AFM–VBS phase transition, the LGW paradigm also fails at explaining non-fermi liquid phenomena in the QPT between magnetic and nonmagnetic metallic phases in heavy fermion metals [26, 27].

With these puzzles in mind, **Deconfined Quantum Criticality** (DQC) was proposed by Senthil *et al* to explain the breakdown of the LGW paradigm in the vicinity of the critical point [28–30]. For the above examples, DQC has been successfully giving qualitative predictions in agreements with the numerical and experimental studies.

Instead of studying the critical theory using conventional order parameters, in the DQC theory it is argued that the key of describing the nature of these critical phenomena correctly is to capture the *emergent* degree of freedom, which are the fractional quantum particles and gauge fields. The fractionalized degrees of freedom emerge with a conservation law of the topological number under the protection of a  $U(1)$  gauge field. The term “deconfinement” is related to the non-compact  $U(1)$  field. The compact field theories allow the change of the topological numbers (in other words, the proliferation of the instanton events or topological fluctuation, which causes the confinement of emergent particles). Therefore, the non-compact  $U(1)$  field theory is a deconfined theory because the emergent fractional quantum number particles are deconfined. Details of the theory are beyond the scope of the thesis, but contacts will be made with predictions from it.

### 1.3 Emergent spinons

In this thesis, we are particularly interested in studying the phase transition between AFM states to VBS states formed due to spontaneously broken lattice symmetry. This phase transition is one of those claimed to violate the LGW paradigm and could be explained by the DQC theory in the critical region. The *fractional quantum number particle* in AFM-VBS phase transition is the emergent  $S = 1/2$  spinon.

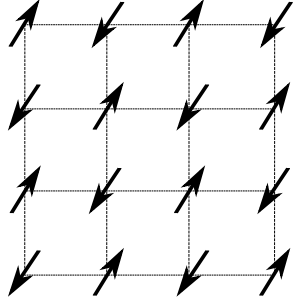


Figure 1.5: A schematic picture of an antiferromagnetic (AFM) configuration. Spin rotational symmetry is broken in this state and the long-range magnetic order is demonstrated in the alternating up and down spins.

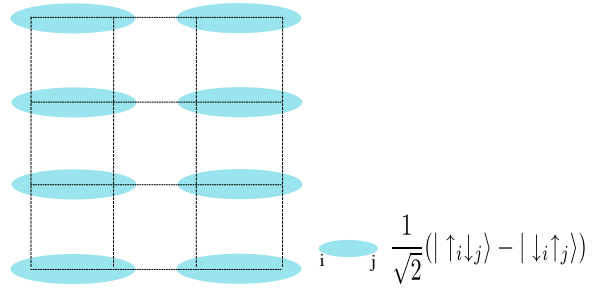


Figure 1.6: A schematic picture of a valence bond solid (VBS) configuration. The (blue) ellipses represent entangled pairs — singlets. These singlets form the crystal-like structure, therefore this state is referred as “solid”.

Antiferromagnetic (AFM, or Néel) states have long-range magnetic order, which is formed by antiparallel (staggered) neighboring spins. As depicted in Fig. 1.5 with a 2D example, all spins are oriented toward one specific direction or the opposite of it, and therefore the spin rotational symmetry is broken. The staggered magnetization  $m_s$  is the good order parameter normally used to detect AFM order [21]. The definition of the staggered magnetization in 2D is,

$$\mathbf{m}_s = \sum_{i=1}^N (-1)^{i_x+i_y} \mathbf{S}_i, \quad (1.1)$$

where  $i$  denotes a site and  $N$  is the total number of spins. In a finite system, the direction of non-zero  $\mathbf{m}_s$  is fluctuating. Therefore, the average  $\langle \mathbf{m}_s \rangle = 0$ . In order to detect the

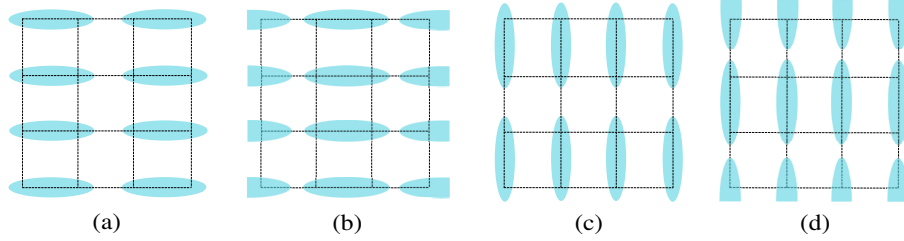


Figure 1.7: A schematic picture to describe four degenerate states (a)-(d) in a VBS.

order of AFM states, we use direction-independent quantities, such as the absolute value of staggered magnetization  $\langle |m_s| \rangle$  or the square of it  $\langle |m_s^2| \rangle$ .

Unlike the AFM states, VBS states conserve the spin-rotational symmetry. As shown in the Fig. 1.6, neighboring spins form singlets (blue ellipses) and the long-range magnetic order is broken ( $m_s = 0$ ). These singlet pairs are called *valence bonds* (VB) in analogy with chemistry. Since the bonds line up in the lattice and form the crystal-like structure, this state is referred as valence bond solid (sometimes called valence-bond crystal). VBS order breaks the translational symmetry and has four degenerate configurations (i.e. ordering in one of them is  $Z_4$  symmetry breaking) in the infinite system. The four degenerate states are demonstrated in Fig. 1.7 as (a)-(d).

A natural way to describe the spin order is to use the *two-spin correlation* function,

$$C(r) = \langle \mathbf{S}_i \cdot \mathbf{S}_{i+r} \rangle. \quad (1.2)$$

For individual configurations in Fig. 1.7,  $C(r)$  will show large and small values according to patterns. However, the average  $C(r)$  will decay exponentially with  $r$  since there is no spin order in the VBS state. The conventional order parameter to describe the VBS state is captured by the *dimer correlation* function  $D(r)$  [31]. In 2D,  $D(r)$  is expressed as,

$$D(r) = \langle C_i C_{i+r} \rangle = \langle (\mathbf{S}_i \cdot \mathbf{S}_{i+\hat{e}})(\mathbf{S}_{i+r} \cdot \mathbf{S}_{i+r+\hat{e}}) \rangle, \quad (1.3)$$

where the  $\hat{e}$  is a unit vector in the  $x$  or  $y$  direction.  $D(r)$  will alternate between strong and weak values in systems with VBS order. Therefore, an empirical indicator to study VBS

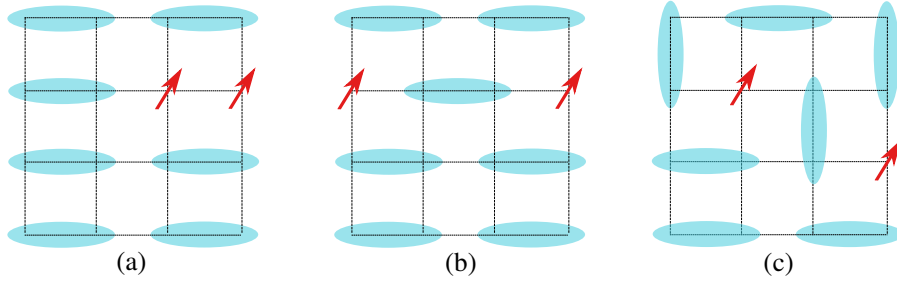


Figure 1.8: A schematic picture of emergent spinons in valence bond solid states (a-b) and the disordered state (c). A pair of spinons could emerge by breaking one singlet and form the triplet pair as shown in red arrows in (a). This pair of spinons could separate in the system and cause a path of misaligned valence bonds in the ordered state (b). Spinons become deconfined and move like free quasi-particles in the disordered state (c).

order is the dimer correlation function difference  $D(r) - D(r - 1)$  [21].

According to the DQC theory, fractional quantum number particles—spinons are condensed in AFM states and confined in VBS states. Near the critical point of the AFM–VBS transition where quantum fluctuations are strong, pairs of spinons would appear as triplet excitations and could move around causing changes of bond configurations in the background of singlets. Fig.1.8 illustrates this in an extreme VBS phase. As shown in Fig. 1.8, the moving of the spinon leaves behind misaligned VBs, which costs energy (for certain Hamiltonians which favor VBS order) and confines the spinons. When the critical point is approached, the VB order is washed away by strong quantum fluctuations and spinons could move effortlessly in the critical state and become deconfined. A demonstration is shown in Fig. 1.8(c), in a disordered state, the “trace” of the spinon movement becomes vague and spinons become deconfined quasi-particles.

## 1.4 Spin liquids

Spin liquids are exotic states, which conserve all symmetries (therefore all local order parameters are zero) but are nevertheless strongly-correlated [32]. Since spins do not form any static order yet are strongly correlated, by the analogy to the molecules in liquids, this

kind of state is called a *spin liquid*. Spin liquids are expected to exist in frustrated magnets. Frustrated magnets are materials which have competing interactions among spins or magnetic moments. Since the system's interactions can not be simultaneously satisfied, this competition leads to the degeneracy of the ground state in corresponding classical systems. When adding quantum fluctuations, these degenerate ground states have collective behavior and give rise to emergent gauge fields and fractional particle excitations.

A well-studied category of classical spin liquids is spin-ice materials [33]. In spin-ices, the f-electron spins locate in the pyrochlore lattice, which have the highly degenerate ground state and long-range spin correlations above the freezing temperature at around 0.5K. The particle excitation in spin-ice is the interesting “monopole”, which was first proposed in theory [34] then discovered in experiments [35].

Different from classical spin liquids, quantum spin liquids (QSL), in which we are more interested in this thesis, should never order even at absolute zero temperature, due to large quantum fluctuations. QSLs provide many interesting research topics in frustrated systems. After Anderson's hypothesis that doped resonating valence bond (RVB) spin liquids might explain the mechanism of high-temperature superconductivity in cuprates [5], QSLs have received even more attention. The RVB is one kind of QSL [36]. The VBs serve as a building block of RVB spin liquids and provide a natural way to describe the ground state of non-magnetic phases. The term “resonating” depicts the fact that driven by quantum fluctuations, VB configurations fluctuate as if they were in resonance. A possible VB configuration is shown in Fig. 1.9. Here we include the long-range VBs as well. Spin liquids could be seen as the superposition of all possible VB configurations, where the short-bond RVB could consist of only nearest neighbor VBs. The elementary excitations of an RVB are emergent spinons as we described in the previous section. Since RVBs are disordered states, spinons are expected to be deconfined [37–39].

Since QSLs have no broken symmetry, it is very hard to study them. In experiments, measuring all local order parameters at low temperature to conclude the absence of any order is very challenging. QSLs could also be characterized by their fractionalized excitations,

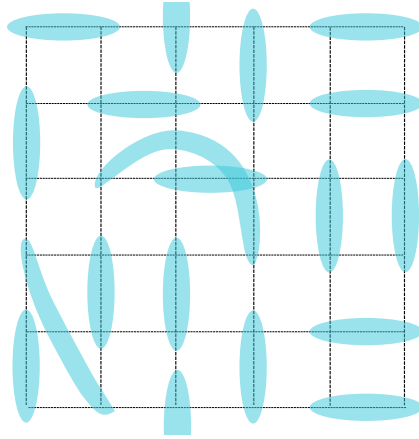


Figure 1.9: A possible configuration of resonating valence bond (RVB) spin liquids. Generally speaking, spin liquids are superpositions of all possible valence bond configurations.

however, the technique to study them in detail was not available till recently: the first strong candidate of QSLs has been characterized by the spinon excitation continuum and short-ranged spin correlations in the antiferromagnetic  $\text{ZnCu}_3(\text{OD})_6\text{Cl}_2$  (herbertsmithite) via inelastic neutron scattering [18]. Theoretically, researchers have realized that besides local order parameters, topological orders could be used to categorize QSLs [15, 40]. Much recent research has focused on searching for QSLs in theoretical models. QSLs have been found on the Kagome lattice with Heisenberg interactions described by the Hamiltonian [17],

$$H = \sum_{\langle ij \rangle} J S_i \cdot S_j, \quad (1.4)$$

and also possibly found in the  $J_1 - J_2$  model ( $H = \sum_{\langle ij \rangle} J_1 S_i \cdot S_j + \sum_{\langle\langle ij \rangle\rangle} J_2 S_i \cdot S_j$ ) on the square lattice as well [15, 16] (though this is currently not widely accepted [41, 42]). For the short-bond RVB spin liquid, the parent Hamiltonian was first proposed by Rokhsar and Kivelson as the quantum dimer model [43]. A version of the RVB spin liquid has been proven to exist at the critical “R–K” point of this model. The parent Hamiltonian of the true quantum RVB, which includes the  $SU(2)$ -invariant spins, was recently proposed by Cano and Fendley [44]. The properties of the ground state of the Cano-Fendley Hamiltonian are in consistence with the numerical results found in the short-bond RVB [45, 46], which

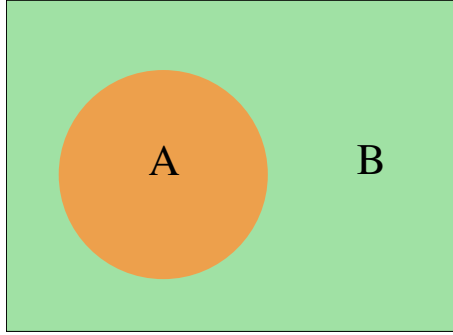


Figure 1.10: A schematic figure showing a system divided into two subsystems  $A$  and  $B$ .

we study in detail in this thesis.

## 1.5 Entanglement entropy

Entanglement, as a key resource in quantum information, has provided exciting insights to study strongly correlated many-body systems [47]. The measure of entanglement between two regions  $A$  and  $B$  is given by the *entanglement entropy*, which is able to capture the hidden order in long-range entangled states, e.g., the QSL. This hidden order usually has interesting topological properties [48, 49].

The most commonly used entropy is the *von Neumann* entropy. For any quantum system with pure state  $|\Psi\rangle$ , the density matrix  $\rho$  is written as  $\rho = |\Psi\rangle\langle\Psi|$ . If we divide the system into two subsystems  $A$  and  $B$  (as shown in Fig. 1.10), the *von Neumann* entropy is written as,

$$S_A = -\text{Tr}\rho_A \ln(\rho_A), \quad (1.5)$$

where  $\rho_A$  is the *reduced density matrix*  $\rho_A = \text{Tr}_B \rho$ , which is obtained by tracing out the degrees of freedom in subsystem  $B$ .

A generalized form of the entanglement entropy is *Renyi entropy*, which is written as,

$$S_n(\rho_A) = \frac{1}{(1-n)} \ln[\text{Tr}(\rho_A^n)]. \quad (1.6)$$

In the limit of  $n \rightarrow 1$ , it reduces to the *von Neumann* entropy  $S_1$ . It has been shown that, for any two Renyi entropies  $S_n$  and  $S_m$ , if  $n < m$ ,  $S_n \geq S_m$  [50]. Therefore, higher order Renyi entropies are smaller than the *von Neumann* entropy. Apart from their different values, the Renyi entropies have similar properties. One of the key properties of Renyi entropies is their scaling behavior near criticality, which provides universal signatures of critical points. Near the critical region of the 1D Heisenberg spin system and other related spin chains, the Renyi entropy scales as [51],

$$S_n = \frac{c}{6} \left(1 + \frac{1}{n}\right) \ln\left(\frac{L}{\pi} \sin\left(\frac{\pi x}{L}\right)\right), \quad (1.7)$$

where  $L$  is the chain length and  $x$  is the length of the subsystem A in the chain. The constant  $c$  is called the *central charge*, which is a universal number underlying the conformal field theory. The quantity  $\frac{L}{\pi} \sin\left(\frac{\pi x}{L}\right)$  in Eq.(1.7) is called the “chord length”.

In 2D spin systems, the scaling function of the gapped spin liquid is of the form,

$$S_n = al - \gamma, \quad (1.8)$$

where  $l$  is the length of the boundary that separates system A and B. (For example, in Fig. 1.10,  $l$  is the circumference of A.)  $\gamma$  is the topological constant that sheds light on the topological properties of systems [48, 49]. The negative sign in front of  $\gamma$  indicates that, there is a reduction of entanglement because of the topological constraint. The leading term of this 2D scaling function is proportional to the boundary length  $l$ , which is referred as “area law” scaling [52]. The “area law” (also called boundary law) is the leading term in the scaling function of 2D gapless system as well [40]:

$$S_n = al - b \log(l) - c \log\left(\frac{L}{\pi} \sin\left(\frac{\pi x}{L}\right)\right). \quad (1.9)$$

The first correction is a logarithmic correction to the boundary length  $l$ ; the second correction gives the scaling function of the system size  $L$  with the *central charge*  $c$  as a coefficient in front. In a 2D periodic square lattice,  $L$  is the system size,  $l$  is the boundary length of

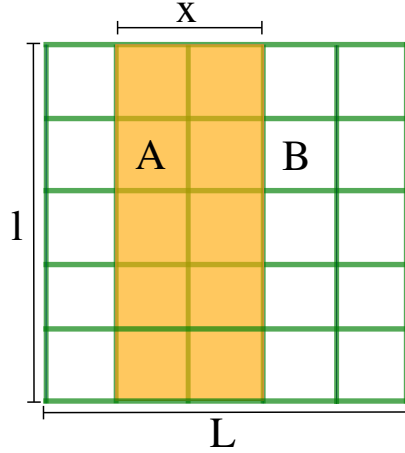


Figure 1.11: A illustrative sketch to explain variables in the scaling function of the Renyi entanglement entropy in Eq.(1.9) on a 2D square lattice. The periodic boundary condition is applied in both directions.

the toric region  $A$ , and  $x$  is the width of torus  $A$ . An illustrative sketch of these variables are shown in Fig. 1.11.

Numerically, the most natural way to calculate the entanglement entropy is to use the Density Matrix Renormalization Group (DMRG) method. It is because DMRG could compute the density matrix  $\rho$  from wavefunctions generated in the calculation directly. However, this numerical method is limited to small 2D systems, as the area law of the entanglement is difficult to deal with because the method is based on a 1D representation of the system. Recently as a breakthrough, the measurement of the second or higher order Renyi entropies in 2D becomes available in the large scale Quantum Monte Carlo (QMC) simulations [50]. In this thesis, we will use QMC to study the second order Renyi entropy of 1D spin wavefunctions, which without a Hamiltonian, cannot be directly studied by DMRG.

## 1.6 Thesis outline

The structure of this thesis is as follows:

Chapter 2 provides an overview of numerical methods and computational techniques used in this thesis. I will discuss properties of the valence bond (VB) basis and calculations

of correlation functions in the VB basis in detail. I will also introduce Monte Carlo sampling methods in the VB basis. Moreover, I will introduce the VB projector quantum Monte Carlo (QMC) algorithm and explain its application to study spinon excitations. I will also briefly discuss the “measurement” of Renyi entanglement entropy in QMC.

Chapter 3 is devoted to study spinons in 1D and 2D quantum spin systems. I will introduce a technique to characterize spinons in terms of their size and confinement length. I present spinon results in a variety of quantum spin models, e.g., the Heisenberg chain, the Heisenberg 2-leg ladder and JQ models in one and two dimensions. I will address observations which are relevant to the deconfined quantum criticality.

In chapter 4, I present a comprehensive study of properties of Resonating Valence Bond (RVB) spin liquids. One highlight of this work is that we define RVB spin liquids as critical VBS states; another highlight is that we propose a plausible mapping of RVB to classical dimer models through studies from classical continuum field theory (the height model).

Chapter 5 focuses on a generalized form of VB states—amplitude-product (AP) states [53]. AP states are a prototype of variational singlet wave functions that could be efficiently constructed as ground states for certain Hamiltonian. I will introduce the AP states in detail. In 1D, I discuss the Néel to VBS phase transition reached by tuning amplitudes of the AP states. I also measure the Renyi entropy of the AP states and draw a conclusion about state classification based on the central charge values.

In chapter 6, I will summarize the main results in this thesis work, provide some future hypotheses and discuss open questions that need to be further explored.

## Chapter 2

# Quantum Monte Carlo Methods and Measurements

It is very challenging to solve Hamiltonian for quantum system analytically, one reason is because the Hilbert space grows exponentially with system size. When the system has relatively large number of particles, e.g. 10 electrons, it becomes impossible to calculate all eigenstates manually. Therefore, computational methods for solving quantum problems are very valuable and worth continuously developing efforts to meet new challenges.

In this thesis, we focus on one of the most powerful computational methods — Monte Carlo algorithms [54]. The Monte Carlo algorithm was first invented by physicist Stanislaw Ulam at Los Alamos National Laboratory in late 1940s, named by Nicholas Metropolis and implemented by John von Neumann [55]. The central idea of Monte Carlo is to use random sampling based on some given probability distribution to compute numerical expectation values of observables. For details of Monte Carlo method, we refer readers to the book Ref. [56].

After Feynman introduced path integrals to formulate the quantum statistical mechanics [57], the generalization of Monte Carlo algorithms to quantum Monte Carlo methods became possible. It was shown that the quantum systems could be mapped onto a  $(d + 1)$ -dimensional classical systems by identifying the sampling weight of a space-time path in quantum statistical mechanics [10]. Therefore, *quantum Monte Carlo* (QMC) could be seen

as a generalization of classical Monte Carlo methods in  $(d + 1)$  dimensions. However, there is a big difference between classical and quantum Monte Carlo simulations — due to the non-zero off-diagonal wavefunction overlaps in samplings of quantum states, in fermionic or frustrated quantum systems, QMC has negative weights (the so called “sign problems”) which is prohibited in the space-time sampling [58, 59]. Though there are many techniques to make QMC work without the serious sign issue to some extent [60], solving the fermionic or frustrated problems in 2D systems at low temperature is still one of the most challenging puzzles in computational physics. Luckily, without the notorious negative sign, there is still a wealth of interesting physics to explore. In this thesis, we focus on unfrustrated bosonic (strictly speaking spin) problems, where QMC contributes as the most efficient and powerful numerical method nowadays.

In this chapter, we first introduce the properties of valence-bond states and Monte Carlo sampling techniques in Sec.2.1. Then we introduce a QMC method — valence-bond projector QMC in Sec.2.2, which serves as a state-of-the-art method in solving ground states of unfrustrated spin systems. We also generalize this method to implement simulations of quantum fractional excitation, i.e. spinons. Lastly, we introduce the measurement of second Renyi entropy with the Monte Carlo method in Sec.2.3.

## 2.1 Sampling of valence bond states

In this section, we firstly introduce the definition of valence-bond states in Sec.2.1.1 and the concept of transition graph in Sec.2.1.2. Then we discuss correlation functions based on transition graphs in clear mathematical forms in Sec.2.1.3. In Sec.2.1.4, we discuss two Monte Carlo sampling methods — two-bond updates and loop updates, together with spin updates in a complete Monte Carlo sweep. We discuss the sampling of valence-bond states with monomers as well.

### 2.1.1 Valence bond basis

We consider the standard bipartite valence bond basis, where a state of  $N$  (an even number of) spins on a bipartite lattice,

$$|V_\alpha\rangle = \frac{1}{2^{N/4}} \prod_{i=1}^{N/2} (|\uparrow_i \downarrow_{\alpha(i)}\rangle - |\downarrow_i \uparrow_{\alpha(i)}\rangle), \quad (2.1)$$

is a product of singlets, where the first spin  $i$  of each singlet is on sublattice  $A$  and the second spin  $\alpha(i)$  is on sublattice  $B$ . With the  $B$  sites also labeled as  $1, \dots, N/2$ , the set  $\alpha(1), \dots, \alpha(N/2)$  is a permutation of these numbers and the label  $\alpha = 1, \dots, (N/2)!$  in  $|V_\alpha\rangle$  simply refers to all these permutations. The signs of the expansion coefficients of this state in the standard  $\uparrow, \downarrow$  spin basis correspond to Marshall's sign rule for the ground state  $|\Psi_0\rangle$  of a bipartite system [61], i.e.,

$$\text{sign}[\Psi_0(S_1^z, \dots, S_N^z)] = (-1)^{n_{A\downarrow}}, \quad (2.2)$$

where  $n_{A\downarrow}$  is the number of  $\downarrow$  spins on sublattice  $A$ .

An *amplitude-product* state [53] is a superposition of valence bond states,

$$|\Psi\rangle = \sum_{\alpha} \psi_{\alpha} |V_{\alpha}\rangle, \quad (2.3)$$

where the expansion coefficients are products of amplitudes  $h(\mathbf{r}_{\alpha,i})$  corresponding to the “shape” of the bonds (the bond lengths in the  $x$  and  $y$  direction in the case of a 2D system);

$$\psi_{\alpha} = \prod_{i=1}^{N/2} h(\mathbf{r}_{\alpha,i}). \quad (2.4)$$

An important special case is the extreme RVB state made up of only bonds of length 1 (one lattice constant), in which case the expansion coefficients  $\psi_{\alpha}$  are the same for all configurations. We will later study this state, as well as a case including the bipartite bonds of length  $\sqrt{5}$  lattice constants, examples of which are seen in Fig. 2.1. We will also study states with no restriction on the bond length. The discussion here will be framed around generic bipartite amplitude-product states, with no restriction on the bond lengths.

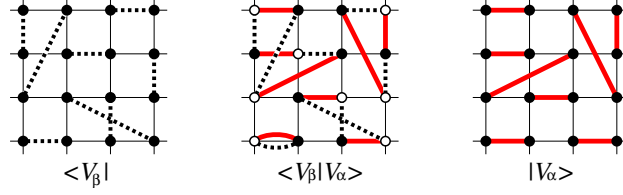


Figure 2.1: Two valence-bond states (left and right) in two dimensions and their transition graph formed by superimposing the two bond configurations (center). One of the spin configurations compatible with the transition graph is also shown, with open and solid circles for  $\uparrow$  and  $\downarrow$  spins. Each loop has two such allowed staggered spin configuration, and the overlap of two valence-bond states is thus  $\langle V_\beta | V_\alpha \rangle = 2^{n_{\alpha\beta} - N/2}$ , here with the number of loops  $n_{\alpha\beta} = 4$  and the number of spins  $N = 16$ .

### 2.1.2 Transition graphs

An important concept in the valence-bond basis is the transition graph formed when the bond configurations of the two states are superimposed [53, 62, 63]. This is illustrated in Fig. 2.1. The overlap  $\langle V_\beta | V_\alpha \rangle$  between two valence-bond basis states can be simply expressed in terms of the number  $n_{\alpha\beta}$  of loops in the transition graph.

The easiest way to calculate the overlap is to go back to the standard basis of  $\uparrow$  and  $\downarrow$  spins, so that

$$\langle V_\beta | V_\alpha \rangle = \frac{1}{2^{N/2}} \sum_{S_\alpha^z} \sum_{S_\beta^z} (-1)^{n_{\alpha, A\downarrow} + n_{\beta, A\downarrow}} \times \langle S_{\beta 1}^z, \dots, S_{\beta N}^z | S_{\alpha 1}^z, \dots, S_{\alpha N}^z \rangle, \quad (2.5)$$

where  $S_\alpha^z$  and  $S_\beta^z$  denote spin configurations compatible with the bond configurations  $V_\alpha$  and  $V_\beta$ , i.e., those that have spins  $\uparrow\downarrow$  or  $\downarrow\uparrow$  on each bond. Terms with any occurrence of  $S_{\alpha i}^z \neq S_{\beta i}^z$  of course vanish, and the double sum, thus, simply counts the number of spin configurations common to the two bond configurations. Since the spins on each bond are antiparallel, the spins along a loop of alternating  $V_\alpha$  and  $V_\beta$  bonds (i.e., the loops in the transition graph) must alternate in a staggered,  $\uparrow\downarrow\uparrow\downarrow \dots$ , pattern. There are two such configurations for each loop. The total number of contributing spin configurations is

therefore  $2^{n_{\alpha\beta}}$ , giving the overlap

$$\langle V_\beta | V_\alpha \rangle = 2^{(n_{\alpha\beta} - N/2)}, \quad (2.6)$$

which replaces the orthonormality condition  $\langle \beta | \alpha \rangle = \delta_{\alpha\beta}$  for an orthonormal basis. For bond tilings  $V_\alpha = V_\beta$ , we have  $n_{\alpha\beta} = N/2$  and the overlap equals unity.

In calculations with superpositions  $|\psi\rangle$  of valence-bond states, such as amplitude-product states, it is often not practical to normalize the states. It is convenient to write operator expectation values in the form

$$\begin{aligned} \langle \Psi | O | \Psi \rangle &= \frac{\sum_{\alpha\beta} \psi_\beta \psi_\alpha \langle V_\beta | O | V_\alpha \rangle}{\sum_{\alpha\beta} \psi_\beta \psi_\alpha \langle V_\beta | V_\alpha \rangle} \\ &= \frac{\sum_{\alpha\beta} \psi_\beta \psi_\alpha \langle V_\beta | V_\alpha \rangle \frac{\langle V_\beta | O | V_\alpha \rangle}{\langle V_\beta | V_\alpha \rangle}}{\sum_{\alpha\beta} \psi_\beta \psi_\alpha \langle V_\beta | V_\alpha \rangle}. \end{aligned} \quad (2.7)$$

Defining the weight  $W_{\alpha\beta}$  for the combined bond configuration  $V_\alpha, V_\beta$  and the normalized matrix element  $O_{\alpha\beta}$  according to

$$W_{\alpha\beta} = \psi_\beta \psi_\alpha \langle V_\beta | V_\alpha \rangle, \quad (2.8)$$

$$O_{\alpha\beta} = \frac{\langle V_\beta | O | V_\alpha \rangle}{\langle V_\beta | V_\alpha \rangle}, \quad (2.9)$$

the expectation value takes the form appropriate for use with the Monte Carlo sampling methods that we will discuss below in Sec. 2.1.4;

$$\langle \Psi | O | \Psi \rangle = \frac{\sum_{\alpha\beta} W_{\alpha\beta} O_{\alpha\beta}}{\sum_{\alpha\beta} W_{\alpha\beta}}. \quad (2.10)$$

The weight  $W_{\alpha\beta}$ , which is used in sampling the states in Monte Carlo simulations, is positive-definite when we consider wave functions satisfying Marshall's sign rule, i.e., the amplitudes  $h(\mathbf{r}_{\alpha,i}) \geq 0$  in (2.4).

Like the overlap of the valence-bond states, the matrix elements of operators of interest can typically also be expressed in terms of the loops of the transition graph of the bond configuration  $V_\alpha, V_\beta$ . We discuss spin and dimer correlations next.

### 2.1.3 Correlation functions

We have already introduced correlation functions in Sec.1.3. Here we compute them in detail in the context of the transition graph and write them in simple expressions, which could be implemented in simulations directly.

The standard spin-spin correlation function is most easily obtained by reintroducing the spins in the transition graph, as illustrated in Fig. 2.1. We can then use the fact that

$$\langle V_\beta | \mathbf{S}_i \cdot \mathbf{S}_j | V_\alpha \rangle = 3 \langle V_\beta | S_i^z S_j^z | V_\alpha \rangle, \quad (2.11)$$

where the latter is diagonal and easy to compute in the  $z$ -spin basis. When summing over the allowed spin states, i.e., the two “orientations” of each loop (for a total of  $2^{n_{\alpha\beta}}$  spin states), it is clear that  $S_i^z S_j^z$  averages to zero if  $i$  and  $j$  are in different loops, whereas for  $i, j$  in the same loop we get  $\pm \frac{1}{4} \langle V_\beta | V_\alpha \rangle$ , with the sign depending on whether the spins are in the same (+ sign) or different (− sign) sublattices. Introducing the notion  $(i, j)_L$  for two spins in the same loop and  $(i)_L(j)_L$  for spins in different loops, we can write the matrix element ratio in (2.10) corresponding to the spin correlation function as

$$C(r) = \frac{\langle V_\beta | \mathbf{S}_i \cdot \mathbf{S}_j | V_\alpha \rangle}{\langle V_\beta | V_\alpha \rangle} = \begin{cases} 0, & (i)_L(j)_L \\ \frac{3}{4} \phi_{ij}, & (i, j)_L, \end{cases} \quad (2.12)$$

where  $\phi_{ij}$  is the staggered phase factor;

$$\phi_{ij} = \begin{cases} -1, & \text{for } i, j \text{ on different sublattices,} \\ +1, & \text{for } i, j \text{ on the same sublattice.} \end{cases} \quad (2.13)$$

While the loop-expression (2.12) for the simple spin-spin correlation function is well known [53, 62, 63], the general form of a four-spin correlation (of which the dimer-dimer correlator of interest here is a special case) was only derived recently [31]. In Appendix A we discuss this derivation in a slightly different way, which is less convenient when generalizing to higher-order correlators (which was also done in Ref. [31]), but more transparent in the case of the four-spin correlator. The resulting general formula for any non-zero four-spin

matrix element is

$$\begin{aligned}
 D(r) &= \frac{\langle V_\beta | (\mathbf{S}_k \cdot \mathbf{S}_l) (\mathbf{S}_i \cdot \mathbf{S}_j) | V_\alpha \rangle}{\langle V_\beta | V_\alpha \rangle} \\
 &= \begin{cases} \left( \frac{9}{16} - \frac{3}{4} \delta_{kl}^{ij} \right) \phi_{ij} \phi_{kl}, & (i, j, k, l)_L, \\ \frac{9}{16} \phi_{ij} \phi_{kl}, & (i, j)_L (k, l)_L, \\ \frac{3}{16} \phi_{ij} \phi_{kl}, & (i, k)_L (j, l)_L, \\ \frac{3}{16} \phi_{ij} \phi_{kl}, & (i, l)_L (j, k)_L. \end{cases}
 \end{aligned} \tag{2.14}$$

Here we have generalized the notation of (2.12) for how the sites are distributed among loops in a straight-forward way, with indices within the same parentheses belonging to the same loop. In the case of the single-loop contribution,  $(i, j, k, l)_L$ , the term  $\delta_{kl}^{ij} \in \{0, 1\}$  depends on the order of the four indices within the single loop, as specified in Eq. (A.9) of Appendix A.

#### 2.1.4 Monte Carlo sampling of valence bond states

A simple but powerful Monte Carlo sampling algorithm for amplitude-product states based on reconfiguration of bond pairs was presented some times ago by Liang *et al.* [53], who used this method to study the spin-spin correlations in amplitude-product states with several different forms of the amplitudes (exponentially or power-law decaying with the length of the bond). A more efficient algorithm using loop updates was developed recently which operates in a combined basis of both valence bonds and spins [64]. The two-bond update, as well, can be made more efficient by working in this combined basis. Here we briefly review these two algorithms, and also discuss the topological winding numbers that can be used to classify the bond configurations.

##### 2.1.4.1 Combined bond-spin basis

Monte Carlo sampling of valence bonds involves making some change in the bra and ket bond configurations  $V_\alpha$  and  $V_\beta$ , and accepting or rejecting the update based on the change in the sampling weight (2.8), according to some scheme satisfying detailed balance. Working with the standard non-orthogonal valence-bond basis and using the Metropolis algorithm,

we need to compute the weight ratio appearing in the acceptance probability

$$P_{\text{accept}} = \min \left[ \frac{W_{\alpha'\beta'}}{W_{\alpha\beta}}, 1 \right], \quad (2.15)$$

where the primes indicate the new states after some changes have been made in either bond configuration  $V_\alpha$  or  $V_\beta$  (or both, but typically one would change only one state at a time).

The weight ratio using (2.8) is

$$\frac{W_{\alpha'\beta'}}{W_{\alpha\beta}} = \frac{\psi_{\alpha'}\psi_{\beta'}}{\psi_\alpha\psi_\beta} 2^{(n_{\alpha'\beta'} - n_{\alpha\beta})}. \quad (2.16)$$

For an amplitude-product state, the ratio of the wave function coefficients is trivial, but computing the change  $n_{\alpha'\beta'} - n_{\alpha\beta}$  in the number of loops in the transition graph can be time consuming, as it involves tracing loops that can be long.

The loops are typically long,  $\mathcal{O}(N)$ , if there is antiferromagnetic long-range order [64]. That is not the case for the short-bond RVB states studied in this paper, but nevertheless it is more efficient to avoid the loop-counting step. That can simply be done by expressing each singlet in the standard basis of  $\uparrow$  and  $\downarrow$  spins, and sampling these spin configurations in addition to the bond configurations [and since the spin basis is orthonormal, the sampled (non-zero weight) spin configurations must be the same in the bra and the ket]. That is, the configurations being sampled consist of a direct product of *two* valence bond patterns  $V_\alpha$  and  $V_\beta$ , as well as one spin configuration  $Z_{\alpha\beta}$  compatible with both  $\alpha$  and  $\beta$  (i.e. one  $\uparrow$  and one  $\downarrow$  spin on each bond). Each loop in the transition graph must consist of an alternating string  $\uparrow\downarrow\uparrow \dots \downarrow$  and, for every loop, there are two choices for this string. Thus, the ratio of the number of spin configurations is equal to the factor  $2^{(n_{\alpha'\beta'} - n_{\alpha\beta})}$  in Eq. (2.16). The Monte Carlo sampling of the spin configurations compatible with the bond configurations therefore automatically takes care of the factor  $2^{n_{\alpha\beta}}$  in Eq. (2.16), with no need to generate a transition graph or count loops. For more details of the arguments leading to this conclusion, see Ref. [64].

### 2.1.4.2 Monte Carlo sampling

Here we outline the two different bond sampling algorithms that we used, each of which comes in a simple version for the classical bond configuration as in classical dimer models (CDM), as well as a generalization for the combined spin-bond basis for the RVB amplitude-product states. In the case of the RVB, the spin configurations also have to be updated. We also introduce a simple extension to sample states with monomers (empty sites).

The two updating algorithms are summarized using simple examples with short bonds in Figs. 2.2(a,b), with (c) showing the extension needed for also sampling monomer configurations. For either algorithm, updates are alternated between the ket and bra configurations, and there is an additional step for updating the spin configuration, where all the spins belonging to randomly chosen individual loops in the transition graph are flipped.

#### 2.1.4.2.1 Two-bond update

For the two-bond update, as in Ref. [53] we choose two sites on the same sublattice (normally a next-nearest-neighbor site pair) and exchange their dimers in the unique way maintaining the  $A - B$  sublattice connectivity, as shown in Fig. 2.2(a). The update can be accepted only if the spin configuration is compatible with the new bond structure, i.e., only antiparallel spins are connected by the bonds. In the case of the extreme short-bond RVB, an allowed new configuration is always accepted, as the wave function ratio in (2.16) trivially equals one, whereas in general, when longer bonds are present, a ratio involving the amplitudes of two bonds has to be computed to determine the Metropolis acceptance rate (2.15).

The algorithm for the CDM is simpler, as there is no spin state in that case. In the case of short bonds, an update of two bonds [flipping a pair of parallel bonds as in Fig. 2.2(a)] is then always accepted, whereas in the presence of longer bonds the acceptance probability involves the ratio of bond fugacities. We here consider only two bond lengths (nearest neighbor and fourth-nearest neighbor bonds, as shown in Fig. 2.1), with fugacities  $Z_1(i) = 1$  and  $Z_2(i)$ , respectively, for bonds connected to site  $i$  (taken to be the sublattice A site, for

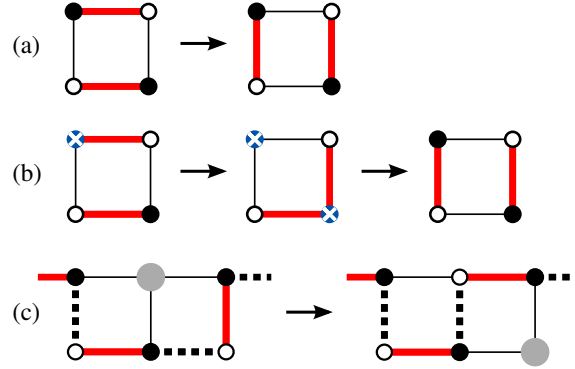


Figure 2.2: Monte Carlo updates for the RVB state in the combined spin-bond basis. Open and solid circles represent  $\uparrow$  and  $\downarrow$  spins. In the basic moves (a) and (b), only one of the two two valence bond configurations is affected at a time. (a) A simple two-bond update. Choosing two sites on the same sublattice, the two bonds connected to them can be reconfigured in a unique way. If the spins are compatible with the  $\uparrow, \downarrow$  singlet restriction, this update can be accepted. (b) Loop-cluster update. Choosing an arbitrary starting site (in this example in the left-upper corner) two defects (a site with no dimer or two dimers connected to it, both indicated with an  $\times$ ) are generated by moving the end of the dimer on the initial site to another site which satisfies the bond-length constraint (here, in the extreme short-bond RVB, the length is always one) and the spin-singlet compatibility (anti-parallel spins on the bond). The dimer that was previously connected to this site is then moved away from the double-bond defect to another site. This process continues until a bond returns back to “annihilate” the original empty-site defect, which here happens already after two bond moves [the last step in (b)]. In both (a) and (b), we only show the bonds of the configuration involved in this update. (c) Monomer update. Monomers are shown as larger circles and must appear in the same locations in the state  $|V_\alpha\rangle$  and  $|V_\beta\rangle$ , the bonds of both of which are shown here (as solid and dashed lines). In addition to the two-bond or loop update of the bonds, monomers can move to a site on the same sublattice by also moving a bond which is common to the two valence bond states.

definiteness). The partition function is then given by

$$Z_{CDM} = \sum_C Z_2^{n_2(C)} \quad (2.17)$$

where  $n_2(C)$  is the number of long bonds in configuration  $C$ . The acceptance probability for an update of bonds on sites  $i$  and  $j$  is

$$P_{\text{acc}} = \min \left[ \frac{Z_{\text{new}}(i)Z_{\text{new}}(j)}{Z_{\text{old}}(i)Z_{\text{old}}(j)}, 1 \right], \quad (2.18)$$

where "old" and "new" correspond to the length-index 1 or 2 before and after the bond reconfiguration.

For both the RVB and CDM, this algorithm keeps the system in a sector of fixed winding number, which we can take advantage of if we want to study properties in the individual sectors. Suitable starting configurations for different winding number sectors are shown in Fig. 4.1.

#### 2.1.4.2.2 Loop update

If we want the system to wander among the different topological sectors, we instead use the loop-cluster update, which is a simple extension of a loop update for the CDM [65, 66]. It is also in general more efficient (exhibits shorter autocorrelation times) than the two-bond update for large size system. To start the loop update, we pick a site at random; in the example in Fig. 2.2(b) the top left site. We move the dimer connected to it, thus creating two defects in the system. We keep the starting site as a vacancy and move the original dimer of the now doubly occupied site to a new site, with certain probabilities satisfying detailed balance, and constrained by the spin configuration so that spins are opposite on every dimer. In the case of short bonds only, the probabilities are equal for the three new neighbor sites. For the general case where longer bonds are included, we refer to Ref. [66] for efficient choices of the probabilities. This update moves the doubly-occupied defect to a new site, which in 2.2(b) is the lower-right site. We keep moving this defect using the above procedures, until it happens that the two defects annihilate each other, which means that bonds have been moved on a closed loop of sites. A sweep of bond updates is defined

as the construction of a fixed number of loops (determined during the equilibration part of the simulation) which on average result in  $\approx N$  moved bonds in both the ket and the bra state.

#### 2.1.4.3 Spin update

After updating the bond configurations with one of the above algorithms, we update the spin configuration by flipping the spins of randomly selected loops of the transition graph (such as those in the middle graph of Figs. 2.1), with probability  $1/2$  for each loop. All the loops have to be traversed, by moving between spins according to the bonds (which are stored in the computer as bidirectional links), alternating between bonds in the bra and ket state. Each site visited is flagged and no new loops are started from already visited sites. The computational cost of a full sweep of such updates (visiting each site once) is  $\mathcal{O}(N)$ .

#### 2.1.4.4 Monte Carlo sweep

A sequence of bond updates in which  $\mathcal{O}(N)$  bonds are affected followed by a complete spin update constitutes one Monte Carlo (MC) sweep, which has a total computational cost  $\mathcal{O}(N)$ . Note that the sampling algorithm without the spins potentially costs up to  $N^2$  steps per sweep, since each two-bond update requires loop-traversals to check whether two loops are joined or a single loop is split [53], and the loop length can then be up to  $\mathcal{O}(N)$  (in a Néel state). The same issue pertains to loop updates in the pure valence-bond basis as well.

#### 2.1.4.5 Sampling with monomers

We are also interested in the distribution of two monomers in the RVB states. In the case of the CDM, the distribution function of the monomer separation can be measured just by keeping track of the two defects [65,66], but in the RVB we have to explicitly introduce two monomers by removing both spins on a randomly chosen valence bond which is common to both the ket and bra bond configurations. Note that valence bond states with monomers are orthogonal unless the monomers are at the same locations in both states. We use the

loop algorithm to sample the bond configuration space, and periodically we also move the monomers. Such a move can be done in combination with the move of a valence bond that is common to the two states, as shown in Fig. 2.2(c). This can always be accepted if there is no change in the bond length (one could also consider updates where a monomer moves and a bond length changes, which we do not do here). We update the position of two monomers in turn after each sweep of bond updates, when possible, and measure the distribution probabilities  $M(\mathbf{r})$  as a function of distance  $\mathbf{r}$  between the two monomers.

Note that if we assign spins to the monomer the situation is different, due to the over-completeness of the basis. In a system with, e.g., two unpaired  $\uparrow$  spins, these two spins do not have to be located at the same sites in the ket and bra state—for a non-zero overlap it is only required that they are pairwise connected by valence bonds in the transition graph (which now contains two broken loops with open ends terminated by the unpaired spins). Such states with unpaired spins should be related to spinons [67], which we will discuss in detail in Sec.2.2.5. Recently, valence bond states including unpaired spins have also been studied in different systems [68, 69].

## 2.2 Projector Monte Carlo with valence bond states

Projector Monte Carlo (PMC) method is a powerful method for studying the ground state of certain Hamiltonians at zero temperature [64]. In this section, we will introduce the basic idea of PMC with valence-bond basis and extend this QMC method to study spinon excitations.

### 2.2.1 Basic ideas of Projector Monte Carlo

The central idea of projection methods is based on the expression,

$$(-H)^m |\Psi\rangle_t = \psi_0 (-E_0)^m [|\Psi_0\rangle + \sum_{n>0} \frac{\psi_n}{\psi_0} \left(\frac{E_n}{E_0}\right)^m |\Psi_n\rangle], \quad (2.19)$$

where  $|\Psi\rangle_t$  is a trial wavefunction, which could be written as the superposition of all singlet

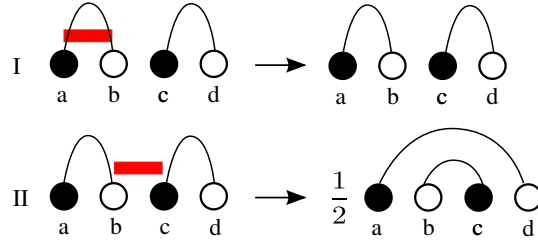


Figure 2.3: An illustration of how the singlet projector (the red rectangle) works. In the top panel I, singlet projector  $C_{ab}$  acts on the singlet  $(a, b)$  and leave the configuration unchanged. In the bottom panel II, singlet projector acts on sites  $c$  and  $b$ , and projects out the singlet  $(c, b)$  with the rearrangement of new bond  $(a, d)$ . The weight of this reconfiguration is  $1/2$ .

eigenstates, i.e.  $|\Psi\rangle_t = \sum_{n \geq 0} \psi_n |\Psi_n\rangle$ . When the power  $m$  is very large and coefficient  $(\frac{E_n}{E_0})^m \ll 1$ , only the first term — the ground state  $|\Psi_0\rangle$  remains.

Here we will start with the *Heisenberg model* on 2D bipartite square lattice as an example to illustrate PMC method. The Heisenberg model could be written as,

$$H = - \sum_{\langle a, b \rangle} C_{ab}, \quad C_{ab} = \frac{1}{4} - S_a S_b, \quad (2.20)$$

where  $\langle a, b \rangle$  labels the nearest spin sites on sublattice  $a$  and  $b$ .  $C_{ab}$  is the singlet projector, which acts on valence-bond states like,

$$\begin{aligned} C_{ab}(a, b)(c, d) &= (a, b)(c, d) \\ C_{cb}(a, b)(c, d) &= \frac{1}{2}(a, d)(c, b). \end{aligned} \quad (2.21)$$

Here  $(a, b)$  and  $(c, d)$  denote singlet pairs. The singlet is always connected from sublattice A to sublattice B, to be in consistency with Marshall's sign rule. As shown in Eq. (2.21) and Fig. 2.3, the singlet projector  $C_{ab}$  does not change the bond configuration if it acts on a singlet pair; if  $C_{ab}$  acts on spins in difference bonds (e.g.  $c$  and  $d$  in Fig. 2.3), it projects out the singlet state between these two spins and reconfigure the bond connection with a weight  $\frac{1}{2}$ . This behavior of singlet operators could be easily proved in spin basis.

Therefore, the  $(-H)^m$  in the projection equation Eq. (2.19) could be written as,

$$(-H)^m = \left( \sum_{r=1}^N C_{a_r b_r} \right)^m = \sum_r \prod_{n=1}^m C_{a_r^n b_r^n} = \sum_r S_r, \quad (2.22)$$

where  $r$  labels the local Hamiltonian at position  $r$  and  $S_r$  is the local operator string with power  $m$ . For any observable  $\hat{O}$ , the measurement of which in the ground state is expressed as,

$$\langle O \rangle = \frac{{}_t \langle \Psi | (-H)^m O (-H)^m | \Psi \rangle_t}{{}_t \langle \Psi | (-H)^{2m} | \Psi \rangle_t} = \frac{\sum_{\alpha\beta lr} W_{lr}^{\alpha\beta} O_{lr}^{\alpha\beta}}{\sum_{\alpha\beta lr} W_{lr}^{\alpha\beta}}. \quad (2.23)$$

where  $l, r$  label two strings of operators,  $\alpha, \beta$  label the superposition of trial wave functions (as in Eq. 2.3). The expectation value is similar as in Eq.(2.9), the weight  $W_{lr}^{\alpha\beta}$  is written,

$$W_{lr}^{\alpha\beta} = \psi_\alpha \psi_\beta \langle V_\alpha(l) | V_\beta(r) \rangle 2^{-(o_\alpha^l o_\beta^r)}. \quad (2.24)$$

$\psi_\alpha, \psi_\beta$  are coefficients before valence-bond states,  $o_l^\beta, o_r^\alpha$  are the number of off-diagonal singlet operator in the operator string  $S_l$  and  $S_r$ , which reconfigure bond structures (as shown in Eq.(2.21)). The expectation value could be measured by doing the importance sampling of  $W_{lr}^{\alpha\beta}$ . However, from Eq.(2.24), we see that the weight depends on the string of operators and valence-bond states. Any local change will request a complete propagation of valence-bond states and recounting of the number of off-diagonal singlet operators, which is computationally inefficient.

We here could use the combined bond-spin basis as discussed in Sec.2.1.4.1, together with the loop-update approach to significantly improve the computational speed from  $\max(m^2, mN)$  to  $\max(N, m)$ . Similar as connecting two valence-bond states alternatively till it goes back to the original point as we discuss in Sec. 2.1.4.2.2, in PMC, loop-update is to connect operators to form closed loops and update them together (we will discuss more about this part in the following section). This could be done efficiently by separating singlet operator  $C_{ab}$  into diagonal (1) and off-diagonal (2) terms,

$$C_{ab}(1) = \frac{1}{4} - S_a^z S_b^z \quad (2.25)$$

$$C_{ab}(2) = -\frac{1}{2}(S_a^+ S_b^- + S_a^- S_b^+). \quad (2.26)$$

The expectation value of these two operators are either  $\pm 1/2$  when two spins are antiparallel or 0 when spins are parallel.

Now in the operator string  $S_r$ , instead of inserting singlet operator  $C_{ab}$ , we insert either  $C_{ab}(1)$  or  $C_{ab}(2)$  into the propagation path to have operator string  $S_r^e$ .  $e$  labels the  $2^m$  combinations of the  $C_{ab}(1)$  and  $C_{ab}(2)$  operators. Since we also include the spin configuration  $Z_{\alpha\beta}$  in our basis,  $C_{ab}(1)$  and  $C_{ab}(2)$  could only operate on two antiparallel spins (otherwise the total weight is 0). Therefore, the total weight of the path becomes,

$$W_{lr}^{\alpha\beta} = \psi_\alpha \psi_\beta \left(\frac{1}{2}\right)^{2m+N/2}, \quad (2.27)$$

under the condition that the spin configuration  $Z_{\alpha,\beta}$  compatible with the valence-bond states  $V_{\alpha,\beta}$  and  $S_r^e |Z_\beta\rangle = S_l^f |Z_\alpha\rangle$ . This weight with constraints are equivalent to the weight in Eq.(2.24). With these basic concepts of PMC algorithm, we are ready to discuss calculation steps in the following section.

### 2.2.2 Steps in PMC method

The PMC algorithm starts with initializing valence-bond states and spin configurations that are compatible with bonds. In 1D  $N$ -site spin chains, it is natural to create a 1D array to label spins from 0 to  $N - 1$ , and assign spin and valence-bond states to them. For 2D spin system, we could linearize labellings by assigning numbers to spins row by row (or column by column) from 0 to  $N - 1$  as well. Therefore, by simply changing initial labellings, 2D simulations could be very similar as 1D chains. For simplicity, we usually set  $V_\alpha = V_\beta$  and  $Z_\alpha = Z_\beta$ , as shown in Fig. 2.4(a).

#### 1. Diagonal updates

The first update is to insert diagonal operators  $C_{ab}(1)$  into the QMC path. The

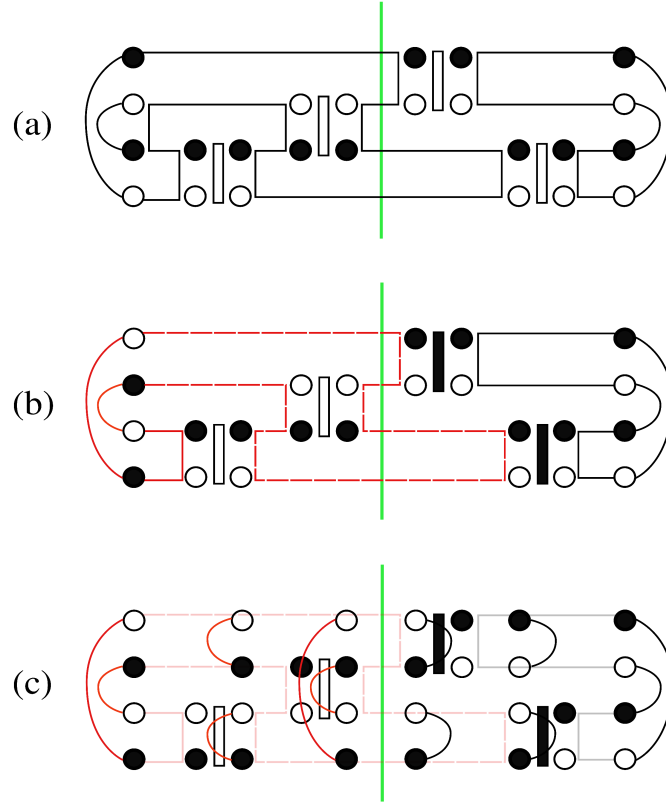


Figure 2.4: An illustration of some key steps in projector Monte Carlo algorithm with the loop update. The open and solid circles represent down and up spins. The open and solid rectangles represent diagonal and off-diagonal operators. Operator strings  $S_l^e$  and  $S_r^f$  operate on states from the left and right ends for  $m$  times, to project the ground state out at around the midpoint of the path. For the demonstration purpose, here we only have  $m = 2$ . (a) We initialize valence bond states and spin configurations at boundaries. We insert diagonal operators on antiparallel spins. We then connect operator vortices to each other and also to the valence-bond states at boundaries to construct loops. (b) We choose loops to flip by probability  $1/2$ . We label flipped loops in red dashed lines and un-flipped loops in black solid lines. The spins at boundaries are updated with corresponding loops. The operators located between two different types of loops switch their types as well — from diagonal to off-diagonal and vice versa. (c) The last step is to treat diagonal and off-diagonal operators as singlet projectors, in order to propagate bonds from two ends to the middle and carry out the observable measurements. We also update spins in the intermediate states according to operator types. We could also update diagonal operators to new legal positions as well, which is not shown in this figure. This is called one MC sweep.

operator can only be located on antiparallel spins as illustrated in Fig. 2.4(a). The spin configuration at each state is the same as initial  $Z_\alpha$  and  $Z_\beta$  for the first step (before other updates take place). Here the operator string is the combination of both strings on the left and right sides, which is written as  $S_{l,r}^{e,f} = (S_l^e)^T S_r^f$ .

## 2. Loop updates

After inserting all diagonal operators, we link all operator vortices, including the VB states at boundaries to form loops. An illustration is shown in Fig. 2.4(a). Each operator vortex has 4 legs and each leg belongs to one loop. After operator locations have been fixed, the loop structure is determined.

When the construction of loops is complete, we then choose loops to flip with probability  $1/2$ . As shown in Fig. 2.4(b), there are two loops formed in this “space-time” configuration. We use red dashed lines to label loops to be flipped. Please note here that, the spins on boundaries which are parts of the flagged loop should be flipped too, as shown in the left boundary of Fig. 2.4(b). This “flipping” also involves the update of operator type: operators that are located between flagged and not-flagged loops should change to the opposite type (diagonal  $\leftrightarrow$  off-diagonal). The reason that we could easily update operators and spins in loops is because the sampling weight  $W_{lr}^{\alpha\beta}$  in Eq.(2.27) only depends on the number of operators, therefore, any loop update will be accepted. This elegant update might not work for anisotropic models. Instead, worm algorithm [70] and directed loop update [71] could be used in QMC to solve anisotropic models. e.g. Heisenberg model with external magnetic field.

## 3. Bond propagation

The next step is to propagate valence bonds according to current operator positions. As we learned from Eq.(2.21) and Fig.2.3, singlet projector projects out singlet pairs. Here we treat  $C_{ab}(1)$  and  $C_{ab}(2)$  operators as singlet projectors, and use them to propagate the valence bond states to the midpoint of the propagation path, as shown in Fig. 2.4(c). The measurement is carried out at or around the midpoint, which we

will discuss more in Sec. 2.2.3. This procedure of switching back to the pure valence-bond basis is equivalent to summing over all spin-z configurations compatible with the bonds of the boundary bra and ket states. We want to point out here that the bond propagation step is not a part of the MC sampling, but for measuring expectation values within each MC sweep.

#### 4. State updates

We also update states on boundaries. This is equivalent to sampling  $W_{\alpha,\beta}^{lr}$  with different valence-bond states  $|V_\alpha\rangle$  and  $|V_\beta\rangle$ . The methods in state updates have already been discussed in Sec.2.1.4.

#### 5. Diagonal update revisit

Now we go back to the diagonal update. After the first MC sweep, we have off-diagonal operators in the loop. Therefore, in the revisited diagonal update, we have two tasks, as demonstrated in Fig. 2.4(c): the first task is to update spins in each propagating states according to the operator type. As spins evolve from state  $|V_\alpha(i)\rangle$  to  $|V_\alpha(i+1)\rangle$ , where  $i \in [1, 2m-1]$ , spins stay the same if there is a diagonal operator and flip signs if there is an off-diagonal operator. The  $Z_\alpha(2m) = Z_\beta(0)$  condition should be satisfied. The second task is to update operators. We could move the diagonal operator to a new allowed position. We could not update the off-diagonal operator freely because this update might bring sign problems to the QMC simulation.

These are procedures in one MC sweep. By using the loop update, we could have more efficient updates, and also, loops guarantee that there will be even number of off-diagonal operators in the simulation, so the negative sign in  $C_{ab}(2)$  in Eq.(2.25) are eliminated in sampling weights. For the detailed implementation in pseudocodes, please refer to the note for the Stochastic Series Expansion (SSE) algorithm in Ref. [21]. Though based on difference ideas, the implementation of SSE is very similar as PMC (the essential difference being in the “time” boundary condition, which is periodic in the SSE but given by the boundary state in PMC).

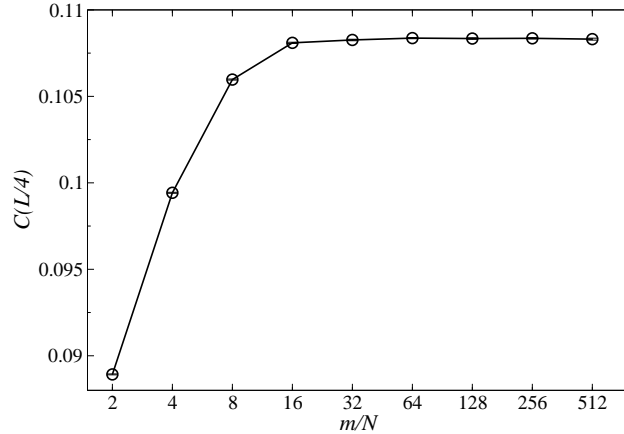


Figure 2.5: The measurement of  $C(\mathbf{r})$  at  $r = (L/4, L/4)$  versus the number of propagation steps for 2D Heisenberg model on a square lattice with edge length  $L = 32$ .  $m$  is the number of propagation steps and  $N$  is the system size. The ratio  $m/N$  is plotted in a logarithmic scale.  $C(L/4, L/4)$  is not converged until  $m/N$  reaches 16.

### 2.2.3 Measurement of observables

Measurements of observables are usually carried out in the midpoint of the propagation path, as marked in the green solid line in Fig. 2.4. After we have propagated the valence-bond states  $m$  times from left and right ends, these two states formed the transition graph in the midpoint of the path, i.e.  $\langle V_\alpha(m) | V_\beta(m) \rangle$ , which is the same as shown in the center of Fig.2.1. Therefore, the measurement of correlation functions are the same as we have discussed in Sec.2.1.3.

In practice, the observables could not only be measured at the midpoint of the propagation, but also a few points around it to have a better statistical performance, provided that the  $m$  is sufficiently large to project out the ground state when measurements take place. In Figure 2.5, the importance of having large  $m$  is demonstrated. We measure the spin-spin correlation function  $C(\mathbf{r})$  at  $r = (L/4, L/4)$  for the 2D Heisenberg model on a square lattice, where  $L$  is the edge length of the square. From the data in Fig. 2.5, we could conclude that correlation values do not converge until  $m/N \sim L$ . Therefore, since  $m \propto L^3$ , PMC takes a long time to reach the ground state for large systems. The calculation should

still be faster than using SSE, or other  $T > 0$  methods, to reach the limit  $T = 0$ .

#### 2.2.4 Generalization to $J - Q_3$ model

The PMC algorithm is easy to extend from Heisenberg model to other non-frustrated isotropic models. In this section, we will discuss the implementation of PMC on  $J - Q_3$  model as an example.

The  $J - Q_3$  model is written as,

$$H = -J \sum_{\langle ij \rangle} C_{ij} - Q_3 \sum_{\langle ijklmn \rangle} C_{ij} C_{kl} C_{mn}, \quad (2.28)$$

where  $J$  term is the Heisenberg interaction and  $Q_3$  term is the interaction of three nearest lined-up singlet operators. We will study  $J - Q_3$  model carefully in Chapter 3. Here we only focus on the numerical implementation of it.

The Heisenberg model only has one group of singlet operators. With the  $J - Q_3$  model, systems now have two groups of operators: the value of the diagonal part of the  $J$  operator is  $W_J = J/2$  and of the  $Q$  operator is  $W_Q = Q/8$ . In the step of diagonal update, we should accept and reject diagonal operator insertion by considering different weight ratios:

- If  $J$  operator is proposed,  $P_{accept} = \min[\frac{W_J}{W_Q}, random]$ ;
- If  $Q$  operator is proposed,  $P_{accept} = \min[\frac{W_Q}{W_J}, random]$ .

*random* is any number randomly generated from  $[0, 1]$ .

For loop updates, here we have  $Q_3$  operator, which has three operator vortices and 12 legs in total. With the consideration of all extra vortices and legs, we could still construct loops similarly as for Heisenberg model, as illustrated in Fig.2.6. Please note that since the  $Q_3$  term has three singlet projectors, there are in total 8 combinations of diagonal and off-diagonal operators ( $2 \times 2 \times 2$ ), which are sampled by loop updates. Each operator in  $Q_3$  is updated independently from the other two. Though this may look complicated, the *bit* operation provides a concise way to record the information of operators. For example, for a spin chain with size 8 as shown in Fig.2.6, we use 4 bits to denote  $J$  and  $Q$  operators.

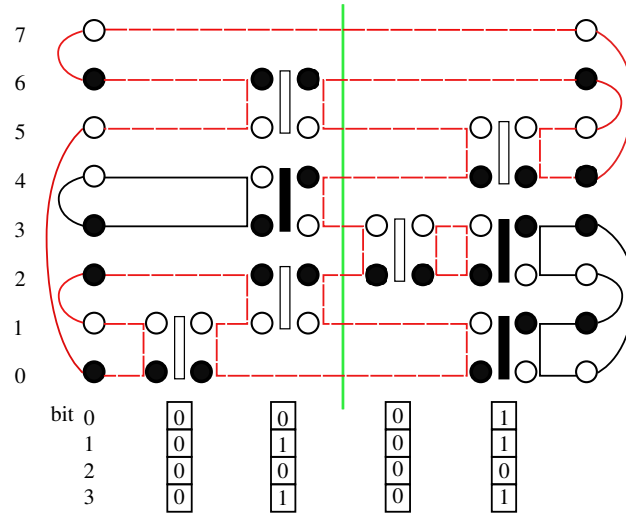


Figure 2.6: An illustration of loop updates in PMC for the  $J - Q_3$  model on a 8-size spin chain. Similarly as the Heisenberg model in Fig.2.4, we connect all operator vortices together with valence-bond states on boundaries to form closed loops. Since the  $Q_3$  term has 3 singlet operator vortices, it has 12 legs. Each operator could be updated independently from the other two, in order to sample 8 combinations of diagonal (open rectangle) and off-diagonal (solid rectangle) operators. We use *bits* to record the operator information, as listed in the bottom of the figure. The first three bits correspond to the type of operators, 0 for diagonal and 1 for off-diagonal. The last bit distinguishes the operator group, 0 for  $J$  term and 1 for  $Q$  term.

On the 4<sup>th</sup> bit, 0 denotes the  $J$  operator and 1 denotes  $Q$  operators. The first three bits denote the type of operators, 0 denotes diagonal and 1 off-diagonal. Therefore, for the  $Q$  operator on the second states from the left, which has “diagonal — off-diagonal — diagonal” combination, we could use the 4-bit 0101, which is of the value 10 to record the operator information on this state. For the  $J$  operator, the second to fourth bits will always to zero, with only the first bit to label the operator type. The other bits are used for the lattice location of the operator.

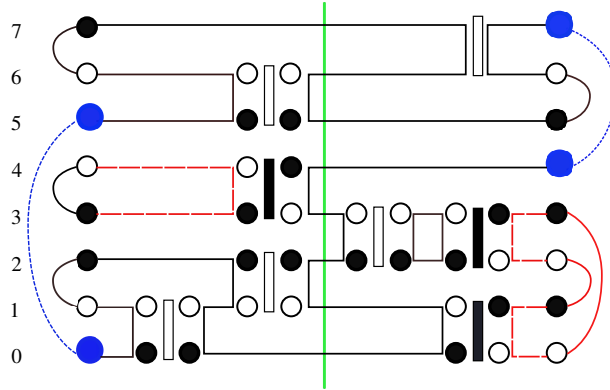


Figure 2.7: An illustration of PMC simulations for triplet states. We sample valence-bond states with two  $S = 1/2$  spinons (bigger blue solid circles) in the system. In the PMC simulation, we treat the triplet (blue dashed line) as singlet. The only difference from the ground state ( $S = 0$ ) simulation is that we never flip the loop containing spinons.

### 2.2.5 Application to spinon characterization

Since in this thesis we focus much on studies of spinons in  $J - Q_3$  model, we here also briefly discuss the simulation of systems with triplet states.

As we present in Sec.1.3, spinons are emergent fractional particles carrying spin  $1/2$ . For states with spinons, as shown in Fig.2.7, we have two unpaired spins connected via a triplet bond (blue dashed line in figure), and all other spins form singlet pairs. In the construction of loops, we treat the triplet the same as singlet in PMC, besides the fact that we never flip loops with spinons in. Therefore, it is a very simple generalization of ground state ( $S = 0$ ) simulations. We also want to address here that, states stay in the  $S = 1$  sector as two spinons never annihilate in our simulations. All spinon statistical measurements are implemented in the midpoint of the propagation path, where states with the lowest energy of the *first excited states* have been obtained. Results will be discussed in detail in Chapter.3.

## 2.3 Renyi entanglement entropy measurement

We have introduced the entanglement entropy in Sec. 1.5. As entanglement entropy has played a more and more important role in condensed matter physics, the recent development in QMC [50] of measuring the second order Renyi entropy  $S_2$  [Eq.(1.6)] has brought a significant progress in computational physics. In this thesis, we also use this recent technique to measure  $S_2$  of amplitude product states. (Results are presented in Sec.5.3.)

As already discussed in Sec. 1.5, entanglement entropy is a quantitative measurement of how much two regions are entangled. We divide our systems into region A and region B. The state of the whole system could be written as  $|\Phi\rangle = \Psi_{A,B}|V_A\rangle|V_B\rangle$ , where  $|V_A\rangle$  and  $|V_B\rangle$  are complete basis of region A and B,  $\Psi_{AB}$  are coefficients. In order to measure  $S_2$ , we need two independent copies of the system. We define an operator  $Swap$  written as  $\hat{O}_{Swap}$  to measure the Renyi entropy. Swap operator will exchange valence-bond states between copy-I and copy-II in the swapped region A as shown in Fig. 2.8(a) and (b). The expression is written as,

$$\begin{aligned} \hat{O}_{Swap} & \left( \sum_{A_1, B_1} C_{A_1, B_1} |V_{A_1}\rangle |V_{B_1}\rangle \right) \otimes \left( \sum_{A_2, B_2} C_{A_2, B_2} |V_{A_2}\rangle |V_{B_2}\rangle \right) \\ & = \sum_{A_1, B_1} C_{A_1, B_1} \sum_{A_2, B_2} C_{A_2, B_2} (|V_{A_2}\rangle |V_{B_1}\rangle) \otimes (|V_{A_1}\rangle |V_{B_2}\rangle) \end{aligned} \quad (2.29)$$

We could write the state of two independent copies as  $|\Phi_{A,B}^{1,2}\rangle = \sum_{A_1, B_1} C_{A_1, B_1} |V_{A_1}\rangle |V_{B_1}\rangle \otimes (\sum_{A_2, B_2} C_{A_2, B_2} |V_{A_2}\rangle |V_{B_2}\rangle)$ , therefore, the evaluation of operator  $\hat{O}_{Swap}$  is,

$$\begin{aligned} \langle \Phi_{A,B} | \hat{O}_{Swap} | \Phi_{A,B} \rangle & = \sum_{A_1, B_1, A_2, B_2} C_{A_1, B_1} C_{A_2, B_2} C_{A_2, B_1} C_{A_1, B_2} \\ & = \sum_{A_1, A_2} (\rho_A)_{A_1, A_2} (\rho_A)_{A_2, A_1} = Tr(\rho_A^2). \end{aligned} \quad (2.30)$$

Therefore, the second Renyi entropy is the same as  $-\ln(\langle \hat{O}_{Swap} \rangle)$ .

In practice, the importance sampling of  $\langle O_{Swap} \rangle$  is not well distributed. Especially for large systems, the measurement of  $\langle S_2 \rangle$  could be too noisy to provide any information.

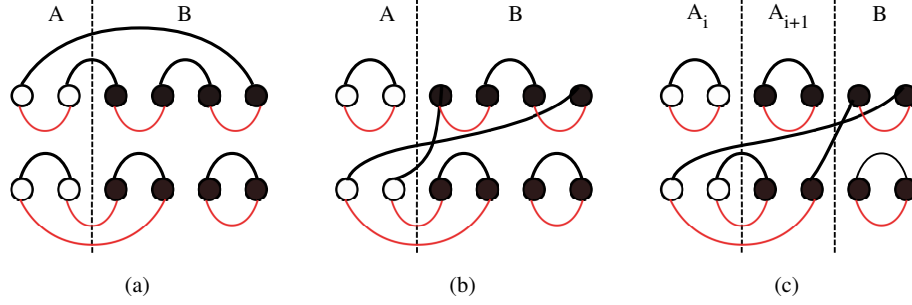


Figure 2.8: We use a 6-site spin chain to illustrate the swap operator and improved ratio trick. In (a), we have two copies of the system (upper and lower), with different VB state configurations. The red (lower) VB states are for reference and swap operator acts on black (upper) VB states. In (b), as we divide the system into two regions, A and B, the swap operator exchanges all VB state connections in region A between two copies. (c) illustrates that with first region swapped, the ratio measurement only operates on the region difference  $A_{i+1} - A_i$ . As we discussed in the text, this ratio trick will improve the statistical performance significantly.

In order to improve the statistical performance, Ref. [50] proposed the “improved ratio” sampling, which samples weights of the pre-swapped region  $A_i$  and measure the swap evaluation in the non-overlapped region between  $A_i$  and  $A_{i+1}$ , as illustrated in Fig. 2.8(b) and (c). This ratio is expressed as,

$$\frac{\langle O_{Swap}^{A_{i+1}} \rangle}{\langle O_{Swap}^{A_i} \rangle} = \frac{\sum_{\alpha, \beta} W_\alpha W_\beta \langle V_\alpha | O_{Swap}^{A_{i+1}} | V_\beta \rangle}{\sum_{\alpha, \beta} W_\alpha W_\beta \langle V_\alpha | O_{Swap}^{A_i} | V_\beta \rangle}. \quad (2.31)$$

Since the Renyi entropy uses the logarithm of the expectation value of the swap, the quantity  $S_2(A_{i+1})$  could be simply written as the summation of all logarithms of previous ratios, such as,

$$S_2(A_{i+1}) = -\ln\left(\frac{\langle O_{Swap}^{A_{i+1}} \rangle}{\langle O_{Swap}^{A_i} \rangle}\right) - \ln\left(\frac{\langle O_{Swap}^{A_i} \rangle}{\langle O_{Swap}^{A_{i-1}} \rangle}\right) - \dots - \ln\left(\frac{\langle O_{Swap}^{A_2} \rangle}{\langle O_{Swap}^{A_1} \rangle}\right). \quad (2.32)$$

We demonstrate the measurement of *second* Renyi entropy here. By having more duplicates of the system, we could compute any higher order of Renyi Entropy as depicted in Eq.(1.6).

## Chapter 3

# Characterizing Spinons as Emergent Elementary Particles

### 3.1 Introduction

In one-dimensional (1D) strongly correlated systems, the emergence of fractional quantum numbers is a generic consequence of collective behaviors. In the exactly solvable critical  $S = 1/2$  antiferromagnetic (AFM) spin chain, the fundamental excitations are soliton-like quasiparticles (kinks and anti-kinks) called *spinons* and carrying spin  $1/2$  [72, 73]. Similar objects exist also in the valence-bond-solid (VBS) state stabilized by frustrated interactions [74]. In higher dimensions, in systems with long-range AFM order, the fundamental excitations are magnons with spin 1, as explained successfully by spin-wave theory [75]. A bound state of spinons (forming magnons) can be induced in the Heisenberg chain by an external magnetic field [76]. In 2D systems, deconfined spinons should emerge when a transition into a VBS state is approached, according to the theory of “deconfined” quantum-critical points [28, 29].

The search for spinons has been a quest in experimental and theoretical condensed matter physics for decades, primarily because the fractionalization of excitations is a characteristic of exotic collective quantum many-body states—spin liquids [77]. Moreover, in some cases the mechanism of confinement of spinons is a condensed-matter analogue of the confinement of quarks in quantum chromodynamics. In this chapter, building on a previous

brief presentation [78], we will explore systems where confinement and deconfinement of spinons can be detected and characterized using large-scale quantum Monte Carlo (QMC) simulations in the valence-bond (VB) basis. We here focus on a range of different 1D systems but note that the same ideas have also already been applied to 2D systems in the context of deconfined quantum-criticality [39].

The starting point of our studies is the  $S = 1/2$  AFM Heisenberg chain, defined by the Hamiltonian

$$H = J \sum_{i=1}^N \mathbf{S}_i \cdot \mathbf{S}_{i+1}, \quad (3.1)$$

where the nearest-neighbor coupling  $J > 0$ ,  $N$  is the total number of spins, and we apply periodic boundary conditions. We will add other interactions to this model later, in order to bring the system to the different types of ground states mentioned above.

The ground state of the plain Heisenberg model (3.1) can in principle be solved exactly by the Bethe-Ansatz approach [79], but in practice many of its salient features, such as the power-law decaying spin-spin correlations, were found using the bosonization method [80]. Reflecting the deconfined spinons, the lowest excited states of the Heisenberg model form bands of degenerate singlets and triplets [76,81,82] with the energy  $\epsilon_1(q)$  as a function of the total momentum  $q$  of the state being  $\epsilon_1(q) = (\pi/2)J|\sin(q)|$ , which was first calculated by des Cloiseaux and Pearson using the Bethe Ansatz [81]. Forming all possible combinations of two spinons propagating independently with fixed momenta,  $\tilde{q}_1$  and  $\tilde{q}_2$  with  $q = \tilde{q}_1 + \tilde{q}_2$  gives a continuum above the lower bound and an upper bound given by  $\epsilon_2(q) = \pi J|\sin(q/2)|$ . A large spectral weight between these bounds (concentrated close to the lower bound because of matrix elements) in inelastic neutron scattering is considered as an indicator of the existence of spinons in one dimension.

The continuum spectrum of spinons has been observed in weakly-coupled-chain compounds such as copper pyrazine dinitrate and  $\text{KCuF}_3$  at zero magnetic field [83,84], while in none-zero magnetic fields incommensurate modes have been observed [83,85]. In another chain compound,  $\text{CuCl}\cdot 2(\text{dimethylsulfoxide})$ , there is an effective internal staggered magnetic field present, and spinon bound states have been observed [86]. In addition, in the

spin ladder system  $(\text{C}_5\text{H}_{12}\text{N})_2\text{CuBr}_4$ , it was reported that the magnon could be fractionalized into spinons by tuning the external magnetic field [87]. The above experimental results can be modeled using the Heisenberg Hamiltonian (3.1) including the other effects mentioned above (fields, inter-chain couplings). In addition to neutron scattering, other experimental signals of spinons have also been proposed [88]. So far, however, all the experimental probes give indirect information on the existence of spinons, and not much information on the properties of spinons other than their dispersion.

Motivated by the on-going exciting research in the quantum physics of fractionalization, in this chapter we are interested in exploring other aspects of spinons and their confinement-deconfinement transitions. Using the QMC approach introduced in Ref. [45] and used in Ref. [39] to study 2D systems, we here explore a wider range of low-dimensional systems where confinement and deconfinement can be studied systematically under various conditions. The method operates in a basis of VBs (two-spin singlets) and unpaired spins and allows us to compute quantities defining the size of an isolated spinon as well as the size of an  $S = 1$  bound state. We also show that the same length scales appear in standard spin correlation functions, but are harder to access there in practice because the signal only appears in the differences between correlations in different spin sectors (and is therefore very noisy in QMC calculations of large systems).

The structure of the rest of the chapter is as follows: In Sec 3.2 we introduce the projector QMC method and calculated observables used to characterize spinons. In Sec 3.3 we present results for the  $J$ - $Q$  chain model [45, 69], which undergoes a quantum phase transition from the Heisenberg critical phase to a spontaneously symmetry-broken valence-bond solid (VBS). This system has deconfined spinon excitation in the entire range of the ratio  $Q/J$  of the Heisenberg exchange  $J$  and a multi-spin coupling  $Q$ . To achieve confinement, in Sec. 3.4 we introduce a staggered pattern of  $J$ -interactions, as recently done also in an investigation of spinon binding to a static impurity [89]. In Sec. 3.5 we study spinon confinement when two Heisenberg chains are coupled to form a ladder. In Sec. 3.6 we discuss the fact that the same length-scales appearing in our VB-based definition of

spinons can also be identified in the fine-structure of the spin-spin correlations in the higher-spin states, thus confirming that these length-scales are not basis dependent and can be investigated using other methods as well. We summarize our work in 1D and discuss future prospects in Sec. 3.7. We also study properties of the DQC spinons and their near-DQC bound states in the 2D spin systems. In Sec.3.9, we demonstrate that a naive picture of a large bound state of two small objects fails—the spinons themselves are of size comparable to the bound state and are “soft”, shrinking when forming bound states. This differs from the prototypical short-bond resonating valence-bond (RVB) spin liquid [5, 62], which we also study as a point of reference in Sec.3.8. Here the deconfined spinons are small, with radius of a few lattice spacings. We conclude the confinement and deconfinement of spinons in 2D in Sec. 3.11.

## 3.2 Methods and calculated observables

We use valence-bond projector QMC (VBPQMC) algorithm, which has been described in detail in Chapter.2.2. Here we focus on the definitions of spinon quantities and how to evaluate them.

### 3.2.1 Generalized VB basis for $S > 0$

In addition to the use of the VB basis for singlet ground states, extensions of the VB basis with unpaired spins also provide a natural and convenient way to describe excitations with higher spin [68,69]. In our study of spinons, we will study systems with one or two unpaired spins. In the former case, the total number of sites  $N$  is odd, and a generalized VB state can be written as

$$|V_\alpha(r)\rangle = \left[ \bigotimes_{i=1}^{(N-1)/2} |a, b\rangle_{\alpha, i} \right] \otimes |\uparrow_r\rangle, \quad (3.2)$$

where the notation explicitly indicates the location  $r$  in the chain of the unpaired spin and  $\alpha$  labels the possible  $(N - 1)/2$ -bond configurations with this site excluded. For system

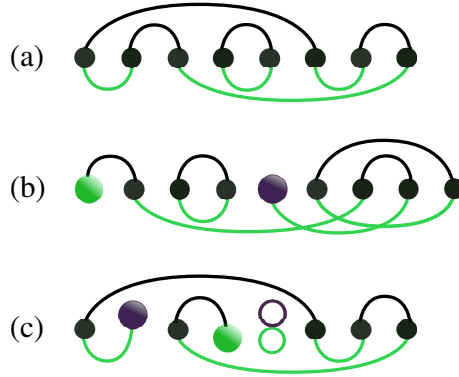


Figure 3.1: Transition graph formed by bra (upper, black) and ket (lower, green) valence bond states on a spin chain. Part (a) shows an  $S = 0$  state on an even number of sites. In (b) the number of sites is odd and there is an unpaired spin in both the bra and the ket state. Part (c) shows an  $S = 1$  configuration, where there are two unpaired spins. In VBPQMC simulations, the distance distribution of the unpaired spins in (b) gives information on the size of an individual spinon, while the size of an  $S = 1$  bound state of two spinons is reflected in the distance distribution of unpaired spins on different sublattices in (c).

with even  $N$  and two unpaired spins, analogously an extended VB basis state is written as

$$|V_\alpha(r_a, r_b)\rangle = \left[ \bigotimes_{i=1}^{N/2-1} |a, b\rangle_{\alpha, i} \right] \otimes |\uparrow_{r_a}\rangle \otimes |\uparrow_{r_b}\rangle, \quad (3.3)$$

with  $N/2 - 1$  singlet pairs and two unpaired spins on different sublattices. These extended VB bases are also overcomplete and non-orthogonal in their respective total-spin sectors  $S$ , and, if we choose (as we do here) the unpaired spins to have  $S_i^z = 1/2$ , the  $z$ -projection of the total spin is  $S^z = S$ .

The transition graphs shown in Figs. 3.1(b,c) have open strings [with an open string of length 0 being a special case corresponding to a bra and ket spinon on the same site, an example of which is seen in case (c)] in addition to loops. If we fix the states of the unpaired spins, as we do here, the strings do not contribute and the overlap of two states is still given by Eq. (2.6). Note, in particular, that the unpaired spins can be at different locations and the states still always have non-zero overlap.

### 3.2.2 Characterization of spinons in the VB basis

In order to study spinon sizes and confinement lengths, we compute overlaps written in the form

$$\frac{1}{2}\langle\Psi_0|\Psi_0\rangle_{\frac{1}{2}} = \sum_{r,r'} \sum_{\alpha,\beta} g_\alpha(r)g_\beta(r')\langle V_\alpha(r)|V_\beta(r')\rangle, \quad (3.4)$$

which is using sums of terms with all possible locations of the unpaired spins and all possible VB states. We have an analogous form

$$\begin{aligned} {}_1\langle\Psi_0|\Psi_0\rangle_1 &= \sum_{r_a,r_b} \sum_{r'_a,r'_b} \sum_{\alpha,\beta} g_\alpha(r_a,r_b)g_\beta(r'_a,r'_b) \\ &\langle V_\alpha(r_a,r_b)|V_\beta(r'_a,r'_b)\rangle, \end{aligned} \quad (3.5)$$

for  $S = 1$  (spinon-pair) systems.

As discussed above, in the VBPQMC method the bra and ket states are generated stochastically, and for  $S = 1/2$  we can use Eq. (3.4) to define a distribution of the separation of the unpaired spins in the bra and ket states. Restricting ourselves to a translationally invariant system we have the probability of separation  $r - r'$  (up to an irrelevant normalization factor):

$$P_{AA}(r - r') = \sum_{\alpha,\beta} g_\alpha(r)g_\beta(r')\langle V_\alpha(r)|V_\beta(r')\rangle, \quad (3.6)$$

where the subscript  $AA$  serves to indicate that the unpaired spins should be on the same sublattice, which we can take as the  $A$  sublattice. Thus,  $P_{AA}(r)$  should vanish when the separation  $r$  is an odd number of lattice spacings. Our basic assertion is that, if spinons are well-defined quasiparticles of the system, then we expect  $P_{AA}$  to reflect the size and shape of an *intrinsic* “wave packet” within which the net magnetization  $S^z = 1/2$  carried by the spinon is concentrated. We will show below that 1D VBS states are characterized by an exponentially decaying overlap,  $P_{AA}(r) \propto e^{-r/\lambda}$ , and it is then natural to take  $\lambda$  as a definition of the intrinsic spinon size.

We should note here that, for a periodic system with an odd number of sites, there are, strictly speaking, no absolute distinction between the sublattices. However, when the system size  $N \rightarrow \infty$  we in general expect the role of the boundary conditions to diminish

and  $P_{AA}(r)$  to tend to zero for any given odd  $r$ . In Sec. we will discuss in detail how this limit is approached, and we will also see an example (one where spinons are not well-defined quasi-particles) where the boundaries continue to play a role even for infinite size.

In the case of  $S = 1$  states (two spinons), we can define several different distributions. Here we will focus on the separation of spinons on *different* sublattices in the bra and ket;

$$P_{AB}(r_a - r'_b) = \sum_{\alpha, \beta} \sum_{r_b, r'_a} g_{\alpha}(r_a, r_b) g_{\beta}(r'_a, r'_b) \times \langle V_{\alpha}(r_a, r_b) | V_{\beta}(r'_a, r'_b) \rangle. \quad (3.7)$$

In the case where a single spinon is a well-defined quasi-particle, i.e.,  $\lambda < \infty$ , we expect this quantity to give us information on the confinement or deconfinement of two spinons. In the former case, we will see that asymptotically  $P_{AB}(r) \propto e^{-r/\Lambda}$  and, thus, we consider  $\Lambda$  as a definition of the confinement length-scale (i.e., the size of the  $S = 1$  spinon bound state). We could also have defined this quantity with the two unpaired spins both in the bra or in the ket, and we have also investigated it. This distribution typically does not differ significantly from the one defined in Eq. (3.7).

We will also study the analogue of the  $S = 1/2$  quantity  $P_{AA}(r)$ , Eq. (3.6), in the triplet state, defined as

$$P_{AA}^*(r_a - r'_a) = \sum_{\alpha, \beta} \sum_{r_b, r'_b} g_{\alpha}(r_a, r_b) g_{\beta}(r'_a, r'_b) \times \langle V_{\alpha}(r_a, r_b) | V_{\beta}(r'_a, r'_b) \rangle, \quad (3.8)$$

where we use the \* superscript to distinguish this distribution from the single-spinon distribution (3.6). We can define  $P_{BB}^*$  in the same way, and use  $P_{AA}^*(r) = P_{BB}^*(r)$  to improve the statistics. We will see that, under certain conditions,  $P_{AA}^*$  of the triplet state contains the same information for the spinon size  $\lambda$  as the  $S = 1/2$  quantity  $P_{AA}$ , and we can use this property of the  $S = 1$  state to characterize the intrinsic spinon size also in cases where the  $S = 1/2$  state breaks translational invariance and is not appropriate for use with our calculations presuming translational invariance (the 2-leg ladder system being such an example, which will be studied below in Sec. 3.5).

The practical simulation procedures for  $S > 0$  are relatively straight-forward generalizations of the method with loop updates for  $S = 0$ . We refer to Refs. [45, 68, 69] for technical details.

Since our calculation projects out the lowest state with given total spin, in the case of  $S = 1$  the total momentum  $k$  is  $k = \pi$  (since this is the momentum of the lowest triplet in a bipartite chain). Therefore the spinons here are not propagating, having individual spin 0 and  $\pi$  (these giving the lowest possible energies in light of the des Clauseaux-Pearson dispersion). For the  $S = 1/2$  state the lowest state has  $k = 0$ . In principle our calculations can also handle total momentum away from  $k = 0, \pi$ , but in practice, due to phase problems in the Monte Carlo sampling, we are restricted to momenta close to 0 and  $\pi$ . We here only consider the lowest state projected out without adding any phases.

### 3.3 Deconfined spinons in uniform spin chains

We here first test the concepts and methods for a class of spin chains, the  $J-Q_3$  model, which can be tuned between a ground-state phase with properties similar to the standard critical Heisenberg chain and a VBS phase with VBs crystallizing on alternating nearest-neighbor bonds. In the critical state, spinons are rigorously known to be elementary excitations based on the exact Bethe-Ansatz wave function of the plain Heisenberg chain, and in a VBS state there are also strong arguments for spinons [74]. In either case, a pair of spinons can be regarded as a kink and an anti-kink of an ordered (in the case of the VBS) or quasi-ordered (in the critical state) medium. There is no apparent confining potential between these defects in one dimension (and clearly any effectively attractive potential would lead to a bound state and confinement of the spinons). Our calculations show explicitly that there are instead weak *repulsive* interactions, which diminishing with the system size, leading to independently propagating spinons in the thermodynamic limit.

### 3.3.1 Results for the $J$ - $Q_3$ chain

We here consider the 1D  $J$ - $Q_3$  Hamiltonian,

$$H = - \sum_i^N (JC_{i,i+1} + Q_3 C_{i,i+1} C_{i+2,i+3} C_{i+4,i+5}), \quad (3.9)$$

where  $C_{ij}$  is a singlet-projection operator on two sites,

$$C_{i,j} = 1/4 - \mathbf{S}_i \cdot \mathbf{S}_j, \quad (3.10)$$

and the  $J$  term is simply the standard antiferromagnetic Heisenberg interaction. We here use the  $Q_3$  term with three projectors, as its ground state at the extreme point  $J = 0$  is more strongly VBS-ordered than that of the  $Q_2$  model with only two projectors.

When the coupling ratio  $g = Q_3/J$  is small, the system remains in the Heisenberg-like critical state, where the spin-spin correlation function  $C(r)$ , the expectation value of Eq. (5.2), has the asymptotic form  $C(r) \sim \ln^{1/2}(r)/r$  [80, 90, 91]. When  $g$  is large, the  $Q_3$  term enforces VBS ordering and  $C(r)$  is exponentially decaying. The VBS state is two-fold degenerate. The physics of this phase transition is identical (in the sense of universality) [78, 92] to that in the frustrated  $J_1$ - $J_2$  chain, where spinons in the VBS state were discussed on the basis of a variational state by Shastry and Sutherland [74]. In field-theory language, the phase transition is driven by the sign-change of a marginal operator, and this operator is also the root cause of the logarithmic correction to  $C(r)$  in the critical phase. Exactly at the critical-VBS transition point the correlations decay as  $1/r$  with only very small corrections. The transition point of the  $J$ - $Q_3$  model is at  $g_c = (Q_3/J)_c \approx 0.1645$ , as determined from level spectroscopy [93] (excited-state singlet-triplet crossing) [78] and VBPQMC calculations of correlation functions [92].

#### 3.3.1.1 Single spinons in states with total-spin 1/2

We here first investigate  $P_{AA}(r)$  as defined in Eq. (3.6) to study the size of spinons in the VBS phase at different coupling ratios  $g$ . In Fig. 3.2(a) we see that the intrinsic spinon wave packet has a pronounced exponential decaying form,  $P_{AA}(r) \propto e^{-r/\lambda}$ , showing that spinons

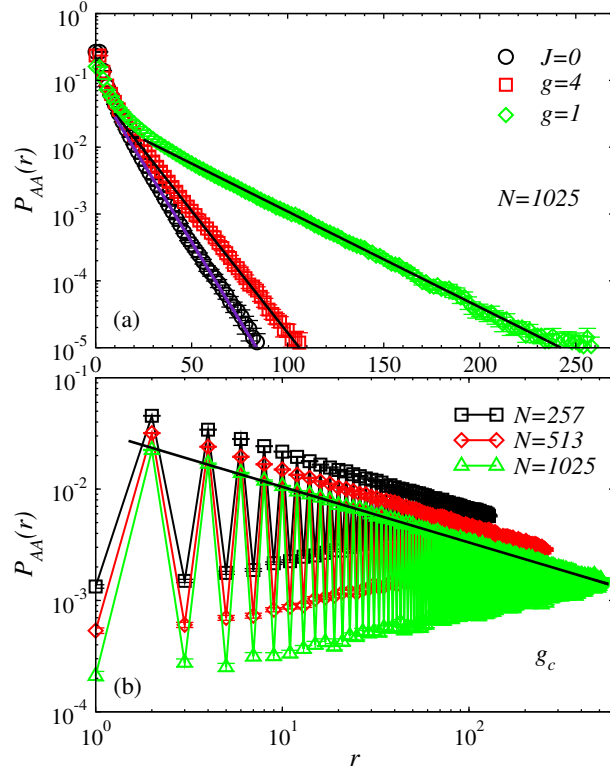


Figure 3.2: Single spinon overlap distribution in the  $J - Q_3$  chain. (a) Exponential decays indicating well-defined quasi-particles in VBS states at different values of  $g = Q_3/J$ . The size  $\lambda$  of the spinon (the inverse of the slopes of the lines on the lin-log plot) diverges as the critical point is approached. Panel (b) shows that spinon is marginally defined at the critical point, with the overlap decaying as a power-law with exponent  $\alpha = 0.500(2)$ . The even-odd oscillations are due to the frustration caused by the single-spinon defect in a periodic chain (with the odd- $r$  contributions only possible in a bipartite system). The effects of frustration diminish as the chain size increases.

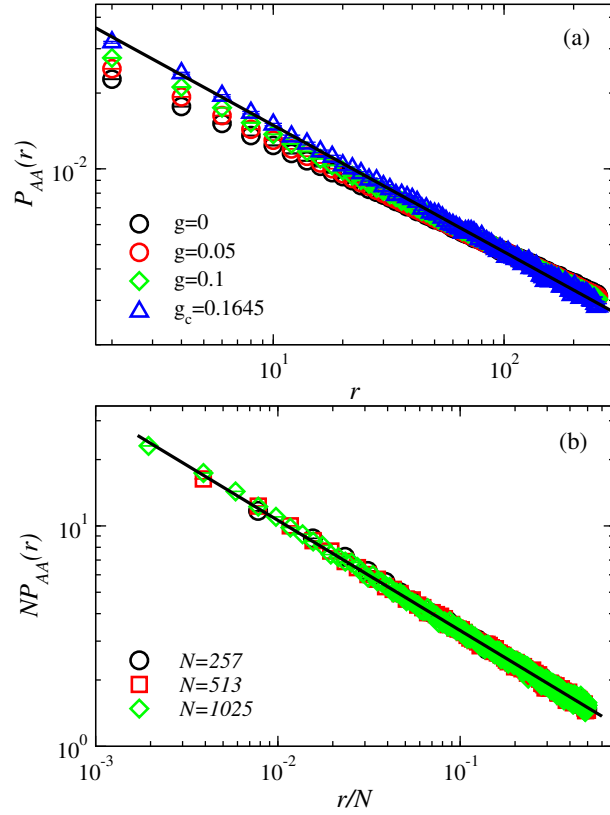


Figure 3.3: (a) Single-spin distribution function at the VBS transition point and inside the critical phase. (b) The data at  $g_c$  rescaled such that data collapse is achieved. The lines correspond to the  $r^{-1/2}$  form.

indeed are well defined quasi-particles of the VBS, with a characteristic size  $\lambda$ . The spinon size decreases with increasing  $g$  (going deeper into the VBS phase), with  $\lambda = 30.0(1)$  when  $g = 1$  and  $\lambda = 9.2(1)$  when  $g \rightarrow \infty$  (the pure  $Q_3$  model). As shown in Fig. 3.2(b), exactly at the transition point the decaying form is no longer exponential, instead it is very well described by  $r^{-\alpha}$  with the power  $\alpha = 0.500(2)$ . Thus, the spinon here can be considered only as marginally well-defined quasi-particle in real space.

It should be pointed out that, in periodic chains of odd size  $N$ , which we use here to study an unpaired spin, there is magnetic frustration caused by the boundary condition and the lattice is no longer strictly bipartite. Thus, maintaining the updating rules in the simulations [64, 92] the VB singlets here can some times be formed between sites on the

same sublattices if we continue to label the sites as alternating A and B, except for one instance of adjacent AA or BB sites (in the simulation we do not explicitly label the sites and there is no breaking of translational symmetry as we just use the same updating rules for the bonds and unpaired spins as for the even- $N$  chains). The distance between the unpaired spin in the bra and ket can then be an odd number of lattice spacings (while it is always even in a true bipartite chain). The probability of these odd distances is exceedingly small in the VBS state of the  $N = 1025$  chains used in Fig. 3.2(a), but in the critical-chain results in Fig. 3.2(b) we clearly can see non-zero odd- $r$  probabilities. Relative to the even- $r$  probabilities, for fixed  $r$  they decrease rapidly as  $N$  grows, while approaching the even- $r$  probabilities as  $r \rightarrow N/2$  (and, interestingly, the odd branch follows the same power-law as the even one but with different sign). In our simulations we neglect the non-trivial (non-Marshall) signs in the wave function arising from the even-length bonds (where we define the length as the shortest of the two possible distances between the two paired spins under the periodic boundary conditions), but we find it unlikely that this approximation would affect our conclusions on the nature of the spinon as these signs also are due to boundaries and we are interested in the thermodynamic limit. We will also see further below that we see the same exponential (for  $g < g_c$ ) power-law (for  $g = g_c$ ) decay also in  $P_{AA}^*$ , Eq. 3.8, in the chains with two unpaired spins, where the lattice remains bipartite and there are no frustration effects.

Given the fact that the exponent  $\alpha$  of the critical spinon overlap in Fig. 3.2(b) is very close to  $1/2$ , and the behavior is seen to remarkable consistency over two orders of magnitude of  $r$ , we conjecture that the exponent should in fact be exactly  $1/2$ . It is tempting to associate it with the square-root of the spin correlation function  $C(r) = 1/r$ , although we have not tried to formally compute this quantity within the bosonization approach (which in principle should be applicable [94]).

Another interesting question to ask is, how is the critical  $\sim r^{-1/2}$  form of the single-spinon distribution  $P_{AA}(r)$  at  $g_c$  changed when going further into the critical region ( $g < g_c$ ). The logarithmic correction to the correlation function  $1/r$  is a well known consequence of

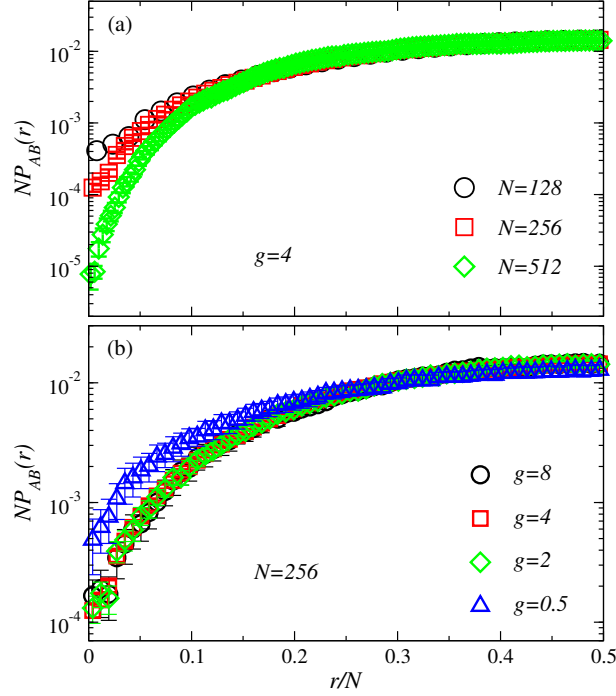


Figure 3.4: Two-spinon distance distribution in VBS states of the  $J$ - $Q_3$  chain at (a) fixed  $g = 4$  and different chain lengths, (b) fixed chain length  $N = 256$  and different coupling ratios. The  $x$ - and  $y$ -axis has been rescaled with  $N$  and  $1/N$ , respectively, in order to achieve data collapse in (a). The distributions in (b) show that the effective spinon-spinon repulsion becomes weaker as system approaches the transition point ( $g_c = 0.1645$ ).

the presence of a marginal operator, as mentioned above. One would then expect corrections to  $P_{AA}(r)$  as well. As seen in Fig. 3.3(a),  $P_{AA}(r)$  indeed changes noticeably when moving away from the transition point into the  $g < g_c$  critical phase. The behavior can be fitted to a power-law with exponent depending on  $g$ , but most likely the  $r^{-1/2}$  behavior persists for all  $0 \leq g \leq g_c$  and it is only the strength of a logarithmic correction that changes. While the data can be fitted to the  $r^{-1/2}$  with a multiplicative logarithmic correction, the power of the logarithm is not clear, and to further study this behavior quantitatively would require much longer chains. In Fig. 3.3(b), we further analyze the behavior at  $g_c$  for different system sizes, re-graphing the data in Fig. 3.2 such that data collapse is achieved. An interesting aspect of these results is that there are no noticeable enhancements due to the periodic boundaries at the longest distances,  $r \sim N/2$ , with the power-law describing the data very well from the smallest to largest distances for all system sizes.

### 3.3.1.2 Two spinons in states with total-spin 1

Next, we consider chains with even  $N$  and two unpaired spins. The distribution function  $P_{AB}(r)$  here reflects the effective mutual interaction between two spinons, mediated by the background of singlets. For a confining case, we would expect to observe  $P_{AB}(r) \propto e^{-r/\Lambda}$ , with a finite confinement length  $\Lambda$ . Deconfinement should be signalled by a divergence of  $\Lambda$ . Results for the  $J$ - $Q_3$  chain in the VBS phase, graphed in Fig. 3.4, show distribution functions with no decay at long distances. Instead  $P_{AB}(r)$  exhibits a very broad maximum at the largest distance, which we naturally interpret as resulting from a weak repulsion between two spinons. As shown in Fig. 3.4(a), the repulsion diminishes somewhat when tuning down the coupling ratio toward the critical point, where, apparently, increasing quantum fluctuations (including an increasing fraction of long VBs) reduce the repulsive potential. The range of  $r$  over which the distribution is almost flat increases essentially proportionally with  $N$ . In Fig. 3.4(a) we have multiplied the distribution function with  $N$  for several  $N$  at a fixed  $g$  inside the VBS phase, and find that the curves collapse well on top of each other for  $r/N$  roughly in the range 0.1 to 0.5. This indicates that the effective

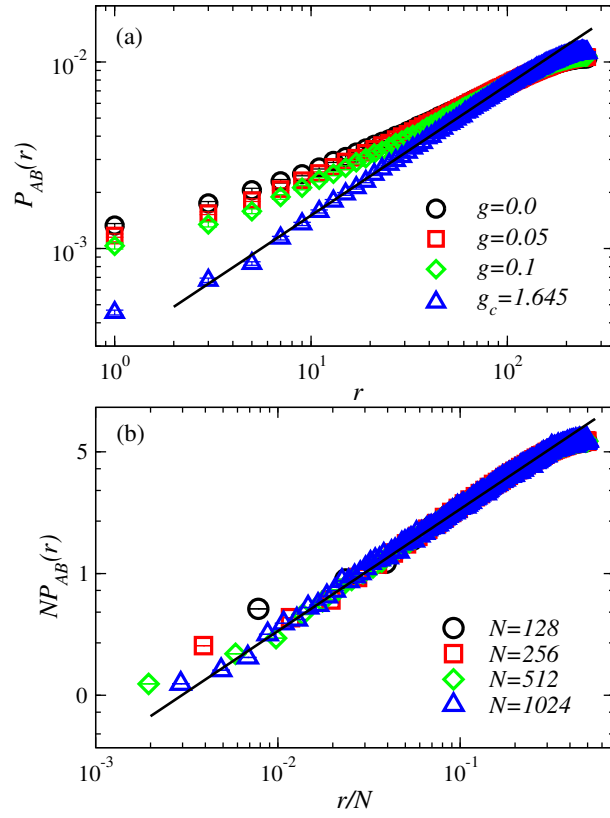


Figure 3.5: Distribution of spinon separations in  $S = 1$  states at and below the VBS transition point  $g_c$ . The lines going through the  $g_c$  points have slope 0.7.

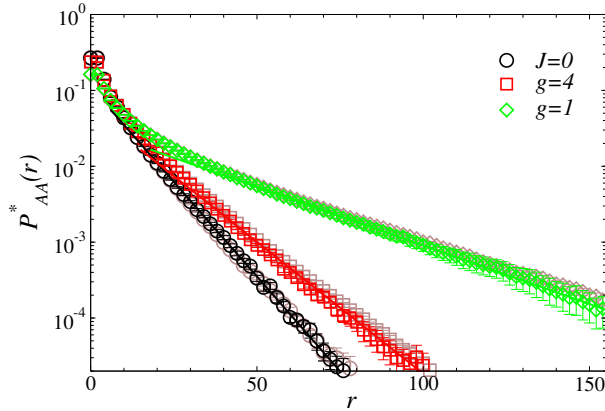


Figure 3.6: The same-sublattice distribution function for  $S = 1$  states at three different values of the coupling ratio. The corresponding distributions  $P_{AA}(r)$  for the  $S = 1/2$  states at the same couplings are shown in lighter (brown) color and they coincide very closely with the  $S = 1$  functions (thus, demonstrating that the single-spinon size can be obtained also from the  $S = 1$  simulations). The system size here is  $N = 1024$  for  $S = 1$  and 1025 for  $S = 1/2$ .

interactions are short-range in nature, with spinons far away from each other behaving as free particles. Clearly, all these results point to deconfined spinons, as expected. While the details of the cause of the repulsive potential are uncertain, it is clear that the sign of the effective interaction is crucial for deconfinement—any weak attractive potential would confine the spinons (and we will investigate this explicitly with a modified model in Sec. 3.4), while short-range repulsive interactions aid deconfinement.

Results for  $P_{AB}(r)$  at the VBS transition and inside the critical phase are shown in Fig. 3.5(a), while results for several chain lengths are shown with rescaled axis to achieve data collapse in 3.5(b). The critical distribution is also here consistent with a power-law,  $P_{AB}(r) \sim r^\gamma$ , with  $\gamma \approx 0.7$  (and with a prefactor decreasing with the system size). Based on these results one may argue that the effective spinon-spinon interactions become increasingly long-ranged as  $g_c$  is approached from the VBS side, although the short-range part is decreasing (the distribution at short distances growing upon decreasing  $g$ ). Inside the critical phase there are again likely logarithmic corrections, and the trend of decreasing

effective spinon-spinon interactions continue as  $g$  decreases.

Next we consider the same-sublattice distribution function  $P_{AA}^*(r)$ , defined in Eq. (3.8). Since the spinons are deconfined and typically are further away from each other than the single-spinon length-scale  $\lambda$ , one would expect that  $P_{AA}^*(r)$  contains essentially the same information as the single-spinon function  $P_{AA}(r)$  for the  $S = 1/2$  state, defined in Eq. (3.6). This is indeed the case in the VBS phase, as demonstrated in Fig. 3.6. Clear exponential decays are observed, and the results coincide almost perfectly with the previous results for  $P_{AA}(r)$  in Fig. 3.2. To reiterate what is going on here, the two spinons in the  $S = 1$  state are on different sublattices, and the unpaired spin on sublattice A in the ket state is correlated to the one on the same sublattice in the bra state, to within the length-scale  $\lambda$  that we have argued describes the internal spinon size. The same holds for the unpaired bra and ket spins in sublattice B. Due to spinon deconfinement the A and B spinons are not bound to each other, however, and typically are far away from each other. Under these conditions the distribution functions  $P_{AA}(r)$  and  $P_{AA}^*(r)$  both contain the same information; the spinon size  $\lambda$ .

As shown in Fig. 3.7(b), the  $S = 1$  function  $P_{AA}^*(r)$  inside the critical phase exhibits an interesting cross-over behavior, most clearly visible at  $g = g_c$ . The behavior at short distances is well described by the same  $r^{-1/2}$  behavior as the corresponding single-spinon function in Fig. 3.3. However, at larger distances the behavior changes to  $\propto 1/r$ . We do not have any explanation for this behavior and it would be interesting to investigate it within bosonization.

### 3.3.2 Break-down of spinons as quasi-particles of a Néel state in one dimension

In a long-range ordered Néel AFM state, the elementary excitations are spin waves (magnons) carrying spin  $S = 1$ . It is then interesting to ask how those change in the nature of the excitations is manifested in our spinon distribution functions.

The continuous spin-rotational symmetry of the ground state of the Heisenberg or J-

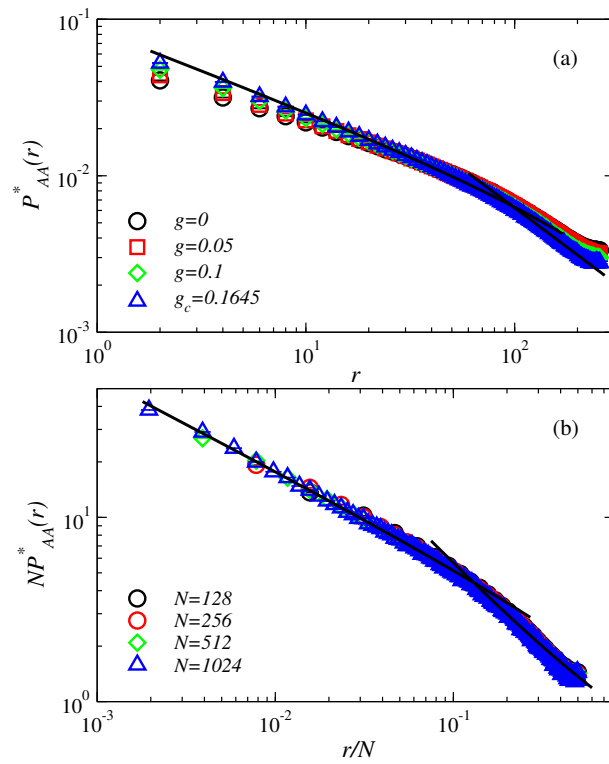


Figure 3.7: Same-sublattice distribution functions for  $S = 1$  states in the critical phase. (a) shows results for different coupling ratios for fixed system size  $N = 512$ , while in (b) results at  $g_c$  are re-scaled to achieve data collapse for several system sizes. The lines have slope  $1/2$  and  $1$  for small and large  $r$ , respectively.

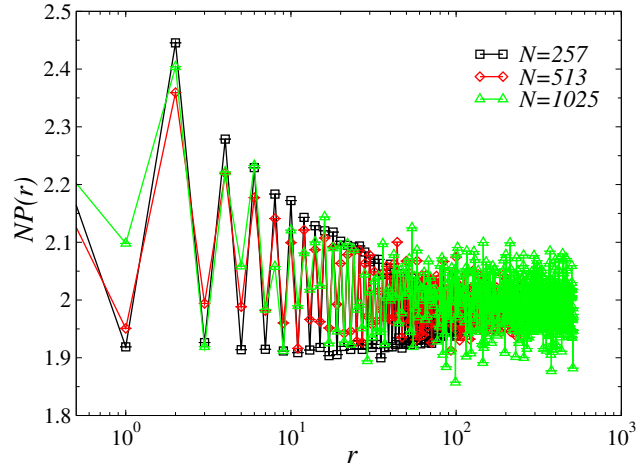


Figure 3.8: Size-scaled spinon overlap function in a Néel-ordered chain with total  $S = 1/2$ . The asymptotically flat (with even and odd- $r$  branches) distribution shows that the spinon is not a well-defined quasi-particle in the Néel state, as expected.

Q chains cannot be spontaneously broken according to the Mermin-Wagner theorem [95]. However, we can circumvent this limitations on 1D ground states by including long-range interactions, in which case the theorem does not apply. We consider unfrustrated power-law decaying interactions defined by the Hamiltonian

$$H = \sum_{i=1}^N \sum_{\substack{N/2 \\ \text{odd } r}} J_r \mathbf{S}_i \cdot \mathbf{S}_{i+r}, J_r > 0, \quad (3.11)$$

where there are no couplings for even separations of spins, while for odd separations the coupling is  $J_r = 1/r^\alpha$ . A similar Hamiltonian was studied before in Ref. [96], where it was found that by tuning the decay exponent  $\alpha$  the system undergoes a continuous phase transition from critical states when  $\alpha > \alpha_c$  to a long-range ordered Néel states when  $\alpha < \alpha_c$ . The critical power depends on details, e.g., on the strength of the nearest-neighbor coupling, and for the above form the critical point is at  $\alpha_c \approx 2.2$ . In our study we are just interested in studying an example of a 1D Néel state and choose  $\alpha = 3/2$ , for which we verified that indeed the system is ordered.

We here investigate the single-spinon distribution function  $P_{AA}(r)$  in an  $S = 1/2$  state for odd  $N$ . In Fig. 3.8, we plot rescaled  $NP_{AA}(r)$  versus  $r$  for different system sizes and find

reasonable data collapse (with some non-monotonic finite size effects for short distances). The behavior here is quite different from the previous cases, Figs. 3.2 and 3.3, with (i) no vanishing of the probability of odd- $r$  separation and (ii) no decay of the rescaled function. The latter behavior indicates that the spinon here is not a well-defined particle, with no concentration of the net magnetization to within an intrinsic wave packet. This is of course not surprising, in the sense that spinons are not expected to be the elementary quasi-particle excitations of the Néel state, and we had also found above that in the critical state the quasi-particles are only marginal, characterized by power-law overlaps. It is still interesting to see that the break-down of the spinons as quasi-particles can be explicitly observed in the distribution function  $P_{AA}(r)$ .

### 3.4 Spinon confinement arising from modulated couplings

In order to observe confinement of spinons, we here use a generalized version of the  $J$ - $Q_3$  model with different nearest-neighbor coupling constants on even and odd bonds. The Hamiltonian is

$$\begin{aligned}
 H = - \sum_{\text{even } i} (J_1 C_{i,i+1} + J_2 C_{i+1,i+2}) \\
 - Q_3 \sum_i C_{i,i+1} C_{i+1,i+2} C_{i+2,i+3}.
 \end{aligned}
 \tag{3.12}$$

When  $\rho = J_2/J_1 \neq 1$ , the Hamiltonian itself breaks translational invariance and there is no longer a VBS phase transition with spontaneously broken symmetry. If we start in a spontaneously formed VBS ( $Q_3/J_1 > g_c$ ) for  $\rho = 1$ , the ground state is doubly degenerate, but once  $\rho > 1$  the degeneracy is broken and the ground state is unique. This is expected to confine the spinons, as the string of out-of-phase bonds formed between two separated spinons is now associated with an energy cost increasing linearly with the separation, instead of the energy only being associated with the domain walls when  $\rho = 1$ . This model was also studied in the presence of an impurity in Ref. [89], and it was found that the localization length of the magnetization distribution forming around the impurity could be tuned by  $\rho$ .

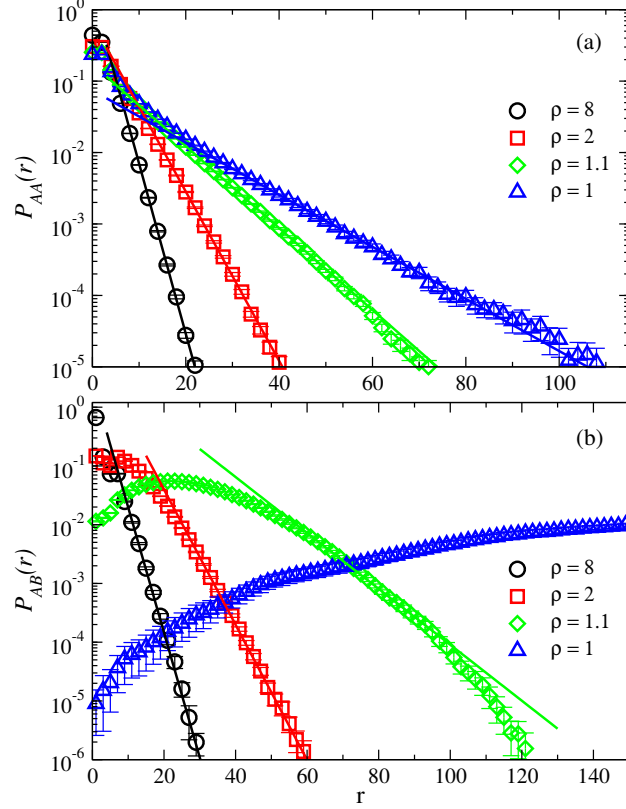


Figure 3.9: Spinon distribution functions in the  $J_1$ - $J_2$ - $Q_3$  chain with  $Q_3 = 4$  and several values of the modulation parameter  $\rho = J_2/J_1$ . (a) shows exponential decays,  $P_{AA}(r) \sim e^{-r/\lambda}$ , of the single-spinon distribution function of the  $S = 1/2$  state, demonstrating well-defined spinons with finite intrinsic size  $\lambda$ . The data points plotted with light brown symbols are the corresponding results for the same-sublattice distribution  $P_{AA}^*$  computed in the  $S = 1$  state. In (b), spinon confinement for  $\rho \neq 1$  is demonstrated in the spinon-distance distribution function;  $P_{AB}(r) \sim e^{-r/\Lambda}$ . The size of the bound state (the confinement length-scale) decreases as the coupling modulation is increased. Data for  $\rho = 1$  are graphed for comparison—in this case the spinons are deconfined and the distribution function does not decay with the separation.

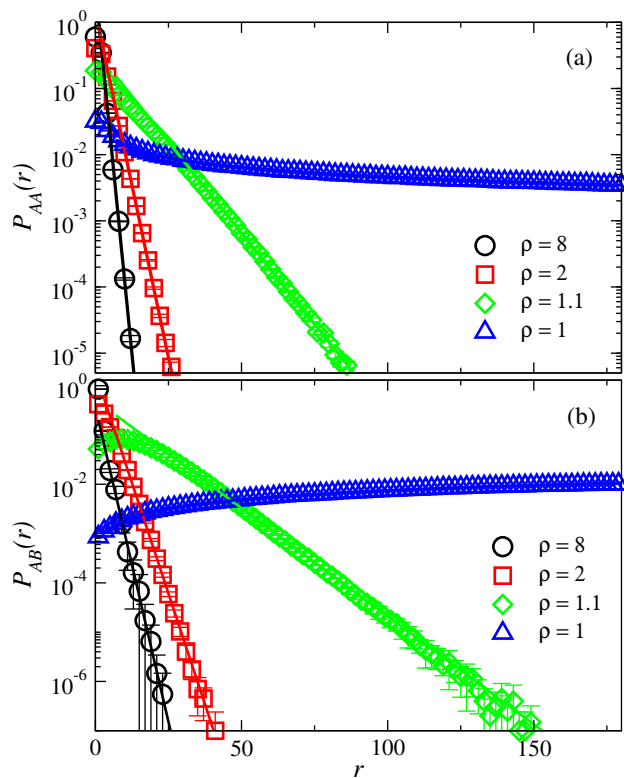


Figure 3.10: The same quantities as in Fig. 3.9 but with the ratio  $Q_3/J_1 = g_c = 0.1645$ . Here the tuning of the modulation parameter  $\rho$  toward 1 corresponds to approaching a critical point.

Here we look at a similar behavior for two spinons binding to each other instead of a static impurity.

We first test for confinement deep inside the VBS phase with  $Q_3 = 4$ . As shown in Fig. 3.9(a), the spinon size  $\lambda$  computed from  $P_{AA}(r)$  in the  $S = 1/2$  ground state becomes smaller when the confining potential increases (tuning  $\rho$  from 1 to 8). Fig. 3.9(b) shows that the confinement length  $\Lambda$  indeed becomes finite once we tune  $\rho$  off 1. For  $\rho$  very close to 1, we should have  $\Lambda \gg L$ , but in practice it is difficult to study this case because the chains have to be very long. Upon increasing  $\rho$  we find that  $\Lambda$  approaches  $\lambda$ . In Fig. 3.9(a) we also show the  $S = 1$  distribution  $P_{AA}^*(r)$ , which coincides almost exactly with  $P_{AA}(r)$ . The agreement is surprisingly good, considering that the confinement length  $\Lambda$  in some of these systems is not much different from  $\lambda$ , and so one may have expected a larger distortion arising from two-spinon interactions.

An interesting observation in Fig. 3.9(b) is the maximum developing in  $P_{AB}(r)$ , seen around  $r = 20$  for  $\rho = 1.1$  and moving to  $R = N/2$  at the uniform point  $\rho = 1$ . In Sec. 3.3 we already argued that there is an effective short-range repulsive interaction between the spinons in the uniform chains, and it is natural that these interactions should persist also for some range of  $\rho$  away from 1, although there is also an attractive part binding the spinons. This, we arrive at the conclusion that when  $\rho$  is close to 1 there is a short-range repulsion followed by a weak attractive potential at longer distances. Judging from the fact that the maximum probability moves toward  $r = 0$  for larger modulation parameters,  $\rho = 2, 8$  in Fig. 3.9(b), the role of the short-range repulsion diminishes (the spinon core softens) as the attractive part is enhanced with growing  $\rho$ .

We also observe similar behaviors in this dimerized model at the critical  $Q_3/J_1$  value, as shown in Fig. 3.10. The main difference is that now the spinon size  $\lambda$  diverges as  $\rho \rightarrow 1$ , instead of tending to a finite value in the VBS phase. Both length-scales are actually smaller than in the VBS phase for larger  $\rho$ , e.g., for  $\rho = 2$ ,  $\Lambda \approx 2.417(9)$  at  $g_c$  while  $\Lambda \approx 3.78(4)$  at  $g = 4$ . This implies that the imposed dimerization in the critical region has a stronger effect than in the ordered VBS phase. In critical region, all lengths diverge, and, therefore, once

we added the explicit dimerization  $\rho \neq 1$  it dominates the physics immediately, while in the VBS phase there are competition effects between the spontaneous VBS and the explicit dimerization, which apparently reduce the effects on the spinon size and confinement length.

### 3.5 Heisenberg ladders

Another way to confine the spinons of the Heisenberg chain is to couple two chains into a ladder, described by the Hamiltonian

$$H = J_1 \sum_{i=1}^L (\mathbf{S}_i^1 \cdot \mathbf{S}_{i+1}^1 + \mathbf{S}_i^2 \cdot \mathbf{S}_{i+1}^2) + J_2 \sum_{i=1}^L \mathbf{S}_i^1 \cdot \mathbf{S}_i^2, \quad (3.13)$$

where the subscripts 1 and 2 label the two chains,  $J_1$  is the nearest-neighbor coupling within the chains, and  $J_2$  is the inter-chain (rung) coupling. It is known that any inter-chain coupling  $J_2$  opens a gap in the excitation spectrum and changes the critical correlations to an exponentially decaying form. This is true for ladders with any even number of legs, while odd-leg ladders are critical and exhibit the universality of the single chain. The situation here is similar to single chains of Heisenberg-coupled integer or half-odd-integer spins, with the former always being gapped according to the now proved ‘‘Haldane conjecture’’ [97,98]. The integer- $S$  chains have localized spinons at the ends of open chains. We here investigate the spinon confinement mechanism in the 2-leg ladder.

Gapped triplons ( $S = 1$ ), which are the low-lying excitations of ladder systems, have already been observed in the excitation spectrum of real materials by inelastic neutron scattering [87]. It has been argued that this observation makes the ladder system the simplest condensed matter system where one can in practice realize a phenomenon similar to quark confinement in particle physics [99]. The energy gap, spin-triplet dispersion relation and the dynamic spin structural factor of the Heisenberg 2-leg ladder model have also been extensively studied by numerical methods [100].

We begin by discussing the standard spin-spin correlation function in the  $S = 0$  ground state. We fit it to the form  $C(r) \propto e^{-\Delta/\xi}$  when  $g = J_\perp/J_\parallel > 0$ , and will later compare the spinon-related length-scales with the correlation length  $\xi$ . Results are shown in Fig. 3.11.

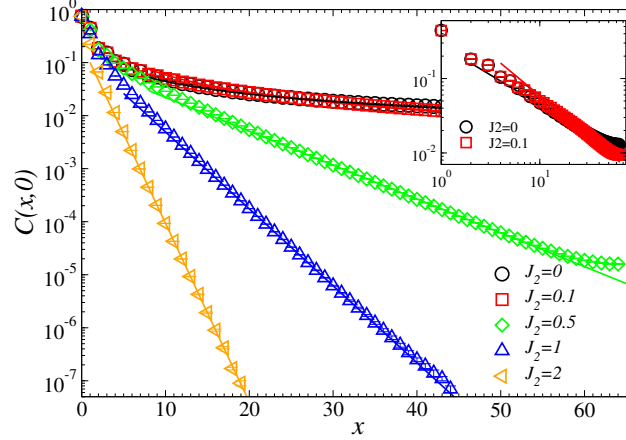


Figure 3.11: Spin correlation function in 2-Leg Heisenberg ladder systems. Here the intra-chain coupling  $J_1 = 1$  and results are shown for several values of inter-chain couplings  $J_2$ .  $C(x, 0)$  decays exponentially when  $J_\perp \neq 0$  and exhibits the power-law decay of the isolated chain when  $J_\perp = 0$ . In the inset, the correlations are large distances on a log-log scale at  $J_2 = 0$  and  $J = 0.1$ . Because here the system length  $L$  is smaller than the correlation length it is not yet possible to observe the exponential decay.

Note that it is very difficult to extract  $\xi$  when  $g$  is small, as  $\xi$  then becomes large and the system size has to be even larger,  $L \gg \xi$ . The inset of Fig. 3.11 illustrates this problem for  $g = 0.1$ . We here focus on rung couplings sufficiently large for extracting  $\xi$  reliably based on our available ladder sizes.

We now turn to the characterization of the spinons. In the 2-leg ladder it is not possible to study a system with an odd number of spins  $N$  without breaking the translational symmetry of the system. We here only discuss calculations in the  $S = 1$  state for even  $N$  and present results for the distributions  $P_{AA}^*(r)$  and  $P_{AB}(r)$  in Fig. 3.12. As we discussed in Sec. 3.3 and Sec.3.4,  $P_{AA}^*(r)$  can reliably give the intrinsic spinon size  $\lambda$  if this length-scale is much smaller than the size  $\Lambda$  of the bound state. In the ladder, the length  $\lambda^*$  as extracted from  $P_{AA}^*(r)$  is always very similar to  $\Lambda$  from  $P^{AB}(r)$ , therefore,  $\lambda^*$  should not be understood strictly as the size of an individual spinon (which cannot even be realized in a translationally invariant system, as discussed above). However, from the comparisons of the spinon size extracted from the two same-sublattice distributions  $P_{AA}(r)$  and  $P_{AA}^*(r)$

in Fig. , we know that  $P_{AA}^*(r)$  actually is a surprisingly good measure of the single-spinon overlap also when the two length-scales  $\lambda$  and  $\Lambda$  are similar. In the ladder systems,  $\lambda^*$  is even somewhat larger than  $\Lambda$ , e.g., at  $J_2 = 1$ ,  $\lambda \approx 3.9$  and  $\Lambda = 3.5$ .

We recently studied a 2D  $J$ - $Q_3$  model with a VBS state [39]. In that case, an individual spinon in an  $S = 1/2$  state can be studied and we found that the so extracted  $\lambda$  is considerably smaller than the bound state of two spinons. We interpreted this as being due to a softness of the extended spinons, which are expected to be a kind of vortices in 2D. Such soft spinons shrink when they are subject to mutual attractive interactions and form a pair. Also there the single-spinon length  $\lambda^*$  extracted from the  $S = 1$  state is somewhat larger than  $\Lambda$ . Given this similarity, we also interpret  $\lambda^* \approx \Lambda$  in the Heisenberg ladder as due to soft spinons. In contrast, in the modulated chains discussed in Sec. 3.4, an individual spinon is much smaller than the bound state in the limit of weak modulation, and this can be naturally interpreted as the individual spinons retaining their individual properties also when in a bound state.

### 3.6 Detecting spinons in spin correlations

The definitions  $\Lambda$  and  $\lambda$  of the spinon length-scales are closely tied to the VB basis, and their underlying distribution functions are not directly physically measurable quantities. It is therefore interesting to investigate whether the same length scales also appear in *bona fide* quantum-mechanical expectation values as well. The natural candidate is the standard spin correlation function using the operator Eq.(2.12) in the total-spin sectors with  $S = 1/2$  and  $S = 1$ . It is clear that these correlations do not differ significantly from those in the ground state with  $S = 0$  and we therefore look at the difference between these correlations,

$$\Delta_S(r) = C_S(r) - C_0(r), \quad (3.14)$$

where the subscript on  $C$  indicates the spin sector in which it is computed. We plot the absolute value of these functions for a  $J$ - $Q_3$  chain in Fig. 3.13(a) and for a  $J_1$ - $J_2$ - $Q_3$  chain

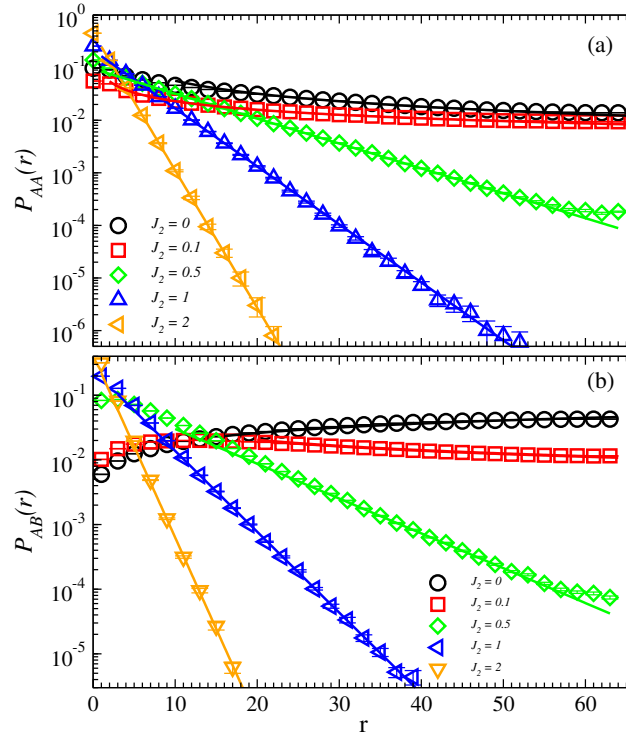


Figure 3.12: Spinon distribution functions in  $S = 1$  states of Heisenberg ladders with different run couplings  $J_2$ . Both distribution functions are exponentially decaying for  $J_2 = 0.5, 1$ , and  $2$ , while for  $J_2 = 0.1$  the system size is not sufficiently large for observing the expected asymptotic exponential decay. The forms for the critical system at  $J_2 = 0$  were discussed in Sec.3.3.

with a small modulation parameter  $\rho = 1.1$  in Fig. 3.13(b). In both cases,  $Q_3$  is relatively large, so that the uniform  $J$ - $Q_3$  chain is deep inside the VBS phase.

For  $S = 1/2$ , we find an almost pure exponential decay in Fig. 3.13(a), with a decay constant very similar to the single-spinon size  $\lambda$  obtained previously for this VBS state. This agreement confirms that  $\lambda$  is an actual physical characteristic of the  $S = 1/2$  state. In the  $S = 1$  state, we find an interesting structure, where at short distances the behavior follows closely the same exponential decay as in the  $S = 1/2$  state, while for larger distances there is a rather dramatic change, with a phase shift in the staggered correlations (which here is not seen directly as we are grasping only the absolute value, but the shift is reflected indirectly in the sharp dip to very small value within a narrow  $r$ -range), followed by a flattening out of the correlations. The phase shift and subsequent flattening out can be understood in terms of deconfined spinons in the following way: Since we are looking at a state with total  $S^z = S = 1$ , the spin correlations at long distances are completely dominated by the contributions from the unpaired spins (the singlet background having exponentially decaying correlations). Since these spinons always reside on different sublattices, we will get positive contributions from odd distances, in contrast to the normal phase of the correlations an antiferromagnet, which is negative at odd distances. We find the standard phase of the correlations in the  $S = 1$  state as well at short distances. Given this, there must be a phase shift at some distance  $r$ . The exact location of the phase shift depends on the model parameters and the chain length in a way which we have not yet disentangled.

As shown in Fig. 3.14, in the case of the ladder systems we do not find any phase shifts and in all cases studied the correlation difference between the  $S = 1$  and  $S = 0$  is essentially a pure exponential form. In the ladder we have not found any case where  $\Lambda$  is significantly larger than  $\lambda$  and most likely these quantities both diverge in the same way as  $J_2/J_1 \rightarrow 1$ . There is therefore no clear regime of weak deconfinement, although the term may be misleading when the length scales both do become large. We therefore use the term *marginal deconfinement* to describe this scenario.

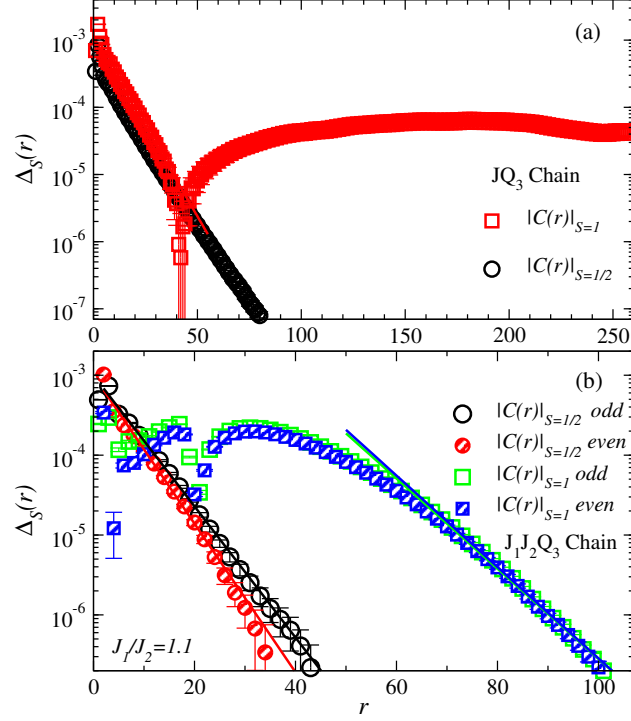


Figure 3.13: Absolute value of the spin correlation function in the  $S = 1/2$  and  $S = 1$  state, after subtraction of the  $S = 0$  correlation function according to Eq. (3.14). (a) is for a  $J$ - $Q_3$  chain with  $Q_3/J = 4$  and (b) is for a  $J_1$ - $J_2$ - $Q_3$  chain with  $J_2/J_1 = 1.1$  and  $Q_3/J_1 = 4$ . In both cases the chain length is  $N = 512$ . The sharp dips where the error bars are large for the  $S = 1$  quantities correspond to phase shifts. In (b) the even- $r$  and odd- $r$  branches are graphed in different colors to show the even-odd effects, while in (a) these effects are small. All lines correspond to exponential fits.

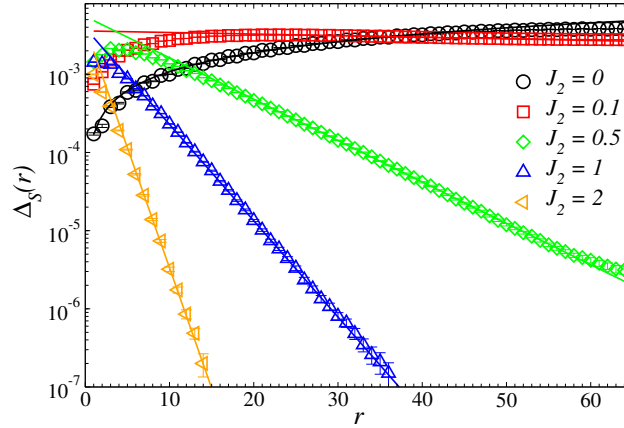


Figure 3.14: Spin correlation difference for Heisenberg ladder systems in the  $S = 1$  sector. The lines show exponential fits.

### 3.7 Summary and discussion for 1D chains

We have used a numerical technique based on valence-bond projector QMC simulations to study the spinon size  $\lambda$  and the confinement length  $\Lambda$  in 1D spin systems. We found that when a system has only one spinon, the overlap between valence-bond states with unpaired  $S^z = 1/2$  moment residing at distance  $r$  away from each other decays as  $e^{-r/\lambda}$  in a gapped VBS, where we interpret  $\lambda$  as characterizing the intrinsic spinon size. In a critical state, the overlap instead decays as  $r^{-1/2}$ , which we interpret as spinons that are only marginal particles, on the verge of losing their identities as quasi-particles. When the system has two spinons, the distribution function for the distance between them decays as  $e^{-r/\Lambda}$  if the spinons are confined (which we have studied using a modulated pattern of weak and strong coupling constants, which leads to a linear spinon-binding potential), with  $\Lambda$  characterizing the size of the bound state. For deconfined spinons (which we have studied in VBS states and critical states) we found that the distribution function instead exhibits a broad peak at the largest separation, demonstrating a weak repulsive potential between the spinons. We studied the Heisenberg 2-leg ladder system. By tuning the rung coupling, the system can be driven from a deconfining phase (two decoupled chains) to a confining phase. In this case the spinon size is always similar to the size of the bound state.

In the Bethe-Ansatz solution of the Heisenberg chain, spinons are non-interacting particles (kinks and anti-kinks), but it should be noted that these particles are obtained from the original spin degrees of freedom using a highly non-local transformation. What we have probed here is instead more direct measures of the spatial “concentration”,  $P_{AA}(r)$ , of the total magnetization of a single spinon, and the correlations between (essentially) the center-of-mass of two such distributions,  $P_{AB}(r)$ . Since our calculation projects out the lowest state with given total spin, in the case of  $S = 1$  the total momentum  $k = \pi$  (in the case of a chain with  $N = 4n$  sites). Therefore the spinons here are not propagating, having individual spin 0 and  $\pi$  (these giving the lowest possible energies in light of the des Clauseaux-Pearson dispersion). In principle our calculations can also handle total momentum away from  $k = \pi$ , but in practice, due to phase problems in the Monte Carlo sampling, we are restricted to momenta close to 0 and  $\pi$ .

In the future it would be interesting to more exhaustively characterize all the length-scales of the system (including  $\lambda$ ,  $\Lambda$ , as well as the spin and VBS correlation lengths) and their divergences under the various conditions afforded by the models we have performed initial studies on here.

### 3.8 RVB Spin Liquid

RVB spin liquids have been considered as promising candidates for explaining high temperature superconductivity in cuprates when doped [2, 5]. It is therefore also interesting to examine in detail properties of the insulating host system. Recently, it was found that the simplest equal-amplitude short-bond RVB is a quantum-critical VBS, with exponentially decaying spin correlations but power-law dimer correlations [45, 46]. It has been long expected that the RVB hosts deconfined spinon excitations [38].

The parent Hamiltonian of the short-bond RVB was found recently [44]. Although the  $S = 1/2$  and  $S = 1$  states we study here may not be its exact lowest states in these sectors, one can still expect them to be good variational states—the actual excitations of the Cano-Fendley Hamiltonian should be very similar.

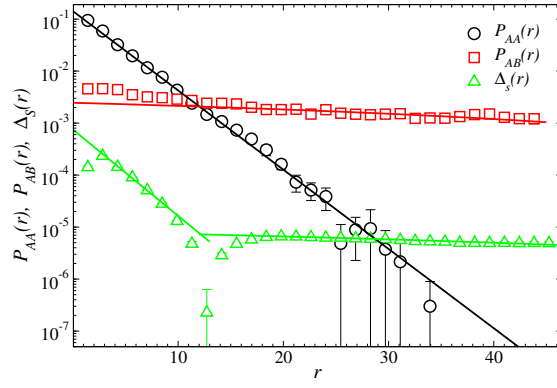


Figure 3.15: Spinon distributions and correlations along the diagonal lattice direction of the RVB spin liquid. Black circles show the single-spinon overlap  $P_{AA}(r)$  in an  $S = 1/2$  state on a  $65 \times 65$  lattice. The exponential decay (fitted line) gives the spinon size  $\lambda = 2.96(1)$  lattice spacings. Red squares show the two-spin distribution  $P_{AB}(\mathbf{r})$  in the  $S = 1$  state on a  $64 \times 64$  lattice, fitted to  $\sim 1/r^\alpha$  with  $\alpha \approx 0.6$ . The green triangles show the absolute value of the difference  $\Delta_S(r)$  between the spin correlations in the  $S = 1$  and  $S = 0$  systems. This quantity exhibits both a spinon-size effect (exponential short-distance decay) and deconfinement (weak power-law decay at long distances). There is a phase shift at  $r \approx 9\sqrt{2}$ .

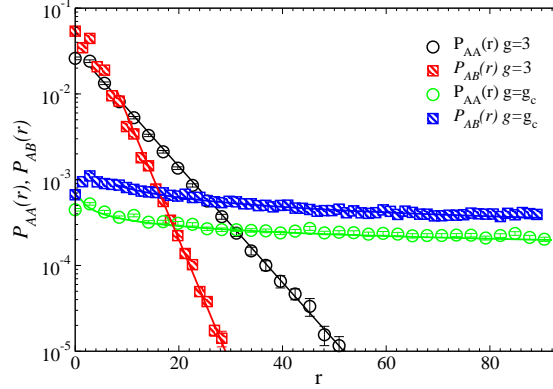


Figure 3.16: Spinon distributions for the 2D  $J\text{-}Q_3$  model on  $L = 128$  and  $129$  lattices at  $g = 3$  (VBS) and  $g_c = 1.5$  (critical). The lines are exponential fits for the  $g = 3$  VBS, giving the single-spinon size  $\lambda = 6.4$  extracted from  $P_{AA}(r)$  in the  $S = 1/2$  state and the confinement length  $\Lambda = 3.1$  extracted from  $P_{AB}(r)$  in the  $S = 1$  state. Both lengths diverge as  $g \rightarrow g_c$ , where the distributions decay algebraically.

We characterize the RVB spinons in Fig. 3.15. The  $S = 1/2$  distribution  $P_{AA}(r)$  demonstrates a well-defined intrinsic spinon wave packet, decaying as  $e^{-r/\lambda}$  with the spinon size  $\lambda = 2.96(1)$ . The  $S = 1$  distribution  $P_{AB}(r)$  is peaked at short distances and appears to decay as  $r^{-\alpha}$  with  $\alpha \approx 0.6$ . This implies marginal deconfinement due to weak attractive spinon-spinon interactions. In Fig. 3.15 we also show that the length-scales observed in  $P_{AA}(r)$  and  $P_{AB}(r)$  are manifested in the  $S = 0, 1$  correlation function  $C(r)$  as well. Hence, the distributions do capture actual physical, basis-independent length-scales [78].

### 3.9 2D $J\text{-}Q$ model

The Néel–VBS transition (the same as AFM–VBS transition) has been debated for years [101]. In 2004, Senthil et al. presented a scenario encompassing several earlier works [101–103] and further proposed a mechanism leading to a generic continuous transition [28–30]. This scenario is at odds with the “Landau rule” according to which transitions between the two ordered states breaking unrelated symmetries should be first-order. A key aspect of the theory is that both order parameters arise out of spinons, which condense in the Néel state and confine in the VBS (where valence bonds can be regarded as tightly bound spinon

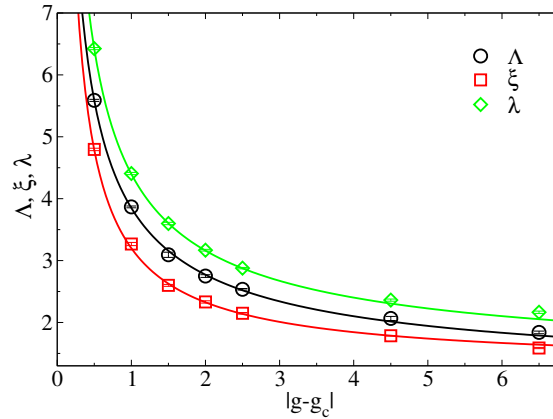


Figure 3.17: The confinement length  $\Lambda$ , the correlation length  $\xi$ , and the spinons size  $\lambda$  in the VBS phase and approaching the critical point ( $g_c = 1.50$ ) of the  $J$ - $Q_3$  model. The calculations were done with  $L = 128$  and  $129$ . The power-law fits (solid curves) are discussed in the text.

pairs). Exactly at the DQC point separating the ordered states the spinons should deconfine. Although opposing views have been put forward [104–106], the generic continuous nature of the Néel–VBS transition has support in QMC studies of  $J$ - $Q$  [24, 64, 107, 108] and other [25] models, including a predicted emergent  $U(1)$  symmetry reflecting the gauge structure of the theory, where spinons interact with an  $U(1)$  gauge field in a non-compact  $CP^1$  action.

The DQC scenario motivates us to investigate spinons directly, by computing the spinon size  $\lambda$  and the confinement length  $\Lambda$  in VBS states and approaching the critical point. As shown in Fig. 3.16, both  $P_{AA}(r)$  and  $P_{AB}(r)$  are exponentially decaying in the VBS phase, with  $\lambda = 6.4(1)$  and  $\Lambda = 3.1(1)$  at  $g = 3$ . Surprisingly, the intrinsic size of a single spinon is, thus, much larger than the bound state of two spinons. We interpret this as a softness of the spinon, which causes it to shrink when subject to attractive interactions from an anti-spinon. This should be a signature of the vortex-nature of the spinon, as the opposite circulations of the members of the pair should lead to cancellations away from the double-vortex core. Such shrinkage of vortices could in principle also occur under certain conditions in superconductors [109–111].

Approaching the critical point both  $\lambda$  and  $\Lambda$  diverge, and at the critical point power laws  $P_{AA}(r) \sim 1/r^\alpha$  and  $P_{AB}(r) \sim 1/r^\beta$  obtain, with  $\alpha \approx \beta = 0.3 \pm 0.1$ . In the DQC theory it is

predicted that the divergence of  $\Lambda$  should be faster than the correlation length  $\xi$ ;  $\Lambda \propto \xi^{1+k}$ , with  $k > 0$  and less than the exponent governing the rate of divergence of the cross-over length-scale of the emergent U(1) symmetry (which should be the largest length-scale) [29]. We extract  $\xi$  from spin-spin correlations. The length-scales  $\xi$  and  $\Lambda$  are graphed versus the coupling ratio in Fig. 3.17. Using lattice sizes  $L$  up to 128, we can reliably extract  $\Lambda$  and  $\xi$  when they are roughly less than 10—beyond which the size-dependence becomes significant and extrapolating to infinite size is difficult. Although we can therefore not reach far into the asymptotic scaling regime, the dependence on  $g - g_c$  is still consistent with the expected power-law divergence, if we allow a constant correction, i.e., fitting to the forms  $\Lambda = a + b(g - g_c)^{-\mu}$  and  $\xi = a + b(g - g_c)^{-\nu}$ . We then find  $\mu = 0.7(1)$  and  $\nu = 0.8(1)$ . The correlation-length exponent  $\nu = 0.59(2)$  was obtained in Ref. [24] based on finite-size scaling collapse for larger systems in the close neighborhood of the critical point. The results based on Fig. 3.17 have large error bars and may also be affected by further non-asymptotic corrections. Regardless of the precise values of  $\mu$  and  $\nu$ , it is clear that  $k = \mu/\nu - 1$  is very close to 0. This is consistent with the value 0.20(5) obtained in Ref. [108] for the exponent governing the U(1) to  $Z_4$  cross-over. The exponent describing the divergence of  $\lambda$  in Fig. 3.17 is 1.1(3); within error bars equal to  $\Lambda$ .

### 3.10 Revisit 1D deconfinement

In the 1D VBS phase, without enforced dimerization,  $J_1 = J_2$  in Eq. (3.12), the spinons are small and deconfined, as shown in Ref. [78]. By turning on a symmetry-breaking dimerization,  $\rho = J_2/J_1 > 1$ , one can tune the confinement length from arbitrarily large to arbitrarily small [89, 112]. Here, to compare with the 2D model approaching its critical point, we instead show results for  $g = Q_3/J_1$  fixed at the critical value  $g_c = 0.1645$  when  $J_1 = J_2$  (where spinons are deconfined). Keeping  $g = g_c$  and turning on the static dimerization,  $\rho > 1$ , we observe in Fig. 3.18 that  $\Lambda \approx \lambda$  ( $\Lambda$  being slightly larger), with both lengths diverging as  $\rho \rightarrow 1$ . This is similar to the behavior observed in the 2D model (apart from the lack of spinon shrinkage). Thus, *the fact that the spinon size and the confinement length are*

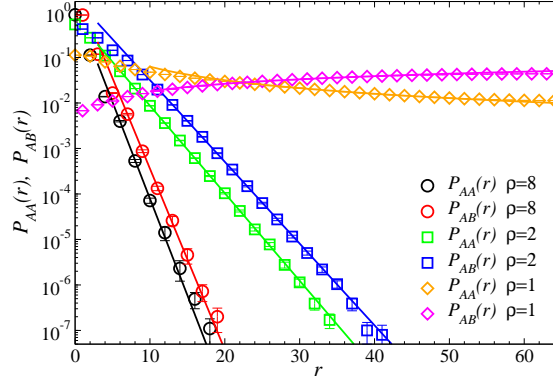


Figure 3.18: Spinon distributions in the  $J_1$ - $J_2$ - $Q_3$  chain with  $Q_3/J_1 = 0.1645$  (the critical point when  $J_1 = J_2$ ) for three ratios  $\rho = J_2/J_1$ . The straight lines for  $\rho > 1$  are exponential fits and the curves for  $\rho = 1$  are power-law fits.

*both divergent does not invalidate the deconfinement picture.* At the critical point, the 1D “spinon shape” distribution  $P_{AA}(r)$  also decays as a power-law, while the pair distribution  $P_{AB}(r)$  is peaked at the longest distance, reflecting marginal (critical) spinons subject to weak repulsive interactions [78]. The main difference in the 2D model is that the effective spinon-spinon interactions are attractive, not only in the VBS phase but also at criticality.

### 3.11 Conclusion and discussion for the deconfinement of spinons in 2D

We showed that a spinon in the 2D  $J$ - $Q_3$  model shrinks when a bound-state (triplon) is formed. We should stress here that the reason why the vortices do not annihilate is that we restrict the system to the  $S = 1$  sector, while spinon annihilation would bring it back to the  $S = 0$  ground state. Both the spinon size and the confinement length diverge as the critical VBS–Néel point is approached, and at the critical point the distribution functions decay as power laws. This is also necessary for continuity, because in the Néel state both distributions become flat (as we discussed for 1D systems in Ref. [78] and have also verified in 2D), when the spinons completely lose their identity as individual objects.

Our scenario deviates from a simple picture of the near-critical triplon being a large object formed by two small particles. The question then is: Are the spinons nevertheless

deconfined, independently propagating excitations? We showed with a known example that in 1D that is possible. The most plausible scenario in 2D is that the behaviors found here are due to weak attractive interactions between a spinon and an anti-spinon—as would in fact be expected based on the DQC theory, where interactions are mediated by a gauge field (but the sign of the effective spinon-spinon interactions is not immediately clear). Note that we have only studied the lowest  $S = 1$  state, and in higher states the kinetic energy should overcome the weak attraction, leading to essentially independent spinons, as found when comparing the critical  $J$ - $Q$  model with a gas of free bosonic  $S = 1/2$  excitations [113].

In the simple RVB spin liquid, we also found weak attractive interactions, but in this case the spinons are small. The differences between the RVB liquid and the critical  $J$ - $Q_3$  model should be due to the fact that the spin correlations decay exponentially in the former (and there is a spin gap), while they have a power-law decay the latter. Both models exhibit algebraic dimer correlations, which should be responsible for the residual spinon interactions. In the 1D case, full deconfinement can be seen thanks to repulsive interactions, although the critical spinons themselves are not small particles (as in the 2D  $J$ - $Q_3$  model), being instead marginally localizable objects described by power-law overlaps. Still, it is rigorously known that these marginal particles do propagate as individual  $S = 1/2$  degrees of freedom [72].

The excitations of collective quantum states only depend on the nature of the ground state, regardless of microscopic details. We therefore expect our results to be generic to 2D columnar VBS states and Néel-VBS critical points. Our results suggest that near-critical and critical VBS are close 2D analogues to the 1D critical spin chains, with the differences essentially due to the different topological aspects of the spinons; vortices versus kink solitons.

## Chapter 4

# Properties of Resonating Valence Bond Spin Liquids and Critical Dimer Model

### 4.1 Introduction

The two-dimensional (2D) resonating-valence-bond (RVB) spin-liquid state introduced by Anderson has been studied extensively during the past two decades, with the hope that it (when doped) might provide an opportunity to understand high-temperature superconductivity in cuprates. [2] Such RVB states, which do not feature any long range magnetic order or broken lattice symmetries (but are believed to exhibit non-local, topological order [67,114]) are also of broader interest in the context of frustrated magnetism, where they were first considered. [115] In studies of specific Hamiltonians, RVB states can be considered as variational ground states. The extreme RVB state built out of only the shortest possible (nearest-neighbor) valence bonds (singlets), with equal weights for all bond configurations (which in the case considered here will be on the square lattice), does not have any adjustable parameters (as long as the signs of the wave function are not considered—in the standard RVB all coefficients are equal and positive). One can also parametrically introduce longer bonds in amplitude-product states. [53] In two dimensions these states are spin liquids if the amplitudes decay sufficiently rapidly (exponentially or as a high power) with the bond length. We report here extensive studies of the RVB state, with only short (length 1) bonds, as well as in the presence of a fraction of bonds (the second bipartite ones

of length  $\sqrt{5}$ ).

The search for Hamiltonians with RVB ground states has been an ongoing challenge during the past two decades. One way to approach the problem is through quantum dimer models (QDM), in which the internal singlet structure of the valence bonds is neglected. The valence bonds are replaced by hard-core dimers, and different dimer configurations are considered as orthogonal states. [43] The effective Hamiltonians in this space, which describe the quantum fluctuations of the dimers, can have crystalline dimer order [corresponding to a valence-bond-solid (VBS) in the spin system] or be disordered (corresponding to a spin liquid). QDMs have many interesting and intriguing properties, e.g., the special Rokhsar-Kivelson (RK) points at which the wave-function of a dimer model corresponds exactly to the statistical mechanics of classical dimers. [43, 116–118] On the square lattice the classical dimer model (CDM) has critical dimer-dimer correlations, decaying with distance  $r$  as  $1/r^2$  (a rigorous result [119, 120]) which then is also the case at the RK point separating two different VBS states on the square lattice. On the triangular lattice, this isolated spin-liquid point with critical dimer correlations is replaced by an extended liquid phase with exponentially decaying dimer correlations. [121] The same physics can be achieved on the square lattice by introducing dimers between next-nearest-neighbor sites. [66] We will here also provide some further results for the CDM, in order to elucidate in more detail the relationship between the RVB and the CDM.

Formally, the QDMs can be related exactly to generalized  $SU(N)$  symmetric spin models. [101] In the limit of  $N \rightarrow \infty$  the valence-bond states become exactly orthogonal dimer states. Whether or not the physics of the quantum dimer models can be extended down to the physically most interesting case of  $SU(2)$  spins is in general not clear (unless the  $N = 2$  features are built in from the start, as can be done in *generalized QDMs* [122]). Moessner and Sondhi have devised a procedure to mimic a system of large- $N$  spins by decorating an original lattice of  $S = 1/2$   $SU(2)$  spins with additional spins, and this way a Hamiltonian with spin-liquid ground state can be constructed. [123] Very recently, Cano and Fendley constructed a Hamiltonian the ground state of which is exactly the short-bond RVB state

on the square lattice (without decoration). [44] While this Hamiltonian is a complicated one with multi-spin interactions that are unlikely present in real systems, the achievement is important as it shows that local  $SU(2)$  spin models with RVB states do in principle exist also on simple lattices.

#### 4.1.1 Correlations in RVB and dimer states

Perhaps surprisingly, very few physical properties of RVB spin liquids have actually been computed. While Monte Carlo simulations of amplitude-product states on the 2D square lattice were carried out some time ago, only the simple spin-spin correlations were calculated. [53] They decay exponentially in the case of the short-bond state. On the other hand, the fact that the dimer-dimer correlations of the CDM (or, equivalently, the QDM at the RK point) decay with a power-law clearly suggests that there should be similar critical correlations also in the RVB state (if the QDM is qualitatively faithful to it). The dimer-dimer correlations of the RVB state are not physical correlations, however, as the dimer basis is non-orthogonal and overcomplete.

In this paper, we use an improved Monte Carlo sampling scheme for valence bonds [64] to compute the physical correlation function most closely related to the dimer-dimer correlations of the CDM, namely, the four-spin correlation function

$$D_{xx}(\mathbf{r}_{ij}) = \langle B_x(\mathbf{r}_i) B_x(\mathbf{r}_j) \rangle, \quad (4.1)$$

where  $B_x(\mathbf{r}_i)$  is a scalar operator defined on a bond,

$$B_x(\mathbf{r}_i) = \mathbf{S}(\mathbf{r}_i) \cdot \mathbf{S}(\mathbf{r}_i + \hat{\mathbf{x}}), \quad (4.2)$$

and  $D_{yy}$  and  $D_{xy}$  can be defined analogously. Here the lattice coordinate of spin  $i$  is denoted  $\mathbf{r}_i$  and  $\hat{\mathbf{x}}$  is the lattice vector in the x-direction. The operator  $B_x(\mathbf{r}_i)$  provides a measure of the singlet probability on the bond between site  $i$  and its “right” neighbor, which is larger on a valence bond (in which case the operator is diagonal) than between two valence bonds (where the operator is off-diagonal and leads to a rearrangement of the two valence bonds). It is therefore appropriate to consider  $B(\mathbf{r}_i)$  as the “quantum dimer” operator to

be used in place of the dimer density  $n_x(\mathbf{r}_i) \in \{0, 1\}$  in the CDM. Because of the non-orthogonality of the valence-bond basis,  $D_{xx}(\mathbf{r})$  is not, however, identical to the classical dimer-dimer correlation function. The two systems and their dimer correlation functions become identical in  $SU(N)$  symmetric generalizations of the RVB when  $N \rightarrow \infty$ . [101]

We will here show that  $D_{xx}(r)$  for the standard  $S = 1/2$   $SU(2)$  spins decays much slower than the classical correlator, as  $1/r^\alpha$  with  $\alpha \approx 1.20$ . These correlations, which are peaked at momenta  $\mathbf{q} = (\pi, 0)$  and  $\mathbf{q} = (0, \pi)$ , correspond to critical fluctuations of a columnar valence-bond-solid (VBS). The exponent  $\alpha < 2$  in the RVB spin liquid corresponds to power-law divergent Bragg peaks, while in the CDM these peaks are only logarithmically divergent. As a consequence of the non-orthogonality of the valence-bond basis, the RVB is, thus, significantly closer to an ordered VBS state than is the CDM (or QDM). This result was first reported by us in a conference abstract [124] and in an unpublished earlier version of this paper [125], and was also found in independent parallel work by Albuquerque and Alet. [46] Here we provide further details on the dimer correlations and their significance.

We also study systems doped with two monomers and compute the distribution function of the monomer separation. A well known result for the CDM is that the monomers are deconfined, with the distribution function  $M(r)$  decaying with the separation  $r$  as  $A(L)/r^\beta$ , where  $\beta = 1/2$  and the prefactor  $A(L)$  decays with the system size  $L$  in such a way that the distribution is normalized for all  $L$ . For the RVB state, we find a more rapid power-law decay, with  $\beta \approx 0.83$ , which still corresponds to deconfined monomers.

It is known that the dimer correlations of the CDM decay as  $1/r^2$  also in the presence of longer bipartite bonds (while non-bipartite bonds leads to a non-critical phase, with exponentially decaying correlations). As we will explain further below and in Appendix B, the exponent  $\alpha$  in this case does not correspond to these leading correlations, however, but a subleading contribution decaying as  $1/r^\alpha$  with  $\alpha > 2$ . This exponent and the monomer exponent  $\beta$  are non-universal, depending on details of the model (the fugacities corresponding to the longer bonds). [66] We also study here the RVB including longer bonds (the second bipartite bond, which connects fourth-nearest neighbors as considered previously in

the CDM [66]) and find that also in this case  $\alpha$  and  $\beta$  change with the concentration of longer bonds. In contrast to the CDM, the leading dimer correlations are always (at least for the range of parameters studied here) controlled by  $\alpha$ , however, since  $\alpha < 2$  for the RVB.

#### 4.1.2 Height representation and topological sectors

A key notion for relating the various results on the CDM and (we believe) the RVB model also, is that of “height model,” or equivalently a  $U(1)$  classical field theory. This means that all the long-wavelength behaviors of the system are captured by a coarse-grained scalar field  $\bar{h}(\mathbf{r})$ . The dimer density operators and monomer defects can all be expressed in terms of  $\bar{h}(\mathbf{r})$ , and the weighting of its configurations is proportional to  $\exp(-F_{\text{tot}})$ , where

$$F_{\text{tot}} = \int d^2\mathbf{r} \frac{1}{2} K |\nabla \bar{h}(\mathbf{r})|^2. \quad (4.3)$$

The height mapping for square-lattice dimers was introduced over twenty years ago. [126–128] The use of such a mapping to explain correlation functions originated earlier (effectively for dimers on a honeycomb lattice) with Blöte, Hilhorst, and Nienhuis. [129, 130]

The key parameter in (4.3) is the dimensionless stiffness constant  $K$ . It can be shown that the exponents  $\alpha$  and  $\beta$  measured in our simulations, as well as the coefficients of a “pinch-point” singularity in the dimer-density structure factor, and also the ratios of the probabilities of different topological (winding number) sectors, are all functions purely of  $K$ . The details of the height-model construction underlying this result are given in Appendix B. It will be shown in Sec. 4.3 that all our measurements based on Monte Carlo simulations of the CDM and RVB consistently give the *same* value of  $K$  for a given model, demonstrating the validity of the height model. That is expected for the CDM, for which the height approach is well known; here we show that it is pertinent to the RVB as well.

A related aspect of RVB states and the CDM is that their bond configurations on periodic lattices can be classified according to a topological winding number. [43] We here define the winding number  $W = (W_x, W_y)$  as used in Ref. [131]. Drawing a path in the

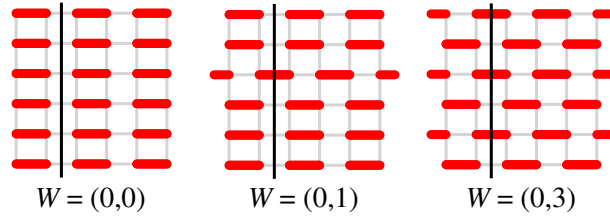


Figure 4.1: Configurations in different winding number sectors,  $W = (W_x, W_y)$ . Here  $W_y$  is given by the number of bonds crossing the line drawn in the  $y$ -direction (since those bonds are at even  $y$ —shifting the bond configuration by one step in the  $y$ -direction leads to  $W_y \rightarrow -W_y$ ). The last case is the unique configuration in its winding number sector and constitutes the staggered state of the QDM.

$y$  direction,  $W_y$  is the number of  $x$ -dimers crossed at even  $y$  minus the number of such dimer crossing at odd  $y$  (see Fig. 4.1). An equivalent definition [43] uses one of the  $W = 0$  single-domain states, such as the one in Fig. 4.2(a), as a reference state. As shown in Fig. 4.2(c), a direction can be assigned to loops of the transition graph so that each carries a “lattice flux”; if we call the net fluxes  $(\Phi_x, \Phi_y)$ , then  $(W_x, W_y) = (\Phi_y, \Phi_x)$  [or, depending on exactly which reference state is used and how the  $y$  coordinates are assigned, we could have  $(W_x, W_y) = (\Phi_y, -\Phi_x)$ —the signs are normally not important]. This definition can be directly extended to systems with long dimers, by associating that flux (which can have both  $x$  and  $y$  components, for cases where there are bonds not along the  $x$  or  $y$  axis) with a line connecting their endpoints. A third definition of the same winding number is (proportional to) the net height difference added up along a path crossing the system in the  $x$  or  $y$  direction, using the rules detailed in Appendix B. The possible winding values for an  $L \times L$  lattice are  $W_x, W_y \in \{-L/2, -L/2 + 1, \dots, L/2\}$ . The equal-weighted (CDM) ensemble is dominated by the winding number sector  $\mathbf{W} = (W_x, W_y) = (0, 0)$  [as follows from  $\nabla \bar{h} = 0$  being the minimum of (4.3)].

Recently, extended QDMs have been considered, with interaction terms that can drive the system into ground states with non-zero  $\nabla h$  in a sequence of commensurate locking transitions. [131, 132] Quantum phase transitions involving these states are unusual, exhibiting aspects of deconfinement on a fractal curve of critical points (forming a Cantor set, which

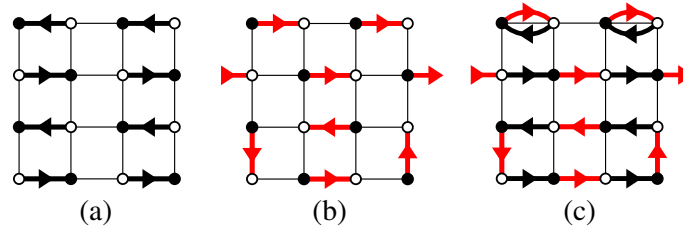


Figure 4.2: (a) Reference state used here for defining the winding number. The direction of the dimers is from sublattice B (open circle) to sublattice A (solid circle). (b) An arbitrary valence bond state, with dimers drawn in the opposite direction, from sublattice A to sublattice B. (c) The transition graph formed by the reference states in (a) and the arbitrary state in (b). The winding numbers correspond to the net fluxes (in units of the system length  $L$ ) defined by traversing the loops formed along the arrows; here  $\Phi_x = 1$  and  $\Phi_y = 0$ , or  $\Phi = (1, 0)$ , which corresponds to winding number  $W = (0, 1)$  in the definition of Fig. 4.1

prompted the term ‘‘Cantor deconfinement’’ for this class of unconventional transitions). This motivates us to also study the CDM and RVB states in different winding number sectors, which (it turns out) also happens to be an effective probe of the states’ topological natures. In the case of the RVB, states defined within sectors of different winding numbers are not orthogonal, but become orthogonal in the limit of the infinite lattice (which we will here demonstrate explicitly based on simulations).

### 4.1.3 Outline of the chapter

We refer readers to Sec. 2.1 for the essential features of the valence bond basis that we use for the RVB-state calculations and Monte-Carlo two-bond reconfigurations [53] and loop-cluster algorithms for sampling the CDM and RVB states.

The outline of the rest of the chapter is as follows: In Sec. 4.2 we present results for the standard case of only length-1 dimers and valence bonds, as well as extended models with bonds of length  $\sqrt{5}$ . In Sec. 4.3 the results are interpreted in terms of a height model. Detailed derivations of height model predictions are left to Appendix B. In Sec. 4.4 we further characterize the nature of the critical VBS fluctuations in terms of the joint

probability distribution of the order parameters for horizontal and vertical bond ordering. We conclude in Sec. 4.5 with a brief summary and discussion.

## 4.2 Results

The ground state of the QDM at the RK point is the equal amplitude superposition of classical dimer states. The CDM can therefore give some insights into properties of the RVB system as well, as long as the non-orthogonality of the valence-bond basis (i.e., the internal singlet structure of the valence bonds of the RVB) does not play an important role. [43] The quantitative validity of this approach is tested here by comparing the properties of the CDM and the short-bond RVB state. We present the definition of winding number and its distributions of both models in Sec. 4.2.1, then briefly discuss the standard spin correlation function of the RVB in Sec. 4.2.3. In Sec. 4.2.4 we study the four-spin VBS correlation function (4.1) of the RVB (which we also refer to as a dimer-dimer correlation function) and compare with analogous results for the well known dimer-dimer correlations of the CDM. In this section we consider the winding number sector  $W = (0, 0)$  and later, in Sec. 4.2.5, discuss also correlations in systems with nonzero winding number. In Sec. 4.2.6 we study the monomer distribution functions and in Sec. 4.2.7 systems including the longer bonds.

### 4.2.1 Sector probabilities

In this subsection, we will first introduce winding numbers and issues related to sampling them either grand-canonically (where there are some ergodicity issues in the case of the RVB) or canonically. We then present probabilities of winding number sectors in detail.

#### 4.2.1.1 Winding numbers

A two-bond update cannot bring the system from one topological winding number sector to another, while the loop update can. In the case of the RVB, there are winding numbers both for the bra and the ket state, and because of the non-orthogonality of the basis these

winding numbers can be different. We denote the full winding number of a configuration in this case as  $W = (W_x^\alpha, W_y^\alpha; W_x^\beta, W_y^\beta)$ . In a grand canonical ensemble of all winding numbers, the sectors have different weight, which can be computed using Monte Carlo sampling with the loop updates simply by keeping track of the number of configurations generated in each sector. Results for such weights are presented below in Sec. 4.2.2.

The loop algorithm for the CDM remains ergodic in the grand-canonical winding-number space even for very large systems, i.e., the loops can easily become very long and span the system. These long loops are related to deconfined monomers. [133] The RVB simulations, in the case of short-bond states, in practice become stuck in some fixed winding-number sector for large  $L$ . However, the shortness of the RVB loops does not imply monomer confinement, as these loops are not directly related to states with monomers. [133] The loops for short-bond two-dimensional RVB states are typically very short (rarely exceeding 12 bonds in the case of the length-1 bonds only). This results in rather large error bars for computed quantities for  $L \geq 50$ , seen in grand-canonical results to be discussed further below. In practice, for large systems we will therefore study canonical ensembles in different fixed winding number sectors. Starting with a configuration initially prepared with a desired winding number (such as those illustrated in Fig. 4.1), two-bond updates explicitly conserve the winding number while loop updates in practice do as well, for large systems within reasonable simulation times.

### 4.2.2 Probabilities results

We simulated the grand-canonical ensemble of winding numbers, as explained in Sec. 4.2.1.1, and accumulated the probabilities of several different sectors as shown in Fig. 4.3, for both the RVB and CDM, and for various system sizes  $L$ . The  $W = 0$  [(0,0) for the CDM and (0,0;0,0) for the RVB] sector is dominant in both cases, with the probabilities in the higher- $W$  sectors decreasing rapidly. The probabilities of these low- $W$  sectors clearly converge to  $L$ -independent non-zero constants, rapidly with  $L$  for the CDM, and also for the diagonal ( $W^\alpha = W^\beta$ ) sectors of the RVB (although the RVB data are much noisier

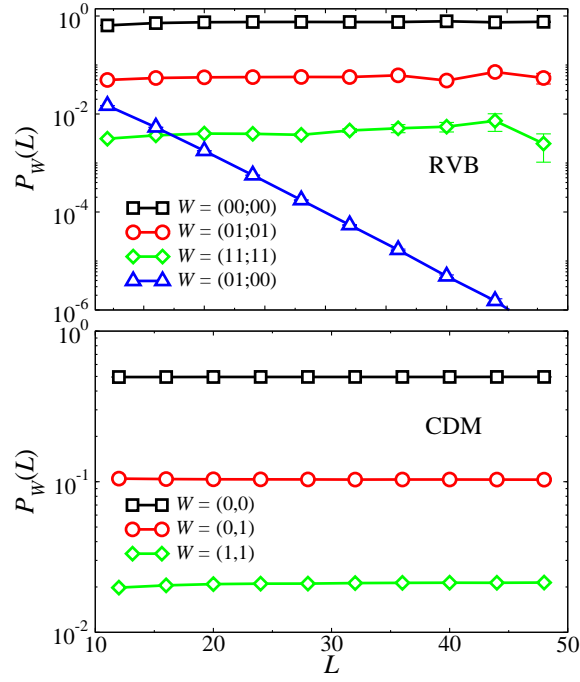


Figure 4.3: Winding number probabilities obtained in simulations with the loop algorithms for the RVB and CDM (with only the shortest bonds, as in Fig. 2.2). Results for several low- $W$  sectors of the CDM (lower panel) and RVB (upper panel) are shown versus the lattice size on a lin-log scale. In the RVB, the probability of the off-diagonal sector  $W = (0, 1; 0, 0)$  vanishes exponentially with  $L$ , reflecting the orthogonality (when  $L \rightarrow \infty$ ) of states in different winding number sectors.

for the large systems). By contrast, the probabilities of the off-diagonal sectors of the RVB, here exemplified by  $W = (0, 1; 0, 0)$ , decay exponentially to zero, which reflects the expectation that the states in different winding number sectors should become orthogonal in the thermodynamic limit. [114] In the following, when considering winding number sectors of the RVB we will focus on the diagonal sectors and for simplicity denote the total winding number by  $W = (W_x, W_y)$  in the same way as for the CDM.

### 4.2.3 Spin correlations in the RVB state

The spin-spin correlation function of the RVB has been studied before and is known to decay exponentially for a 2D system with short bonds (while a system with sufficiently slow

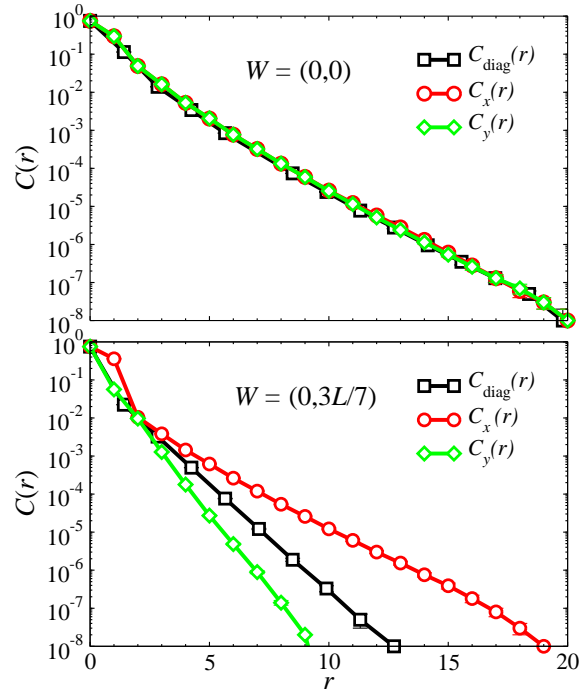


Figure 4.4: Spin correlations versus lattice distance  $r$  in the short-bond RVB in the sector of winding numbers  $W = (0,0)$  (top panel) and  $W = (0, 3L/7)$  (bottom panel) computed using  $L \times L$  lattices with  $L = 48$ . Results are shown for the separation  $(x, y)$  taken along the two axis,  $(r, 0)$ ,  $(0, r)$ , as well as on the diagonal,  $(r/\sqrt{2}, r/\sqrt{2})$ .

decay of the probability of long bonds has long-range antiferromagnetic order). [53, 134] Here, we only comment briefly on the role of the winding number. For unequal  $x$  and  $y$  winding numbers,  $W_x \neq W_y$ , the CDM and RVB systems clearly do not have the  $90^\circ$  rotational symmetry of the square lattice. We will investigate the directional dependence of the four-spin dimer-dimer correlations below. Here, in Fig. 4.4, we show results for the spin-spin correlations in two different winding number sectors. The correlations are always exponentially decaying with distance, with a faster decay in the same direction as the one in which a non-zero winding number is imposed.

#### 4.2.4 Dimer correlations

In the CDM, the dimer-dimer correlation function  $D_{xx}(\mathbf{r})$  is defined in the standard way using the bond occupation number  $n_x(i) = 0, 1$  on the link of the lattice between site  $i$  and its neighbor at distance  $(1, 0)$ ;  $D_{xx}(\mathbf{r}_{ij}) = \langle n_i n_j \rangle$ . The four-spin correlation function (4.1) of the RVB instead involves the loop estimator (2.15). This reduces to the CDM form for  $SU(N)$  spins when  $N \rightarrow \infty$  and the basis becomes orthogonal [in the representation of  $SU(N)$  in which the factor  $1/2$  in the off-diagonal matrix element in (A.3) and (A.4) is replaced by  $1/N$ ; [101] see, Ref. [135] for computations with such basis states]. For  $N = 2$ , considered here, significant differences between the RVB and CDM can be expected.

Since we are using periodic boundary conditions, the maximal separation to be used in the correlation function is  $(L/2, L/2)$  on a  $L \times L$  lattice. We first investigate the dominant part of the correlation function, which in the CDM is a mixture of a staggered component, at  $q = (\pi, \pi)$  in reciprocal space, and columnar correlations, at  $q = (\pi, 0)$  and at  $(0, \pi)$ . [119, 120] The asymptotic decay of these correlations can be accessed through the difference between the real-space correlations at two distances, e.g.,

$$D_{xx}^*(x, y) = D_{xx}(x, y) - D_{xx}(x - 1, y). \quad (4.4)$$

This quantity at the longest distance  $\mathbf{r} = (L/2, L/2)$  is graphed versus  $L$  in Fig. 4.5 for both the RVB and the CDM in several fixed winding number sectors.

For the CDM, the decay with  $L$  is consistent with the known  $\sim 1/r^2$  decay of the dominant correlations. Apart from an overall prefactor that depends on the winding number, there are only minor differences between the different winding sectors for small systems. The dependence of the results on the winding number is stronger for the RVB, but, as expected, also here the exponent  $\alpha$  in the power-law form  $1/r^\alpha$  becomes independent of  $W$  for large  $L$  (as long as the relative winding number  $W/L \rightarrow 0$  when  $L \rightarrow \infty$ ). Unlike the CDM, in this case the prefactor of the power-law form also converges as  $L \rightarrow \infty$ , i.e., the correction to the prefactor decays as some power higher than  $\alpha$ .

In Fig. 4.5, we also show results in the grand-canonical winding number ensemble, which,

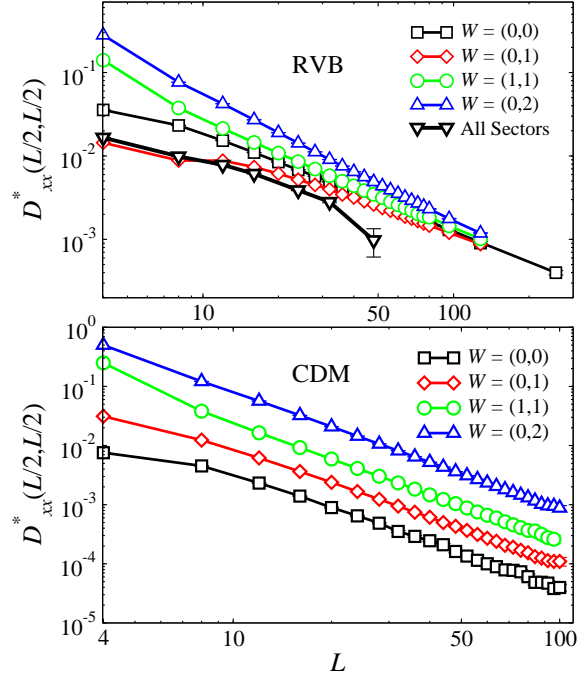


Figure 4.5: Dimer-dimer correlation function difference (4.4) at the maximal distance versus the lattice size. The upper panel shows results for the quantum RVB in different topological sectors as well as in the grand canonical ensemble (including all winding number sectors, in which case the fluctuations between sectors becomes very slow for large systems, as reflected in the large error bar for  $L = 48$ ). All correlations converge to the same power-law decay as system size increases. The power, based on the  $W = (0, 0)$  data for large  $L$ , is  $\alpha = 1.191(6)$ . The lower panel shows results for the CDM, which are consistent with  $\sim 1/r^2$  (shown with the solid line) for all winding number sectors.

as discussed in Sec. 4.2.1.1, suffers from problems with non-ergodic sampling for  $L \geq 50$  (reflected in the large error bar for  $L = 48$ ). For extracting the asymptotic form of the correlations, the  $W = (0,0)$  sector is the best choice and gives  $D(r) \propto 1/r^\alpha$  with  $\alpha = 1.191(6)$  for large systems. While the behavior is, thus, qualitatively similar to the CDM, the exponent differs considerably. The reduced value of the exponent can be interpreted as the RVB state being closer to an ordered VBS than might have been anticipated based on the known CDM dimer correlations.

There are two sources of differences between the correlations in the CDM and the RVB: the form of the estimator (2.15) as well as the weighting of the bra and ket valence bond states with the loop factor  $2^{n_{\alpha\beta}}$  for the RVB instead of the equal superposition of the individual bond configurations in the CDM. We have also measured the dimer correlations of the RVB in the same way as in the CDM, by just using the bond occupation numbers in the bra and the ket states (but with the correctly weighted sampling of the RVB). We find the same exponent  $\alpha \approx 1.20$  as above, which shows that the source of the different power-law is only the different weighting of the states. This could also have been anticipated based on the fact that the spin-spin correlation function of the RVB is exponentially decaying, which translates into short loops in the transition graph. [62, 63] The loop estimator (2.15) of the four-spin dimer correlation function is therefore still local and cannot change a power law.

The Fourier transform of the full dimer-dimer correlation function  $D_{xx}(\mathbf{r})$  is the structure factor  $S(\mathbf{q})$ . This quantity gives a more detailed picture of the long-distance behavior of the dominant correlations. Representative results for the  $S(\mathbf{q})$  for  $L = 32$  systems in three different winding number sectors  $(0, W_y)$  are shown in Fig. 4.6. In this section we focus on the  $W = (0, 0)$  sector and leave discussions of nonzero winding numbers to Sec. 4.2.5. The “bow-tie” feature seen for  $W = (0, 0)$  in the CDM is well known and understood based on the mapping of the system to a height model (see Appendix B). The system has two kinds of power-law correlations: an effectively dipolar kind, which is responsible for the “pinch-point” singularity at  $\mathbf{q} = (\pi, \pi)$  (see Appendix. B.3), and a “critical” kind with variable

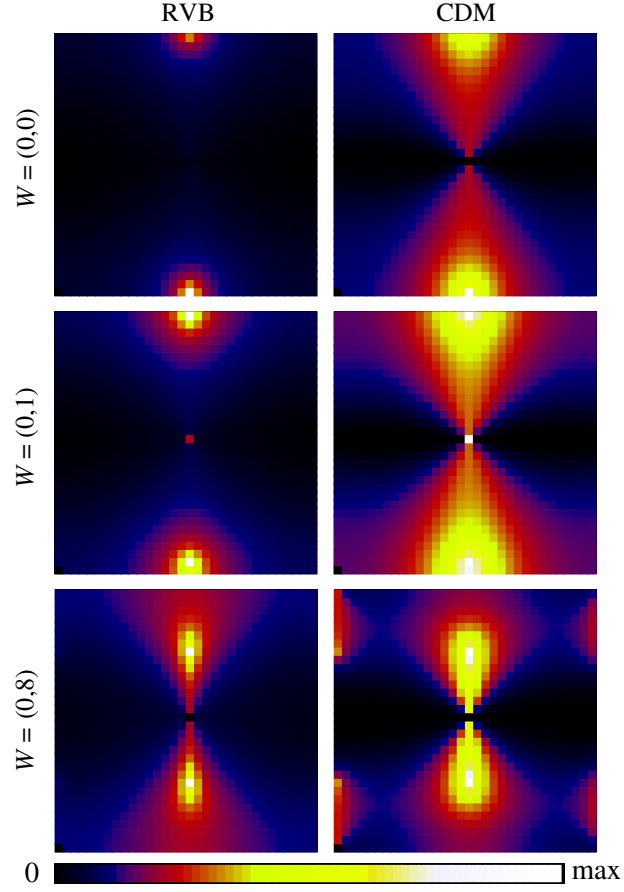


Figure 4.6: Fourier transform  $\mathbf{S}(\mathbf{q})$  of the dimer-dimer correlation function  $D_{xx}(\mathbf{r})$  for systems of size  $L = 32$ . The squares represent the full reciprocal space  $q_x, q_y \in [0, 2\pi]$ . Results in winding number sectors  $W = (0, 0)$ ,  $W = (0, 1)$ , and  $W = (0, 8)$  are shown for the RVB (left) and CDM (right). The location of the broad (“incommensurate”) peak in both cases is  $\mathbf{Q} = (\pi, 2\pi W_y/L)$ . The sharp peak at  $(\pi, \pi)$  is due to a nonzero average staggered dimer order induced by a nonzero winding number. This peak has been removed in the graphs  $W = (0, 8)$  in order to make the other features of the correlations better visible. The height of the peaks as a function of the system size is analyzed in Fig. 4.7.

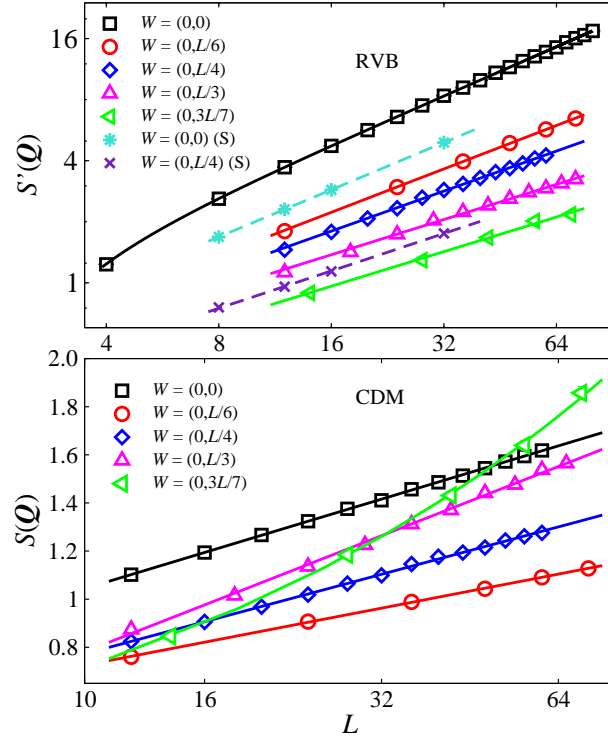


Figure 4.7: Peak values of the dimer structure factor, where  $\mathbf{Q} = (\pi, 2\pi W_y/L)$ , versus the system size in sectors with different winding  $W_y$ . The modified definition  $S'(\mathbf{Q})$  for the RVB is given in Eq.(4.5). Note the different  $y$ -axis scales used for the two models (logarithmic for the RVB and linear for the CDM). In the CDM (lower panel) the behavior is consistent with a log divergence (as shown with fitted lines) for small winding numbers, but for larger  $W$  it appears that the behavior is instead governed by a power law (which then may be the case for all  $W_x/L > 0$  for sufficiently large systems). The curve through the  $W = (0, 3L/7)$  data shows  $S(\mathbf{Q}) \propto L^{0.48}$ . In the RVB (upper panel) the exponent of the power-law divergence decreases slightly with increasing winding number. The legends with (S) correspond to the peak values of the full structure factor  $S(\mathbf{Q})$ .

exponents, which leads to a broad peak at  $\mathbf{Q} = (\pi, 0)$  diverging logarithmically with the system size, as shown in the lower panel of Fig. 4.7. In the RVB the peak is much sharper and diverges faster, as a power law (as shown in the upper panel of Fig. 4.7) on account of the real-space form  $1/r^\alpha$  with  $\alpha \approx 1.2 < 2$  of the dimer correlation function.

When the Fourier transform  $S(\mathbf{q})$  is computed post-simulation based on all computed real-space correlations, the measurements in the simulations are expensive, requiring  $\mathcal{O}(N^2)$  operations to take full advantage of spatial averaging. In the CDM, we can instead easily just compute  $S(\mathbf{Q})$  at the single wave-vector  $\mathbf{Q}$  directly in the simulations at a much lower cost of  $\mathcal{O}(N)$  to access larger system sizes. In the RVB, this speed-up is not possible, however, because we are there really measuring a four-spin correlation function that cannot be simply expressed as a product of two-spin correlators, as discussed in Appendix A, and there is no obvious way of avoiding the  $\mathcal{O}(N^2)$  scaling of this measurement.

In order to have a similar quantity, which scales with the system size in the same way as  $S(\mathbf{Q})$  but for which the measurements require only  $\mathcal{O}(N)$  operations, we define a modified structure factor  $S'(\mathbf{Q})$  for the RVB as

$$S'(\mathbf{Q}) = \langle \tilde{B}_x^*(\mathbf{Q}) \tilde{B}_x(\mathbf{Q}) \rangle \quad (4.5)$$

where  $\tilde{B}_x(\mathbf{Q})$  is the Fourier transform of the spin-spin correlator matrix element  $\langle V_\beta | (\mathbf{S}_i \cdot \mathbf{S}_j) | V_\alpha \rangle$  for an individual configuration in the RVB simulation (i.e., obtained from a transition graph, which gives values  $\in \{-3/4, 0\}$  for each nearest-neighbor bond on the lattice). This definition of the peak value differs from the full Fourier transform  $S(\mathbf{Q})$  of the four-spin dimer correlator  $D(r)$ , essentially because it does not contain any information on the order of the site indices in the matrix element  $\langle V_\beta | (\mathbf{S}_k \cdot \mathbf{S}_l)(\mathbf{S}_i \cdot \mathbf{S}_j) | V_\alpha \rangle$ , which plays a role in the transition-graph two-loop estimator of the dimer correlation function (as discussed in Appendix A). In particular, the modified quantity misses certain negative contributions arising in some cases where all four indices belong to the same loop [see Eq. (2.15)]. Therefore, we expect  $S'(\mathbf{Q}) > S(\mathbf{Q})$ , which is also confirmed by results for both quantities in small systems, as shown in the upper panel of Fig. 4.7. The form of the power-law divergence is

the same, however.

Overall, there is significant directional dependence in the dimer correlations, but for  $W = (0, 0)$  the RVB results in Fig. 4.7 confirm that the peak at  $(\pi, 0)$  (corresponding to columnar-modulated correlations) is sufficiently isotropic for the size dependence of the Fourier peak to be directly related to the exponent of the power-law decay  $1/r^\alpha$  found above for the real space correlation (and, it should be pointed out, the exponent  $\alpha$  also comes out consistently to the same value when extracted in different directions in real space).

With  $S'(\mathbf{Q})$  diverging with the system size  $L$  as  $L^{\alpha_Q}$ , we expect  $\alpha_Q \approx 2 - \alpha$  and the data confirm this. For instance, the  $W = (0, 0)$  data in the upper panel of Fig. 4.7 was fitted to a function  $f(x) = b_Q x^{\alpha_Q} + b_2 x^{\alpha_2}$  (where typically  $\alpha_2 < 0$  and this correction term is added in order to include data for the full range of system sizes) with four fitting parameters and we found  $\alpha_Q = 0.800(2)$  in good agreement with  $\alpha = 1.191(6)$  but with a smaller error bar. Our best estimate for the exponent is, thus,  $\alpha = 1.200(2)$ . Here the error bar is purely statistical and there may still be some systematical errors present as well (likely of the same order), arising from neglected higher-order corrections.

#### 4.2.5 Correlations with nonzero winding number

In a background of nonzero winding number, all dimer-dimer correlations should become modulated by the factor  $\cos(\delta\mathbf{Q} \cdot \mathbf{r})$ , as derived using the height-model formalism in Appendix B and shown explicitly as Eq. (B.16), where  $\delta\mathbf{Q} = 2\pi(W_x, W_y)/L$ . Such a modulation is visible in the real-space dimer correlation function, as shown in Fig. 4.8 for  $D_{xx}^*(\mathbf{r})$  along the diagonal lattice direction,  $\mathbf{r} = (x, x)$ , for systems of different size with winding number  $W = (0, 2)$ . This implies that when  $\mathbf{r}$  is followed along the  $[1, \pm 1]$  direction through an entire period,  $2(W_x \pm W_y)$  nodes of  $D_{xx}(\mathbf{r})$  are crossed; indeed, Fig. 4.8 for  $W = (0, 2)$  shows two changes of sign between  $x = 0$  and  $L/2$ , in both the CDM and the RVB cases.

The correlation function  $D_{xx}(x, y)$  in the full 2D space is shown for the RVB in Fig. 4.9, where an overall background constant representing  $D(r \rightarrow \infty)$  has been subtracted from  $D(\mathbf{r})$  and the remainder has been multiplied by  $r^\alpha$  to make the modulations visible. An

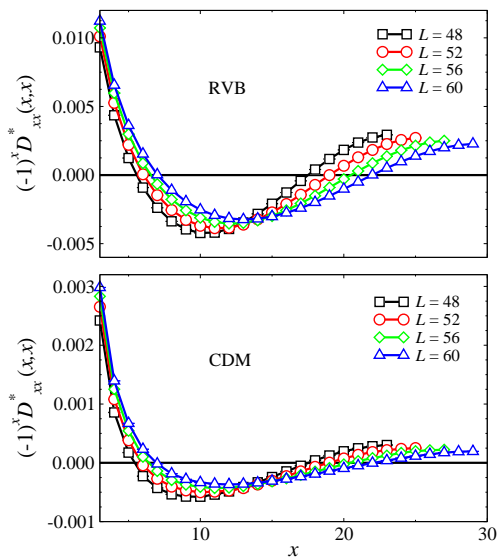


Figure 4.8: Dimer correlation differences versus  $x$  [where the separation  $\mathbf{r} = (x, x)$ ] along the diagonal lattice direction for systems of different size. The winding number is  $W = (0, 2)$ , and therefore two phase shifts are seen (corresponding to a total of four domains). Note that the overall magnitude of these correlations is much larger in the RVB (upper panel) than in the CDM (lower panel).

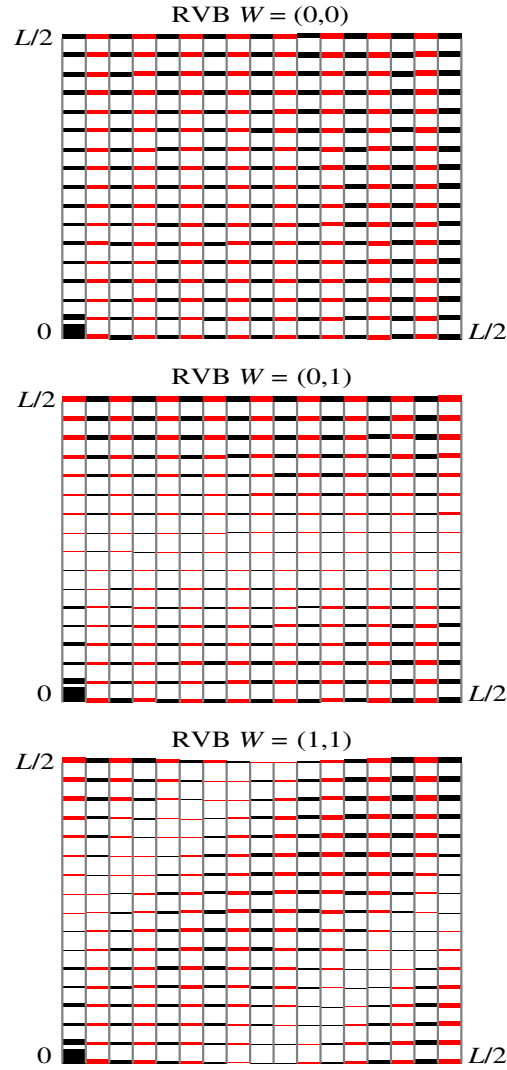


Figure 4.9: Correlation patterns obtained from the dimer correlator  $D_{xx}(x, y)$  by subtracting a constant and dividing the result by the leading power-law form  $r^{-\alpha}$  (with  $\alpha = 1.2$  for the RVB and  $\alpha = 2$  for the CDM). The  $(\pi, \pi)$  contribution was also removed for the  $W \neq 0$  sectors (by going to Fourier space as in Fig. 4.6). Black and red (gray) bars represent positive and negative values (i.e., stronger and weaker dimer correlations), respectively. In the  $W = (0, 0)$  sector, a dominant columnar pattern is visible, while in the  $W = (0, 1)$  sector the correlations shift from weak-strong weak-strong to strong-weak strong-weak over a window of distances  $\propto L$ , corresponding to two nodal lines as stated in text. The origin is at lower left corner, and one quadrant ( $L/2 \times L/2$ ) is shown of the possible separations. In the  $W = (1, 1)$  sector, correlations shift twice in a row, corresponding to the presence of two pairs of nodal lines.

over-all non-decaying staggered contribution present when  $W \neq 0$  has also been subtracted (see further discussion of this below and in Fig. 4.6). The color coding shows positive and negative correlations, and the width of bars represent the magnitude of the correlations. In the winding number  $W = (0, 0)$  sector, the positive and negative values alternate in rows, showing that the overall dominant correlations are of columnar type. In the  $W = (0, 1)$  sector, a phase shift occurring around at  $y = L/2$  is clear. The region over which the shift takes place is itself of size  $\mathcal{O}(L)$ , as expected since the amplitude is modulated proportional to a sine wave (which can be considered as a highly fluctuating critical delocalized domain wall). The results for the  $W = (1, 1)$  sector confirm the existence of two such delocalized nodes along the diagonal direction. A similar pattern of phase shifts in the correlation function is seen in the CDM case as well, but is much weaker because of the significantly faster decaying correlations (as is also clear in Fig. 4.8).

To our knowledge, these correlations in sectors of fixed non-zero winding number have not been studied in detail previously (but were pointed out also in the parallel work by Albuquerque and Alet [46]). In Appendix B, we extend the height-model approach to this case as well (in Sec. B.7). Here we only briefly discuss some of the main features, with the aim of comparing the RVB and CDM systems.

Turning back to the Fourier space plot, Fig. 4.6, it includes representative results for the structure factor in three different winding number sectors  $(0, W_y)$ . Once the winding number is non-zero, it is clear that there is, for both models, a  $\delta$ -function peak in  $S(\mathbf{q})$  at  $(\pi, \pi)$ , reflecting a non-zero static staggered order parameter. Since this peak grows in proportion to the winding number, we have subtracted it off in some cases in Fig. 4.6 to make the other features better visible.

There are two notable features of these results, for both the RVB and CDM: (i) the pinch-point remains at  $(\pi, \pi)$  and (ii) the singularity at  $(\pi, 0)$  present for  $W_y = 0$  is offset to  $\mathbf{Q} = (\pi, 2\pi W_y/L)$ , which when  $L \rightarrow \infty$  can be considered as an incommensurate peak at  $\mathbf{Q} \equiv (\pi, w)$ ,  $w \in [0, \pi]$ . This is exactly as expected from Eq. (B.17) obtained within the height-model representation in Appendix B. Figure 4.7 shows the system size dependence

of the singular peak for different *large* winding numbers  $W_y \propto L$ . These features have been qualitatively expected in the case of the CDM based on several previous works [132, 136, 137] (as outlined in Appendix B), but they are still interesting to study quantitatively and to elucidate the similarities and differences between the CDM and RVB. It is already clear from Fig. 4.6 that the divergence of the incommensurate peaks is much stronger for the RVB than the CDM, which is anticipated based on our result for the slow real-space decay of the dimer-dimer correlations in the RVB.

For non-zero winding number, the correlations become significantly anisotropic, but we have not attempted to study their full functional form in real space or Fourier space. The exponent governing the asymptotic power-law decay is, however, expected to be direction independent, as discussed in Appendix B. The results in Fig. 4.7 indicate that  $S(\mathbf{Q})$  has the form  $L^{\alpha_Q}$ , with a weak dependence of the exponent  $\alpha_Q$  on the location of the peak (i.e., the winding number), also as expected based on the height-model results in Appendix B.8.

The incommensurate peak of the CDM was discussed by Fradkin et al., [132] who pointed out a set of critical points in extended QDMs with more complicated diagonal and off-diagonal terms than the standard RK nearest-neighbor bond-pair interactions. The critical points extend from the conventional RK point at zero winding number, forming a complex fractal curve with devil's staircase features (forming a Cantor set). This critical curve separates a staggered dimer phase from one with a complex bond pattern with a large unit cell, which depends on the winding number. Similar transitions with a series of different VBS phases were studied in Ref. [131]. Our CDM results in Fig. 4.7 for large winding numbers suggest that the incommensurate peak may become power-law divergent (i.e., stronger than the logarithmic divergence obtaining at zero winding number). This is seen most clearly in the  $W = (0, 3L/7)$  graph, where it is clear that the divergence with  $L$  is faster than logarithmic. A power-law fit,  $L^{\alpha_Q}$  with  $\alpha_Q = 0.48(3)$  describes the data well. This is expected in the height scenario, since a nonzero background  $W/L$  changes the effective stiffness to  $K'$  as given by (B.25). The exponent  $\alpha$  of real-space correlations accordingly changes from 2 and consequently the integral of  $1/r^\alpha$  (the structure factor) should diverge

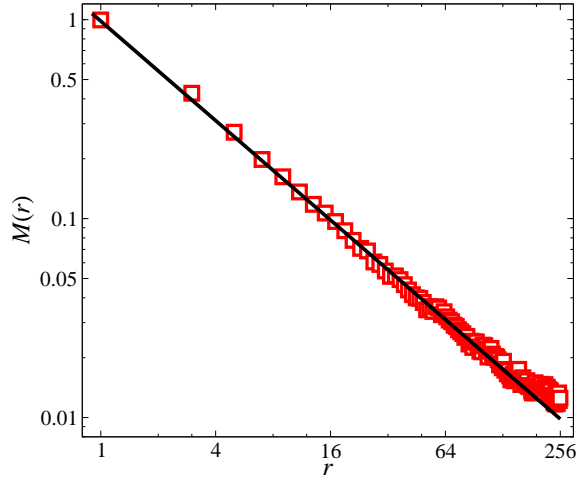


Figure 4.10: Monomer distribution function in the RVB state on an  $L = 512$  lattice. The straight line is a fit to the power-law form  $1/r^\beta$  with  $\beta = 0.830(9)$ .

faster than logarithmically.

#### 4.2.6 Monomer distribution

Monomers are expected to be deconfined in RVB states, [2] which provides an intuitive picture of spin-charge separation. Here we will study two monomers in the RVB. It should be noted, however, that these monomers are bosonic, and hence the results cannot be directly related to a hole-doped RVB spin liquid. In that case the monomers should be fermions and, as discussed, e.g., in Ref. [67], the sign rule we use here for the valence bonds would have to be replaced by more complex signs. It is nevertheless interesting to compare the monomer-doped RVB and CDM systems considered as different statistical mechanical systems.

The monomer-monomer distribution function of the CDM is defined using the monomer density  $m(\mathbf{r}_i) = 0, 1$ ;

$$M(\mathbf{r}_{ij}) = \frac{\langle m(\mathbf{r}_i)m(\mathbf{r}_j) \rangle}{\langle m(\mathbf{r}_i)m(\mathbf{r}_i + \hat{\mathbf{x}}) \rangle}, \quad \mathbf{r}_{ij} = \mathbf{r}_i - \mathbf{r}_j, \quad (4.6)$$

where the normalization with the correlation at distance  $r = 1$  is a convention which makes it easy to compare results for different system sizes (i.e., results for fixed  $r$  converge

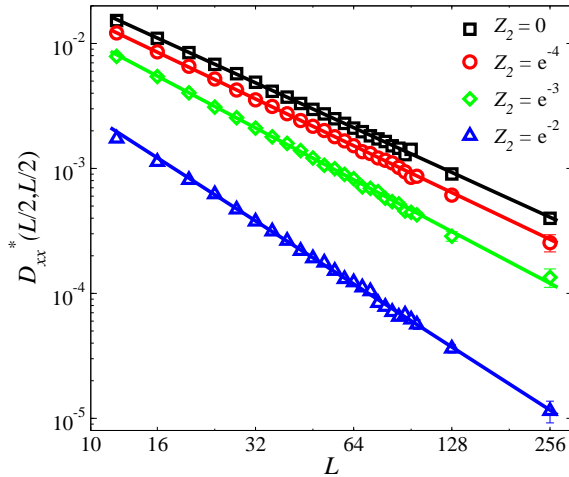


Figure 4.11: Dimer-dimer correlation function difference  $D_{xx}(r)$  for RVB systems in the  $W = (0, 0)$  sector with different fugacities  $Z_2$  of long (fourth-neighbor) bonds (with the short-bond fugacity  $Z_1 = 1$ ). The decay exponents grows with the long-bond fugacity. The values are given in Table 4.1.

to a non-zero number with increasing size, even if the monomers are deconfined). It is known [119, 120] that this function for the short-bond CDM decays as  $M(r) \propto 1/r^\beta$  with  $\beta = 1/2$ . This slow decay reflects monomer deconfinement, i.e., the function  $\langle m(\mathbf{r}_i)m(\mathbf{r}_j) \rangle$  without the normalization in (4.6) decays to zero for fixed  $\mathbf{r}_{ij}$  when  $K \rightarrow \infty$ . We use exactly the same definition of  $M(\mathbf{r})$  for the RVB, applying the procedures discussed in Sec. 2.1 to sample monomer configurations (while in the CDM the loop algorithm for the bond sampling without monomers gives the monomer distribution function as a by-product [65, 66]). Note that the winding number is not well defined in the presence of monomers, since they are associated with “broken loops” in the transition graph in Fig. 4.2.

The exponent  $\beta = 1/2$  for the CDM has been confirmed previously in Monte Carlo simulations on large lattices. [66] Figure 4.10 shows our results for the RVB, using a system of size  $L = 512$  (for which the results for moderate separation of the monomer are sufficiently converged to extract the decay exponent). We find that the exponent  $\beta \approx 0.83$  is significantly larger than in the CDM. The monomers are, thus, more strongly correlated to each other than in the CDM, but still deconfined. Note that in a long-range ordered VBS

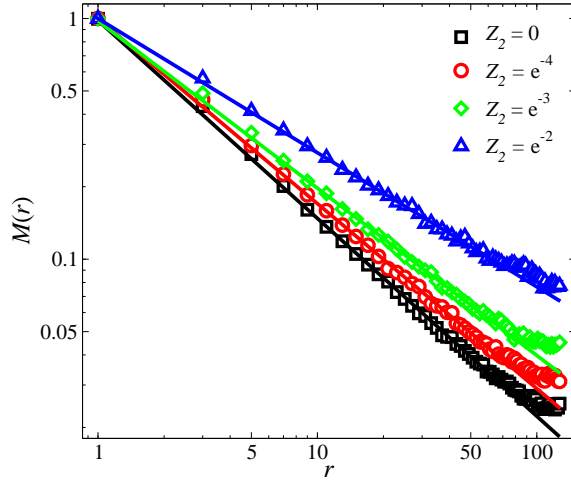


Figure 4.12: Monomer distribution function  $M(r)$  for RVB states with a small fraction of fourth-neighbor bonds on a lattice of size  $L = 256$ . The straight lines are fits giving deconfinement exponents which decrease with increasing long-bond fugacity. The exponents are listed in Table 4.1.

one would expect the monomers to be confined.

#### 4.2.7 Including longer bonds

As the next step after investigating the extreme short-bond RVB, it is natural to think about the role of the longer bond in spin liquids and the classical dimer model. In the case of the CDM, introducing bonds between next-nearest neighbors on the square lattice leads to exponentially decaying dimer correlations and monomer confinement, [66] as on a triangular lattice with only nearest-neighbor bonds. [121] However, with only bipartite bonds, the behavior is qualitatively similar to the short-bond model (as long as the fugacity for longer bonds decays sufficiently rapidly with the length of the bonds). [66] The dimer correlations decay as  $1/r^\alpha$  with  $\alpha = 2$  not changing as longer bonds are introduced, but the monomer exponent  $\alpha$  decreases from  $1/2$ .

In the RVB, Marshall's sign rule cannot be applied if non-bipartite (frustrated) bonds are introduced. Due to the non-orthogonality of the basis, there is, regardless of how signs beyond some simple Marshall rule are introduced, a sign problem in the Monte Carlo bonds

Table 4.1: Dimer-dimer and monomer exponents obtained for the CDM and RVB systems at different fugacities  $Z_2$  for the next-shortest bonds (of length  $\sqrt{5}$ ).

Model	$Z_2$	$\alpha$	$\beta$
CDM	0	1.98(1)	0.4996(5)
CDM	$e^{-4}$	2.17(2)	0.447(2)
CDM	$e^{-3}$	2.44(8)	0.392(1)
CDM	$e^{-2}$	2.7(2)	0.302(1)
RVB	0	1.191(6)	0.830(9)
RVB	$e^{-4}$	1.255(5)	0.775(5)
RVB	$e^{-3}$	1.377(10)	0.707(5)
RVB	$e^{-2}$	1.676(12)	0.563(6)

sampling (due to non-positive definiteness of the state overlaps). We here study the effects of bipartite valence bonds connecting fourth-nearest neighbors, i.e., of “shape”  $(x, y) = (2, 1)$  and all symmetry-related shapes, as was done previously for the CDM. [66] We use small fugacities  $Z_2 = e^{-2}$ ,  $Z_2 = e^{-3}$  and  $Z_2 = e^{-4}$  for the longer dimers and  $Z_1 = 1$  for the short bond connecting nearest neighbors. In the RVB, since we work with the amplitude product states [Eq. (2.4)], we just use the “fugacities” as another notation for the RVB amplitudes;  $h(r = 1) = Z_1 = 1$ ,  $h(r = \sqrt{5}) = Z_2$ .

Spin correlations have been previously studied in the presence of long bonds, including exponential and power-law decays of the length-dependent fugacities. [53,134] Here we again focus on the dimer-dimer correlations and monomer distribution function.

The exponent of the dimer-dimer correlations changes with the fugacity of long bonds, as shown in Fig. 4.11 and Table 4.1. The change can be seen even more obviously in higher winding number sectors (not shown in the figure). Note also that the spin correlations increase when longer bond are introduced. [53,134] Fig. 4.12 shows the monomer distribution  $M(r)$  as defined in Eq. (4.6). Similar to the CDM, [66] the confinement exponent changes with fugacity of long bonds. The higher the fugacity of long bonds, the lower is the monomer deconfinement exponent.

### 4.3 Height model interpretation

All of the numerical results found in these simulations can be compared with results obtained in the framework of the “height model” introduced in Sec. 4.1.2 and elaborated in appendix B. According to that description, each of the following can be written as a function of a single parameter, the height stiffness  $K$ :

- (1) The sector probabilities  $P(W_x, W_y)$  presented in Fig. 4.3.
- (2) The exponent  $\alpha$  of critical dimer correlations, inferred from the  $L$ -dependence of the structure factor at  $\mathbf{Q} = (\pi, 0)$  [the peak-value at winding number  $W = (0, 0)$  as shown in Fig. 4.7], and also from the  $L$  dependence of these same correlations at  $\mathbf{r} = (L/2, L/2)$  in real space, as plotted in Fig. 4.5.
- (3) The decay exponent  $\beta$  of the monomer distribution function  $M(r)$  as presented in Fig. 4.10.
- (4) The coefficient of the “pinch-point” singularity in the structure factor  $S(\mathbf{q})$  as shown in Fig. 4.6.

We can use these relations to reduce the different results to independent estimates of the stiffness, which we call  $K_P$ ,  $K_\alpha$ ,  $K_\beta$ , and  $K_S$ , from these respective measurements. The agreement (to be demonstrated below) of these is powerful evidence that a height-like field theory underlies the RVB state. That is well-known to be true for the CDM state, but the extension to the RVB is non-trivial, due to the configuration space here consisting of two bond configurations weighted by their transition-graph loops, as discussed in Sec. 2.1. Indeed, we have not derived the height-model representation explicitly for the RVB. We will make some comments on the feasibility of actually deriving the effective model below.

#### 4.3.1 Four ways to extract stiffness

We now run through the ways in which we get four independent measurements of the height stiffness  $K$ . CDM results are presented in parallel to the RVB results, firstly to check the

Table 4.2: Stiffness parameter  $K_P$  in the infinite CDM and RVB systems inferred from the winding-number sector probabilities (from data in Fig. 4.3) according to Eq. (4.7).

$(W_x, W_y)$	CDM		RVB	
	$P(W_x, W_y)$	$K_P$	$P(W_x, W_y)$	$K_P$
(0,0)	0.49625(4)	—	0.764(5)	—
(1,0)	0.10321(3)	0.19628(3)	0.057(2)	0.325(5)
(1,1)	0.02146(1)	0.19629(3)	0.0043(5)	0.324(7)
(2,0)	0.000925(2)	0.19642(8)	—	—

systematic errors in our fitting procedures against exactly known results, and secondly to emphasize the similar behaviors.

#### 4.3.1.1 Sector probabilities

Table 4.2 gathers together the numerical sector probabilities from the data sets in Fig. 4.3. As seen in the figure, the smaller sizes show noticeable finite- $L$  corrections, which are expected to be  $O(1/L^2)$  due to the quartic correction (B.19) to the free energy density. The larger sizes show larger statistical errors particularly for the RVB case, as explained in Sec. 4.2.1.1. In order to partially account for finite- $L$  corrections of leading order and higher, which we need to extract the probabilities at  $L \rightarrow \infty$  with relatively smaller statistical fluctuations by using a large set of lattice sizes, we use suitable polynomial fitting functions (some times without linear term) to extrapolate values in the thermodynamic limit.

According to Eq. (B.15), we expect  $P(W_x, W_y) \propto \exp[-8K(W_x^2 + W_y^2)]$ , and thus, we define

$$K_P \equiv -\frac{\ln[P(W_x, W_y)/P(0, 0)]}{8(W_x^2 + W_y^2)}. \quad (4.7)$$

This expression clearly gives consistent results for every pair  $(W_x, W_y)$ , for either model as shown in Table 4.2. The  $K_P$  values in this table are calculated directly from the corresponding sector probabilities presented next to them. The  $K_P$  values included in Table 4.3 are taken from the  $W = (0, 1)$  sector, as that has the smallest error bars (and also should be the best in terms of originating from a weak “tilt” field). As indicated by Fig. 4.13, the  $K_P$

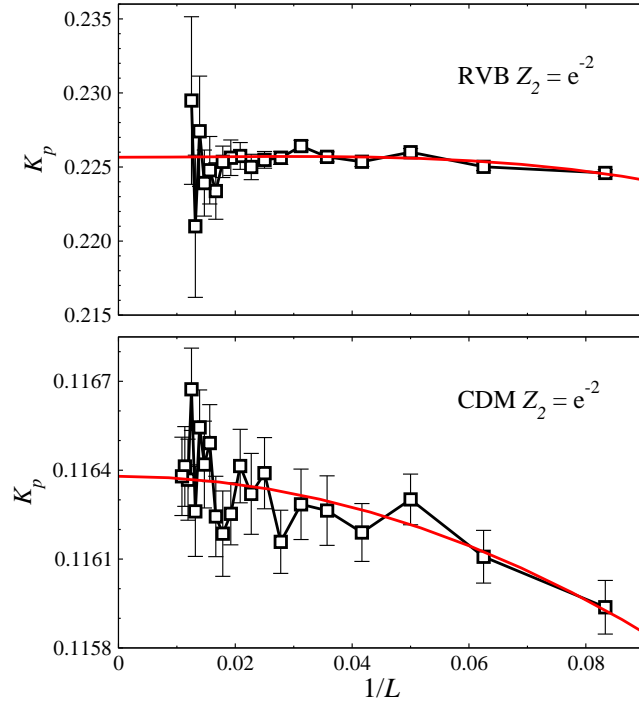


Figure 4.13:  $K_P$  value calculated in the  $W = (0, 1)$  sector according to Eq. (4.7) for systems with fugacity  $Z_2 = e^{-2}$  for long bonds and different lattice sizes. RVB and CDM results are shown in the upper and lower panel, respectively, as a function of the inverse system size  $1/L$ . The curves are second-order polynomial fits, not including the linear term.

value does not depend much on system size  $L$  for  $L$  larger than  $\approx 50$ . Therefore, in order to obtain smaller statistical errors, we presented  $K_P$  in Table 4.3 with the same method described above for extrapolating winding sector probabilities in the thermodynamic limit. As an example, polynomial fitting functions are shown in Fig. 4.13.

#### 4.3.1.2 Critical dimer correlations

We have [Eq. (B.8) in Appendix B.4] that  $\alpha = \pi/8K$ ; hence we define

$$K_\alpha \equiv \frac{\pi}{8\alpha}. \quad (4.8)$$

The values of  $\alpha$  summarized in Table 4.1 could in principle all be obtained by fitting the size dependence of the peak-value  $S(\mathbf{Q})$  of the dimer structure factor, i.e., according to the peak-height analysis illustrated in Fig. 4.7 in the case of the RVBs. However, this approach

Table 4.3: Stiffness estimates obtained from the four kinds of measurements discussed in the text;  $Z_2$  is the fugacity for dimers of length  $\sqrt{5}$ .

Model	$Z_2$	$K_P$	$K_\alpha$	$K_\beta$	$K_S$
CDM	0	0.19628(4)	0.198(1)	0.1962(2)	0.1959(7)
CDM	$e^{-4}$	0.17547(4)	0.182(2)	0.1755(8)	0.1794(3)
CDM	$e^{-3}$	0.15065(6)	0.161(5)	0.1539(4)	0.1582(4)
CDM	$e^{-2}$	0.11638(3)	0.14(1)	0.1186(4)	0.1234(1)
RVB	0	0.323(5)	0.330(2)	0.326(4)	0.3242(4)
RVB	$e^{-4}$	0.3067(8)	0.313(1)	0.304(2)	0.3081(2)
RVB	$e^{-3}$	0.2774(5)	0.285(2)	0.278(2)	0.277(1)
RVB	$e^{-2}$	0.2258(1)	0.234(2)	0.221(2)	0.22619(2)

requires a very significant computational effort for large lattices. We therefore use an easier but still reasonably accurate way to extract  $\alpha$ , by fitting the real-space long-distance dimer correlator  $D_{xx}^*(L/2, L/2)$  as in Fig. 4.11 by a power-law [as expected according to Eq. (B.7)]. For non-zero  $Z_2$  cases in the CDM, this approach does not work well, however, because  $\alpha$  increases with the fugacity, becoming larger than 2, and therefore the critical term is overshadowed by the stronger dipolar term (which always decays as  $1/r^2$ ; see Sec. B.4) and is hard to detect. In contrast, in the RVB  $\alpha < 2$  always and the critical term is dominant. A better way to find  $\alpha$  in the CDM is to extract values by a fit of  $|D_{xx}^*(x, x)|$  (along the diagonal axis) for a range of distances  $x$  on a large lattice, since the dipolar term vanishes on this axis. The corresponding  $K_\alpha$  values are listed in Table 4.3.

#### 4.3.1.3 Monomer pair distribution correlations

We have [Eq. (B.11) in Appendix B.5] that  $\beta = 8K/\pi$ ; hence we define

$$K_\beta \equiv \frac{\pi\beta}{8}. \quad (4.9)$$

This quantity extracted from the exponents listed in Table 4.1, where the values originate from fits to the  $r$ -dependence of the monomer distribution function (Fig. 4.12 in the case of the RVBs), is listed in Table 4.3.

#### 4.3.1.4 Coefficient of the pinch-point in $S(\mathbf{q})$

At  $\mathbf{Q} = (\pi, \pi)$ , there is a pinch-point singularity of the dimer structure factor for  $x$ -oriented dimers,  $S(\mathbf{q})$ , meaning that there is no divergence, but the limiting value at  $\mathbf{Q}$  depends on the direction of the ray along which it is approached. The coefficient of this  $k_y^2/(k_x^2 + k_y^2)$  singularity is  $1/K$  according to Eq. (B.5), so we can do a simple fit and call the result  $K_S$ . Of course, the actual dependence on  $\mathbf{q} = \mathbf{Q} + \mathbf{k}$  must have additions of higher order in  $\mathbf{k}$ , since  $S(\mathbf{q})$  is periodic in the Brillouin zone. Therefore, only a small domain around  $\mathbf{Q}$  should be used in the fit, but it may be advantageous to use more than the wave-vectors immediately adjacent to  $\mathbf{Q}$ , as one can then extrapolate to  $\mathbf{Q}$  and eliminate most of the unwanted additions. Of the four methods, this one is closest to direct measurement of the height Fourier spectrum  $\langle |\tilde{h}(\mathbf{k})|^2 \rangle$ , which was the best method to extract stiffness constants from simulations of height models [136, 138] or random-tiling quasicrystals [139, 140].

In the RVB case, some additional steps are necessary, because we do not construct a height function and do not really even have a dimer configuration (recall that the contributions to the wave function from different dimer configurations are non-orthogonal and the simulations sample pairs of dimer configurations). We only have the correlations  $D_{xx}$  of an operator that has some projection onto a dimer-like variable as well as other contributions. This has two consequences for  $S(\mathbf{q})$ . The first is that the “other contributions” contribute a constant background on top of the pinch-point singularity, which does not vanish even along the line  $k_y = 0$ . That can in principle be remedied by fitting and subtracting off the constant addition, but unless the lattice is very large such a procedure will not be perfect. In our fits carried out here, we simply use the value of the point that is next to the pinch point along line  $k_y = 0$  as our constant addition.

The second consequence of the lack of a formal height model is that the measured  $S(\mathbf{q})$  is a multiple of the assumed dimer structure factor by an unknown coefficient  $c_S^2$ . Fortunately, we can calibrate  $c_S^2$  using the sectors with nonzero winding numbers, since the  $\delta$ -function peak at  $\mathbf{Q}$  in those cases (after subtracting the constant background) is proportional to  $c_S^2$  times  $(W_x^2 + W_y^2)$  times known constants, allowing us to infer  $c_S^2 \approx 0.56$ . From this value

we can extract a normalized  $S(\mathbf{q})$  and, finally, find the pinch-point coefficient we call  $1/K_S$ . This estimate of  $K_S$  was computed for several system sizes and then extrapolated to  $L = \infty$  by fitting functions  $f(L) = a_0 + a_1/L^2 + a_2/L^3$  for the RVB and  $f(L) = a_0 + a_1/L^2$  for the CDM (i.e., with both forms not including the linear term). The results are given in Table 4.3.

### 4.3.2 Summary of the stiffness estimates

Table 4.3 collects all four estimates of  $K$ , with their statistical errors (one standard deviation). The fugacity  $Z_2$  for long dimers specifies a family of RVB models and one of CDM models, with different exponents. Note that  $K$  according to our convention is  $\pi/8$  times  $K$  as used previously in Ref. [66].

The respective estimates for the stiffness constant for a given case typically agree to within a few error bars. In some cases the deviations are larger than expected purely based on statistics. This is not unexpected, since the correlation functions we have analyzed are also affected by corrections to the leading forms we have used. Note that  $K_S$  for the CDM with long dimers are systematically too large (the only really significant disagreement); and  $K_S$  for the RVB with long dimers appears to be slightly too large as well. Here the background contributions which may not be perfectly subtracted off in our procedure, may be to blame.

The results for the CDM can be compared with the exact value  $K_{\text{CDM}} \equiv \pi/16 \approx 0.19635$ , with which all  $K$  estimates in Table 4.3 agree to within 2 error bars or less. As another test, we calculated  $K_P$  for the CDM with long bonds only (i.e., fugacities  $Z_2 = 1$  and  $Z_1 = 0$ ). The resulting value implies an exponent for the monomer correlations of  $\beta = 0.11092(6)$ , which agrees (within 1.5 error bars) with a previous obtained using a different analysis of the monomer distribution function (and where it was conjectured that  $\beta = 1/9$ ). [66]

The good agreement between four different stiffness estimates provides strong evidence of an underlying height model description of the RVBs. The plausibility of the height-model approach for the RVB is partially motivated by the fact that the RVB and CDM coincide

for  $SU(N)$  spins when  $N \rightarrow \infty$ . [101] One can then think of corrections to the continuum version of the height model for the CDM in terms of an  $1/N$  expansion (which we have not carried out). The results discussed here show that the  $1/N$  corrections all the way down to  $N = 2$  only correspond to a renormalization of the stiffness constant.

## 4.4 Order-parameter distribution

A columnar long-range ordered VBS on the square lattice breaks the translational and rotational lattice symmetries. As we have seen in the previous sections, the RVB is a critical VBS with a rather slowly decaying dimer-dimer correlation function. This correlation function, Eq. (4.1), measures the magnitude of the VBS order parameter. In this section we look at another aspect of these critical VBS correlations, probing the individual order parameters for columns forming with  $x$  and  $y$  orientation of the modulated bonds, defined as

$$\begin{aligned} D_x &= \sum_{x=1}^L (-1)^x \sum_{y=1}^L [\mathbf{S}(x, y) \cdot \mathbf{S}(x+1, y)]_{\text{conf}}, \\ D_y &= \sum_{y=1}^L (-1)^y \sum_{x=1}^L [\mathbf{S}(x, y) \cdot \mathbf{S}(x, y+1)]_{\text{conf}}, \end{aligned} \quad (4.10)$$

where  $[\dots]_{\text{conf}}$  indicates that these correlators are evaluated for an individual configuration (i.e., in the RVB they are matrix elements between the sampled bra and ket states). The expectation values of these order parameters vanish. In the CDM, the dimer-dimer correlation functions that we investigated before correspond to their squares, i.e., the dominant structure factor in reciprocal space (as seen in Fig. 4.6) is  $S(\pi, 0) = \langle D_x^2 \rangle / N$ , and the behavior of this quantity as a function of the system size is shown in Fig. 4.7. In the RVB, as we have discussed in Sec. 4.2.4 and Fig. 4.7, the squared order parameter based on the sampled values from Eq. (4.10) is not exactly the same as the actual four-spin correlation function, but we have shown that the scaling properties are the same.

We here study the probability distribution  $P(D_x, D_y)$  generated in the Monte Carlo sampling. Each generated configuration of the valence bonds corresponds to pair of values

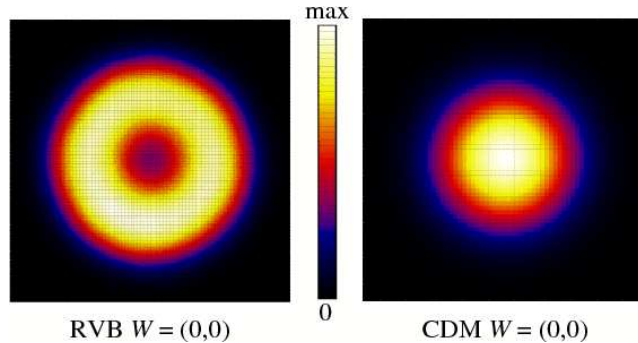


Figure 4.14: VBS order parameter distribution function  $P(D_x, D_y)$  in the space of point pairs  $(D_x, D_y)$  generated in the Monte Carlo simulations of the RVB state (left) and CDM (right) for systems of size  $L = 64$ . We are only concerned here with the shapes of these distributions (a ring with depleted weight in the center for the RVB and a broad central peak for the CDM) and have therefore not labeled the graphs with the range of  $(D_x, D_y)$  or the actual values of the probability density.

$(D_x, D_y)$  evaluated according to the loop estimator (2.12). We use these to accumulate the histogram  $P(D_x, D_y)$ . Such histograms were generated by Sutherland in his loop-gas study, [62, 63] and he noted a circular symmetry of the distribution (instead of a 4-fold symmetry that would have been naively expected due to the lattice symmetry). At that time the results were affected by very large statistical uncertainties, however.

Dimer order-parameter histograms have recently become interesting in the context of *deconfined quantum critical* (DQC) points [28, 29, 141] in models exhibiting quantum phase transitions between the antiferromagnetic Néel state and a VBS state. [107, 108] A long-range ordered columnar VBS corresponds to a distribution  $P(D_x, D_y)$  peaked at one of the four points  $(\pm|D|, \pm|D|)$ , with the magnitude  $|D|$  growing linearly with the system size  $N = L^2$ . In a finite system, in which the  $Z_4$  symmetry is not broken, one expects equal weight in all these four peaks, as well as some weight between the peaks (which is related to the tunneling probability between the four ordered VBS states). As a DQC point is approached from the VBS side, one expects an emergent U(1) symmetry in the system. [28, 29] This is manifested in  $P(D_x, D_y)$  as a circular-symmetric distribution, [107, 141] i.e., for a finite system size  $L$ , the discrete four-fold ( $Z_4$ ) symmetry naively expected for the VBS

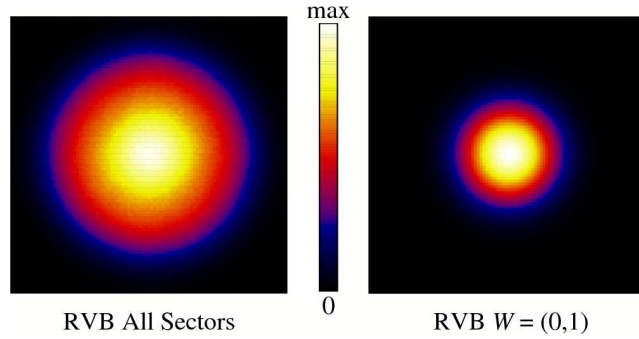


Figure 4.15: VBS order parameter distribution function  $P(D_x, D_y)$  for  $L = 48$  systems in the grand-canonical winding number ensemble (left) and with winding number  $W = (0, 1)$  (right). Here the range of  $D_x, D_y$  values is the same in both cases, i.e., the distribution for  $W = (0, 1)$  is much narrower.

evolves into a continuous  $U(1)$  symmetric distribution. For fixed couplings, the  $Z_4$  symmetry develops as  $L$  exceeds a length-scale characterizing the spinon confinement (which diverges at the DQC point).

While the RVB is a critical state, it does not correspond to a DQC point, because the spin correlations decay exponentially. At a DQC point, both the spin and dimer correlations are critical. [28, 29] It is nevertheless interesting to study the symmetry of the critical VBS order parameter in the RVB and to compare it with the corresponding distribution in the CDM [where in  $\mathbf{S}(x, y) \cdot \mathbf{S}(x + 1, y)$  is replaced by the dimer occupation number on the bond]. Results for  $L = 64$  systems in the winding number sector  $W = (0, 0)$  are shown in Fig. 4.14. Completely circular-symmetric distributions are seen in both cases, with no signs of  $Z_4$  anisotropy. The natural expectation for a critical state is that the weight is centered around  $(D_x, D_y) = (0, 0)$ , and this is in fact true for the CDM. Surprisingly, it is *not* true for the RVB critical state: the distribution is instead ring shaped, with the dominant weight a finite radius away from the center. This is the behavior seen in candidate models for DQC points in the VBS state close to the phase transition into the Néel state. The ring-shaped distribution in the RVB case is no contradiction to its being a critical state, because the ring's radius still grows slower with  $L$  than  $L^2$ . The expectation value  $\langle D^2 \rangle / N$  is twice the

structure factor  $S(\pi, 0)$  and hence grows as  $L^{2-\alpha}$ , with  $\alpha \approx 1.20$  determined in Sec. 4.2.4.

In the case of a fixed non-zero winding number, the VBS order parameter is modulated by a plane wave, in the same way as its correlation function is, as discussed in Sec. 4.2.4. Hence its spatial average tends to cancel, with the result that the distribution function now has a central peak, as seen in Fig. 4.15 (right panel) for  $W = (0, 1)$ . For large winding numbers the distribution is marginally oval-shaped, reflecting the anisotropy induced by large winding numbers (see Appendix B). In Fig. 4.15 the anisotropy is too small to observe clearly. Interestingly, when all winding numbers are included in grand-canonical simulations, the ring-shaped distribution seen for  $W = (0, 0)$  in Fig. 4.14 no longer obtains. Although this sector completely dominates the grand-canonical ensemble (as seen in Fig. 4.3), the narrow central peaks contributed by the non-zero winding number sectors completely fill in the central portion inside the ring, resulting in a broad central peak, as shown in Fig. 4.15 (left panel).

## 4.5 Summary and discussion

We have compared long-wavelength properties of short-bond RVB spin-liquid states with those of classical dimers, specifically those associated with correlations and topological constraints of dimers. Taking properly into account the non-orthogonality of valence-bond basis states, arising from the internal bond-singlet spin structure which is not present in classical dimers, we have carried out numerically exact Monte Carlo simulations of the four-point correlation function measuring the tendency to formation of a VBS state. In contrast to the exponentially decaying two-point spin correlations, [53] these VBS correlations decay as a power law. Such a power might have been anticipated based on the fact that the classical dimer-dimer correlations decay as  $1/r^2$  (although the overcompleteness of the RVB could in principle have led also to more dramatic deviations from the CDM), but the exact value of the exponent necessitates an exact treatment of the overcomplete basis, as we have done here. The result is that the correlations decay slower than what might have been anticipated, as  $1/r^\alpha$  with  $\alpha \approx 1.20$ .

The weighting of valence bond states is (qualitatively) different in that sampling the RVB state involves the transition graph of two states, whereas in the CDM only a single state is sampled (as different dimer configurations are by definition orthogonal). In particular, the loops are small in the short-bond RVB, as they necessarily must be in order to give exponentially decaying spin correlations (whereas in an antiferromagnetically ordered state the typical loop size scales as the system size [64,134]). The operators that we measure are also different in the two systems: the “dimer-dimer” correlations in the RVB actually refer to two-spin operators, [Eq. (4.2)] in place of just bond occupation numbers in the CDM. We have confirmed that the changed  $\alpha$  exponent (and presumably other changed expectations) in the RVB state originate solely from the different state weighting, not from the form of the correlation-function estimator (2.15).

The RVB structure factor has a “pinch-point” at  $(\pi, \pi)$  in reciprocal space, in any winding number sector, like the well-known pinch-point in the CDM and other height models; it further shows singularities related to the critical correlations near to  $(\pi, 0)$  (but shifted by nonzero winding number) which are logarithmic for CDM at zero winding number, and otherwise are variable power laws. Finally, we found that introduced pairs of monomers, i.e., topological defects, are marginally (power-law) deconfined with a power law distribution of their separations.

Remarkably, all of the above observations fit into the framework of the “height model” with a stiffness constant  $K$  as worked out in Appendix B. Independent measurements of the stiffness constant can be derived from (i) logarithms of the probabilities of sectors with different winding numbers, (ii) the critical dimer correlation exponent, (iii) the monomer pair separation exponent, and (iv) the pinch point of the structure factor  $S(\mathbf{q})$ . All yielded  $K_{\text{RVB}} \approx 1.6K_{\text{CDM}}$ . Other behaviors, which do not yield measurements of  $K$ , are also suggestive of this. Thus, our results vindicate at last the qualitative correctness of the zero-overlap assumption adopted in the RK QDM, although quantitatively the RVB state has a larger degree of VBS order (as expressed by that ratio of stiffnesses 1.6). It is as if the RVB state were the ground state of the generalized RK state corresponding to some (still

unknown) generalized classical dimer model.

We extended the model by introducing a small fraction of longer bonds (the next bipartite bond, which connects fourth-nearest neighbors). We studied the evolution of the power laws characterizing the dominant VBS correlations and monomer correlations as a function of the fugacity of long bonds. As in the CDM case, [66], in the dimer-dimer correlations, a  $(\pi, \pi)$  modulated “dipolar” term continues to have the  $1/r^2$  behavior; on the other hand, a  $(\pi, 0)$  modulated “critical” term has an increasing exponent, while the monomer-monomer distribution function has a decreasing exponent, both of which can be explained in terms of a decreasing stiffness for the “height” fluctuations. The monomers remain deconfined for all fugacities we studied.

We further studied the modifications to correlations due to finite topological winding number, for both the RVB and classical dimers. The critical VBS correlations acquire a sinusoidal modulation, correlations become anisotropic, and the effective stiffness is increased, as expected from height-model calculations;

We have also studied the joint probability distribution  $P(D_x, D_y)$  of the VBS order parameters for columnar order with  $x$  and  $y$  oriented bonds. We found this distribution to be U(1) symmetric, which in analogy with the proposed deconfined quantum-critical point [28, 29] should correspond to the lattice-imposed  $Z_4$  symmetry of the VBS on the square lattice to be dangerously irrelevant [when regarded as a perturbation to an U(1) symmetric field theory] in these critical systems (both in the RVB and the CDM). In a model that has one of these states as the ground state for some values of tunable parameters, e.g., the extended dimer models with “Cantor deconfinement” studied in Refs. [132] and [131], one would then expect the U(1) symmetry to be emergent upon approach to the critical point.

Although we have here studied the RVB state without reference to any specific Hamiltonian, some general conclusions can still be drawn based on our results. If a (local) Hamiltonian’s ground state has algebraic correlations, then it must correspondingly have gapless excitations. Thus, our results show that any Hamiltonian [44] with the RVB ground

state is *gapless* in the singlet sector, even though it has a spin gap. Furthermore, the close qualitative correspondence of the RVB static correlations to the RK model [43] suggests the long-wavelength excitations are similar too; these are known [116] to be coherent bosons with  $q^2$  dispersion. Some actual spin systems may be spin gapped but singlet gapless. This has long been claimed for the spin-1/2 kagome antiferromagnet, [142, 143] although the spin gap is small enough that an extrapolated value of zero can not be ruled out. [144] From this viewpoint, it is interesting to verify that the original short-range RVB state has such a property.

In experiments, the 2D organic  $S = 1/2$  spin-liquid candidate,  $\text{EtMe}_3\text{Sb}[\text{Pd}(\text{dmit})_2]_2$  shows gapless spin and singlet sectors in zero magnetic field, [145] but in a magnetic field, spin excitations become gapped while singlet excitations remain gapless and have high mobility, as indicated by specific heat and thermal conductivity.

On the theory side, one might ask whether our result should have been expected. Soon after the original proposal of the RVB wave function, field theorists argued that it corresponded to a  $U(1)$  gauge theory, [101, 126, 128] and for a “height model” to be in its rough phase, as we found, is equivalent to being asymptotically a  $U(1)$  gauge theory. But, the numerical value of the stiffness constant  $K$  has not been measured previously (before our original estimate in Ref. [124]); to our knowledge, it was not even suggested whether  $K$  should be larger or smaller than  $K_{CDM}$  of the quantum dimer model. If for no other reason, one must check the value of  $K$  since, were it much larger, one would find long-range order in the dimer correlations (a spin-Peierls phase).

It would clearly be interesting to try to derive the height model (or the continuum version of it) starting from an  $1/N$  expansion of the classical dimer model, which corresponds to the RVB for  $SU(N)$  spins in the limit  $N \rightarrow \infty$ . Further, the recent construction [44] of a model Hamiltonian which has exactly the RVB state studied here as its ground state also offers hope that one could actually, with extensions of that Hamiltonian, study a quantum phase transition in which the static properties of the critical point should be exactly those that we have investigated here in the RVB.

# Chapter 5

## Amplitude Product States in 1D Chains

### 5.1 Introduction

The valence-bond (VB) basis [31, 53, 63, 146–148] is ideally suited for describing many different types of ground states and low-energy excitations of quantum spin models [2, 67–69, 74, 78, 114, 115, 134, 149, 150]. In the case of  $S = 1/2$  spins in the singlet sector, a basis state corresponds to a tiling of the lattice into bonds connecting pairs of sites forming singlets, such that each spin belongs to one bond. This basis is overcomplete if bonds of all lengths are included. To describe the ground state of a Hamiltonian with bipartite interactions, only bonds connecting sites on different sublattices have to be included—this restricted VB basis exactly reproduces Marshall’s sign rule [61] for the ground state of such a system. Thus, in this basis the wave function is positive definite and can be sampled using Monte Carlo (MC) techniques, as discussed in Sec.2.1.

In this introductory section we review the definition and properties of the well-studied Liang-Doucot-Anderson amplitude-product states [53] and their spin and dimer correlation functions (first introduced in Sec.2.1.3). We would like to refer readers who are interested in the Monte Carlo sampling method to Sec. 2.1.

### 5.1.1 Amplitude-product states

The most commonly used variational states in this context are the AP states introduced by Liang, Doucot, and Anderson [53]. Here one associates a bond connecting two sites  $(a, b)$  with an amplitude  $h(a, b)$ , which in the case of a translationally-invariant system is only a function of the lattice vector  $\mathbf{r}_{ab}$  separating the two sites;  $h(a, b) = h(\mathbf{r}_{ab})$ . The wave function coefficient for a VB configuration  $V$  is then

$$\psi(V) = \prod_{\mathbf{r}} h(\mathbf{r})^{n_{\mathbf{r}}}, \quad (5.1)$$

where  $n_{\mathbf{r}}$  is the number of bonds of “shape”  $\mathbf{r}$  in the configuration.

The amplitudes  $h(\mathbf{r})$  can be used as variational parameters. In the original work with the AP states to describe the ground state of the two-dimensional (2D) Heisenberg model [53], only the amplitudes for a small number of short bonds were optimized, and different functional forms (exponentially or power-law decaying with the distance  $r$ ) were tested. In later work all the amplitudes (on finite lattices) were optimized, leading to relative energy errors (deviations from results from unbiased quantum Monte Carlo, QMC, calculations) of less than 0.1% [64, 151]. In the optimal state the amplitudes decay asymptotically as  $1/r^3$ , which is also the result of a mean-field VB approach [134].

In some cases, if one is just interested in the properties of some class of states without reference to a specific Hamiltonian, the optimization step is not needed. This approach has been taken in recent studies of the prototypical resonating VB (RVB) spin-liquid state consisting of the superposition of all configurations of the shortest (nearest-neighbor) bonds on the square lattice [40, 45, 46], and also in the presence of some fraction of the second bipartite bond (fourth-neighbor) [45] (which is covered in Chapter 4). These wave functions, for which the parent Hamiltonian was recently identified (in the case of nearest-neighbor bonds only) [44], has exponentially decaying spin correlations but power-law decaying VBS correlations. A phase transition from the Néel state into this kind of spin liquid can be achieved by using amplitudes of the form  $h(r) \propto 1/r^{\kappa}$  and tuning the exponent  $\kappa$  to a critical value [134, 152].

In this chapter, we closely examine the Néel–VBS transition within the standard AP states in one dimension, with amplitudes  $h(r)$  of the form  $1/r^\alpha$ . This transition, which occurs at a critical value of  $\alpha$  (which is not universal but depends on the detailed form of the amplitudes for small  $r$ ) was previously studied by Beach [134], but only the spin correlations were computed. Here we extract also the VBS correlations and confirm that there is a single critical point versus  $\alpha$ . The exponents are continuously varying, depending on the short-bond amplitudes.

### 5.1.2 Spin and dimer correlations

In order to characterize the different phases realized by the AP states, we evaluate order parameters for detecting antiferromagnetic (AFM) order and VBS order. AFM order can be characterized using the standard two-spin correlation function,

$$C(\mathbf{r}_{ij}) = \langle \mathbf{S}_{\mathbf{r}_i} \cdot \mathbf{S}_{\mathbf{r}_j} \rangle (-1)^{(x_{ij}+y_{ij})}, \quad (5.2)$$

where we use  $\mathbf{r}_{ij}$  to denote the vector separating the lattice sites  $i$  and  $j$  and the phase factor cancels the signs of the staggered spin correlations obtaining in the systems we study. Alternatively, one can study the full sublattice magnetization averaged over the whole system;

$$\mathbf{m}_s = \frac{1}{N} \sum_i \phi_i \mathbf{S}_i, \quad (5.3)$$

where  $\phi_i = +1$  on sublattice A and  $\phi_i = -1$  on sublattice B. Since the singlet AP states manifestly cannot break the spin-rotation symmetry, order must be detected in the squared order parameter  $\langle \mathbf{m}_s^2 \rangle$ , which in the limit of large system size will be identical to the long-distance spin correlation (5.2).

To accurately locate an antiferromagnetic phase transition, the Binder cumulant is very useful. It is defined according to [153]

$$U = \frac{5}{2} \left( 1 - \frac{3}{5} \frac{\langle \mathbf{m}_s^4 \rangle}{\langle \mathbf{m}_s^2 \rangle^2} \right), \quad (5.4)$$

where the factors are chosen for the 3-component AFM order parameter such that  $U(N \rightarrow \infty) = 0$  in the disordered phase (where the order-parameter distribution is a Gaussian with zero average) and  $U(N \rightarrow \infty) = 1$  in the ordered phase (where the radial distribution is peaked at non-zero  $m_s$ ). Typically crossing points of  $U$  graphed versus a control parameter for different system sizes approach the critical point vary rapidly as a function of increasing system size.

To characterize VBS order we use the dimer correlation function, defined as

$$D_{xx}(\mathbf{r}_{ij}) = \langle B_x(\mathbf{r}_i)B_x(\mathbf{r}_j) \rangle, \quad (5.5)$$

in terms of the bond operators

$$B_x(\mathbf{r}_i) = \mathbf{S}_{\mathbf{r}_i} \cdot \mathbf{S}_{\mathbf{r}_i + \hat{\mathbf{x}}}, \quad (5.6)$$

directed along the unit vector  $\hat{\mathbf{x}}$ . In some cases we will characterize VBS order by the long-distance behavior of Eq. (5.5). The states we will be studying have a 2-site VBS unit cell, forming a staggered weak-strong-weak-strong pattern in one dimension. We can extract the dominant component of the correlations, corresponding to the squared order parameter, by taking the appropriate difference of Eq. (5.5) evaluated at nearby distances. We here use a symmetric version of this difference;

$$D_{xx}^*(\mathbf{r}) = D_{xx}(\mathbf{r}) - \frac{1}{2} [D_{xx}(\mathbf{r} - \hat{\mathbf{x}}) + D_{xx}(\mathbf{r} + \hat{\mathbf{x}})]. \quad (5.7)$$

The above two- and four-spin correlations are related to the transition-graph loops generated in the VB MC sampling process. For instance, the estimator for the two-spin correlation is given by [53, 63]

$$\frac{\langle V_\alpha | \mathbf{S}_{\mathbf{r}_i} \cdot \mathbf{S}_{\mathbf{r}_j} | V_\beta \rangle}{\langle V_\alpha | V_\beta \rangle} = \begin{cases} \pm \frac{3}{4}, & [i, j], \\ 0, & [i][j], \end{cases} \quad (5.8)$$

where  $[i, j]$  and  $[i][j]$  denote sites  $i$  and  $j$  belonging to the same loop and different loops, respectively, and the sign in the case  $[i, j]$  is  $+$  and  $-$  for spins on the same and different sublattices, respectively. From Eq. (5.8) one can also obtain a very simple expression for

the estimator for the squared staggered magnetization,

$$\frac{\langle V_\alpha | \mathbf{m}_s^2 | V_\beta \rangle}{\langle V_\alpha | V_\beta \rangle} = \frac{3}{4} \sum_{\ell=1}^{l_{\alpha\beta}} \mathcal{L}_\ell^2, \quad (5.9)$$

where  $\mathcal{L}_\ell$  is the size (the number of sites) of loop  $\ell$ .

Both the dimer correlation function and the fourth power of the staggered magnetization involve four-spin correlations. Detailed descriptions on how to calculate these based on the transition graph of two VB configurations can be found in Appendix A. Here we only write down the expression for the fourth power of the staggered magnetization, needed for the Binder cumulant Eq. (5.4),

$$\frac{\langle V_\alpha | \mathbf{m}_s^4 | V_\beta \rangle}{\langle V_\alpha | V_\beta \rangle} = \sum_{\ell} \mathcal{L}_\ell^2 + \frac{15}{16} \left( \sum_{\ell} \mathcal{L}_\ell^2 \right)^2 - \frac{5}{8} \sum_{\ell} \mathcal{L}_\ell^4 \quad (5.10)$$

which is also solely determined by the sizes of all loops formed in the transition graph. We note that the Binder cumulant of the VBS order parameter is much more difficult to evaluate, since its definition in analogy with (5.4) requires eight-spin correlations. While these also in principle can be evaluated in terms of the transition-graph loops [31], the expressions are quite complicated to implement in practice and we have not done so.

### 5.1.3 Outline of the chapter

In Sec. 5.2 we study the Néel–VBS transition in 1D AP states and their continuously varying critical exponents. In Sec. 5.3, we discuss the measurement of the entanglement entropy of AP states. We conclude in Sec. 5.4 with a summary and discussion of future prospects.

## 5.2 Phase Diagram in 1D

In one dimension, the standard AP states given in Eq. (5.1) are able to reproduce a Néel–VBS transition without correlation factors. We will study this 1D transition carefully in this section, using the very efficient loop update of the VB configurations.

It is natural to study the evolution of the state as a function of some parameter governing the long-distance behavior of the amplitudes, e.g., using the power law  $h(r) = 1/r^\kappa$  with

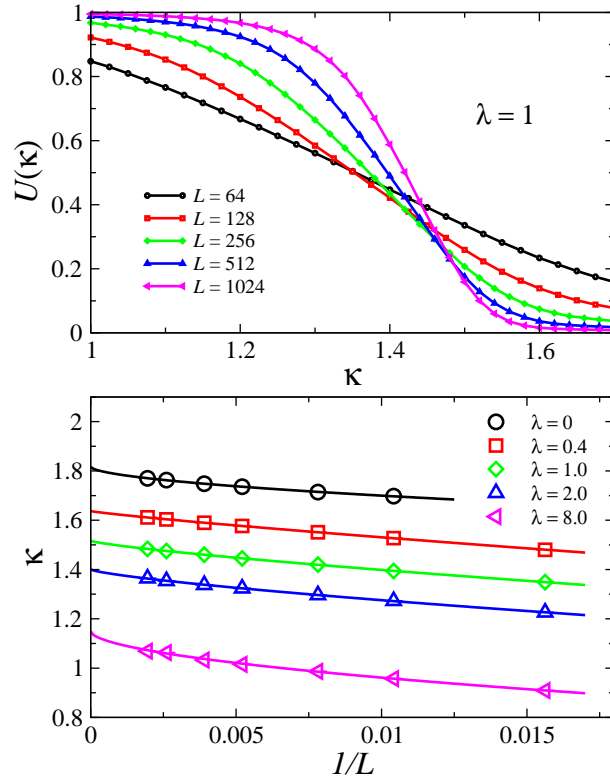


Figure 5.1: The upper panel shows the crossing behavior of the Binder cumulant  $U(\kappa)$  defined in Eq. (5.4) for several different chain lengths  $L$  when  $\lambda = 1$ . The approach to 1 for small  $\kappa$  and 0 for large  $\kappa$  corresponds to the presence and absence of Néel order, respectively. The crossing point approaches the critical value of  $\kappa$ . The lower panel demonstrates extrapolations to the thermodynamic limit of the critical  $\kappa_c$  by fitting crossing points of  $(L, 2L)$  pairs to the power-law correction (5.12).

tunable  $\kappa$  or an exponential form. Here we will use the power-law. However, it is already known that the nature of the state is not just determined by the asymptotic behavior of  $h(r)$ , but also depends on details of the short-bond weights [134]. In addition to the exponent  $\kappa$  we here tune the shortest-bond amplitude  $h(r = 1) = \lambda$ . The wave function is, thus, explicitly given by

$$\psi(V) = \lambda^{n_1(V)} \prod_{r>1} \left( \frac{1}{r^\kappa} \right)^{n_r(V)}, \quad (5.11)$$

where  $n_r(V)$  again refers to the number of bonds of length  $r$  in the bond configuration  $V$ .

It is clear that for  $\lambda > 0$  and large  $\kappa$  this AP state is a VBS, since in the limit  $\kappa \rightarrow \infty$  only two configurations contribute; those with  $r = 1$  bonds on alternating links. For small  $\kappa$  there is instead Néel order but no VBS order [134]. Note that long-range order corresponding to broken SU(2) symmetry is possible in this kind of 1D system, since viewed as a classical statistical-mechanics problem there are long-range interactions (since the bonds have unbounded length), and the Mermin-Wagner theorem [95] prohibiting 1D Néel order does not apply. Note also again that the AP wave function is a singlet and, thus, the SU(2) symmetry is not actually broken (as in any calculation targeting the singlet ground state). The magnitude of the Néel order measured by  $\langle m_s^2 \rangle$ , Eq. (5.3), or the long-distance correlation function Eq. (5.2) can still evolve toward a non-zero value as the system size grows, tending to the square of the symmetry-broken value of  $m_s$  in the corresponding thermodynamic-limit state with no constraint on the total spin.

Beach has previously studied Néel ordering in this class of wave functions (with a somewhat different parametrization of the short-bond amplitudes) [134]. He found a continuous transition between the Néel state and the non-magnetic state. Here we also investigate the VBS correlations and find a single transition point where both the spin and dimer correlations are critical. We study the evolution of the transition in the plane  $(\kappa, \lambda)$ .

For fixed  $\lambda$ , in order to find the critical value of  $\kappa_c$  of the AP state we study the Néel Binder cumulant Eq. (5.4). The behavior of curves for different system sizes  $L$  crossing each other as a function of  $\kappa$  is illustrated in the upper panel of Fig. 5.1. The crossing points do not fall exactly on a single point due to subleading size corrections. We observe a systematic smooth drift of the crossing points as the system size is increased. In order to eliminate this size effect and determine the critical point from data such as those in Fig. 5.1, we extract  $\kappa$ -values corresponding to crossing points of  $(L, 2L)$  size pairs, and plot these points against  $1/L$ , as shown in the lower panel of Fig. 5.1. We then extrapolate these values to  $L \rightarrow \infty$  and obtain  $\kappa_c$ . The fitting function we use here for extrapolation is the standard power-law [153];

$$f_c(L, 2L) = \kappa_c + \frac{a}{L^b}. \quad (5.12)$$

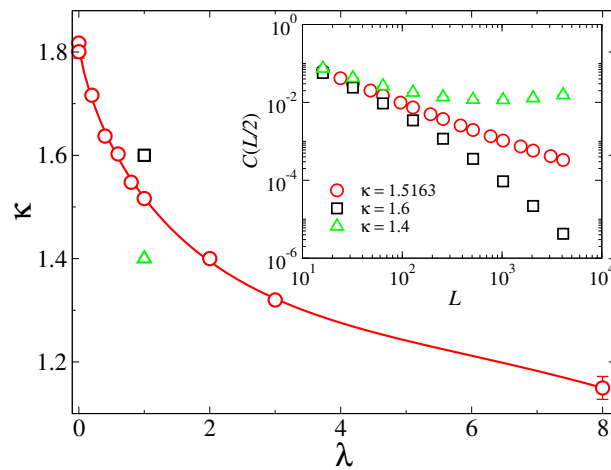


Figure 5.2: Phase diagram of 1D AP states with tuning parameters  $\kappa$  and  $\lambda$ , as defined in Eq. (5.11). The circles are calculated transition points and the curve is a guide to the eye representing approximately the boundary between the long-range ordered Néel (below) and VBS (above) phases. The inset exemplifies long-distance spin correlation functions inside the phases and at the critical point when  $\lambda = 1$ ; the black squares correspond to  $\kappa = 1.6$  (inside VBS phase) and the green triangles are for  $\kappa = 1.4$  (in the Néel phase). The red circles show the behavior at the critical point.

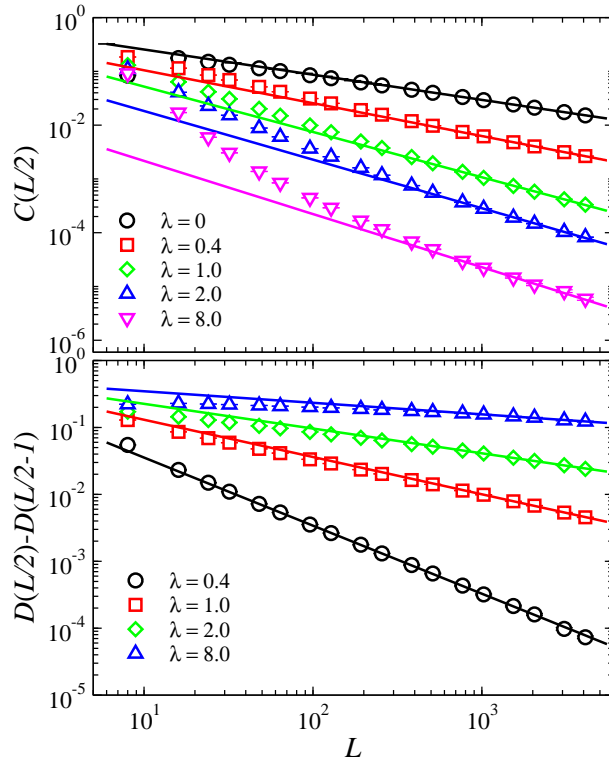


Figure 5.3: Staggered spin-spin (upper panel) and dimer-dimer (lower panel) correlations of 1D AP states at the largest distance, graphed versus the chain length at  $\kappa = \kappa_c$  for different short-bond amplitudes  $\lambda$ . All lines are fits to the form  $aL^{-b}$ .

The extrapolated  $\kappa_c$  values versus  $\lambda$  are plotted in Fig. 5.2; the phase diagram of 1D AP states with the two tuning parameters  $\lambda$  and  $\kappa$ . The inset of this figure demonstrates the qualitatively different behaviors of the spin correlation functions in the two phases and at the critical point, using  $\lambda = 1$  results as an example. At  $\kappa = 1.6$  the correlations decay faster than power-law, as is expected for a non-magnetic VBS ordered state. In contrast, at  $\kappa = 1.4$ , the correlations for small  $L$  first decay somewhat but then converge to a non-zero value for larger  $L$  (even increasing somewhat for large systems), demonstrating the presence of long-range Néel order. At the critical value  $\kappa_c$  extracted using the Binder crossings as explained above, the decay of the correlations are consistent with a critical, power-law form.

To determine whether the VBS correlations are also critical at the  $\kappa_c$  points extracted from the Néel Binder cumulant, we further study both the spin and dimer correlations

at these points. The results confirm the expectation of a common critical Néel and VBS point. By studying chains as large as  $L = 4096$ , we can extract the exponents governing the critical correlation functions with relatively small error bars (thanks to the powerful VB MC loop update discussed in Sec. 2.1). The analysis of the power laws is presented in Fig. 5.3. Note that in order to avoid boundary modifications of the power-law correlation functions as a function of the distance  $r$  in systems of fixed  $L$ , we study the long-distance correlations versus the system size, with  $r = L/2$  for the spin correlations and the staggered component of the dimer correlations extracted based on  $r = L/2$  and  $L/2 - 1$  data according to Eq. (5.7) [where it should be noted that  $D(L/2 - 1) = D(L/2 + 1)$  for a periodic chain]. In practice, this method is typically more convenient than studying the behavior as a function of  $r$  for very large  $L$ , because the finite-size effects from the periodic boundaries (which enhance the long-distance correlations [154]) are significant and one has to choose a longest distance  $r_{\max} \ll L$  when fitting data. The asymptotic behavior appears to be approached faster in the long-distance correlations versus  $L$ , but the  $r$  dependence for large  $r$  gives very similar results (up to a factor, due to the aforementioned boundary-enhanced long-distance correlations when plotted versus  $L$ ).

As  $\lambda$  increases, larger system sizes are needed to observe the asymptotic critical forms. Especially for the largest  $\lambda$  studied,  $\lambda = 8$ , one can observe in Fig. 5.3 (upper panel) a clear cross-over of the spin correlation function from a rapidly decaying short-distance form to the asymptotic power-law form. The straight lines in Fig. 5.3 are fits to the simple asymptotic form  $aL^{-b}$ . We have also tried to include shorter chains in an analysis including corrections, by fitting to the form  $aL^b + cL^d$ . This form is, however, not capable of describing the small size effect in this model (in contrast to 2D critical spin liquid RVB states, where this form works very well [45]). In any case, the large- $L$  behaviors appear to be reasonably well converged to the simple power law and the exponents extracted should be reliable. An exception is  $\lambda = 0$ , for which the dimer correlations decay very rapidly and are too noisy to allow the exponent  $\beta$  to be reliably determined (and we have therefore not graphed these correlations in Fig. 5.3). It is even possible that the VBS state for  $\lambda = 0$  is of a different

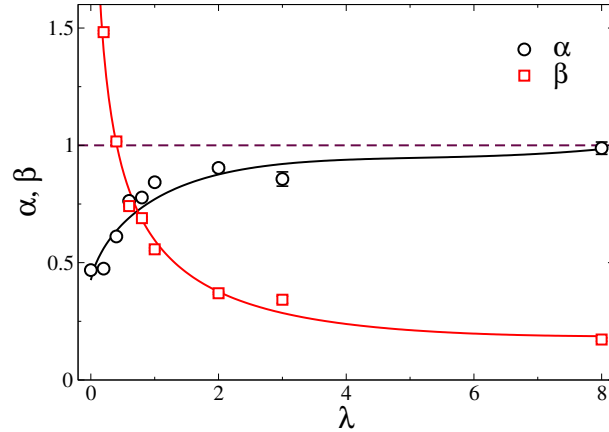


Figure 5.4: The continuously varying spin ( $\alpha$ ) and dimer ( $\beta$ ) decay exponents of the 1D AP state (5.11) as a function of the short-bond amplitude  $\lambda$ . The exponents correspond to the power-law decay of the correlation functions;  $C(r) \sim r^{-\alpha}$ ,  $D^*(r) \sim r^{-\beta}$ . The points are calculated values and the curves are guides to the eye.

kind than for  $\lambda > 0$ . Further studies will be needed to settle this issue.

We plot the extracted critical exponents as a function of  $\lambda$  in Fig. 5.4. The exponents vary continuously with  $\lambda$ , with the dimer exponent decreasing monotonically and the spin exponent increasing. An interesting conclusion that can be drawn from these results is that the critical state becomes increasingly “quasi VBS ordered” with increasing  $\lambda$ , with the decay exponent of the dimer correlations perhaps vanishing as  $\lambda \rightarrow \infty$ , although this is difficult to confirm definitely (because the simulations become increasingly difficult for large  $\lambda$ ). The behavior is in line with the expectation that a large lambda favors VBS ordering because of the predominance of the very shortest bonds, i.e., when moving on the critical line toward higher  $\lambda$  the density of short bonds increases, and this leads to a strengthening of the VBS quasi-order. At the same time, the exponent of the spin correlations appear to approach 1. However, Néel order still exists for large  $\lambda$  when reducing  $\kappa$  from the critical value. In terms of the transition graph estimators of the correlation functions, VBS correlations correspond to certain loop correlations [31], while Néel order is related to the presence of long ( $\propto L$ ) loops. While long-range Néel and VBS orders are mutually exclusive in these states, the Néel state in the neighborhood of the critical curve for large  $\lambda$  approaches

a coexistence situation. Here the magnitude of the Néel order parameter also becomes very small, however, and the coexistence is therefore not robust. One notable aspect of the AP states is that they are not able to reproduce the ground state of the critical Heisenberg chain, where  $\alpha = \beta = 1$  [155].

### 5.3 Rényi Entanglement Entropy Calculations

The VB formulation of the ground state of a spin chain can be viewed as a 1D classical statistical mechanics problem, but at the same time it should also correspond to a path-integral formulation in  $1 + 1$  dimensions (with some underlying parent Hamiltonian). One may then expect the system to be classifiable according to the standard 2D conformal field theories by a central charge  $c$ . Varying critical exponents, as we have found here, normally imply  $c \geq 1$ , but the unknown parent Hamiltonians that may include long-range interactions may invalidate this requirement, although it is not clear how the power-law bond length translates into effective interactions in an underlying parent Hamiltonian (and the interactions in it may in the end well be short-ranged).

In this section, in order to explore the possibilities of classifying AP states with central charge  $c$ , we compute the bipartite entanglement entropy of the AP state to test its system size scaling and consistency between  $c$  extracted from it [156–158] and from the correlation functions. Such calculations can be carried out using the VB MC sampling scheme as introduced in Sec. 2.3 and references [40, 159]. We here present our analysis methods and results.

#### 5.3.1 Fitting method

For a 1D periodic quantum spin chain with size  $L$ , let us divide the chain into subsystem  $A$  with  $l$  sites and subsystem  $B$  with  $L - l$  sites. Recall from Sec. 1.5, the Rényi entanglement entropy (REE) is defined as,

$$S_n(\rho_A) = \frac{1}{(1-n)} \ln[\text{Tr}(\rho_A^n)], \quad (5.13)$$

where  $\rho_A$  is the reduced density matrix of subsystem  $A$  and  $n$  is a positive index number. When  $n = 1$ , it restores the von Neumann entropy. The scaling of REE carries a universal constant  $c$ , the so-called ‘‘central charge’’, as expressed in [51, 156, 157]

$$S_n(l) = \frac{c}{6} \left(1 + \frac{1}{n}\right) \ln \left[ \frac{L}{\pi} \sin \left( \frac{\pi l}{L} \right) \right] + d_n, \quad (5.14)$$

where  $d_n$  is a nonuniversal constant. For the anisotropic spin-1/2 chain [160] and the spin-1 Fateev-Zamolodchikov model [158], strong oscillations in the REE with order index  $n > 1$  require finite-size corrections to the scaling form [Eq. (5.14)]. In order to capture the oscillation, a general form is expressed as [158]

$$S_n(l) = \frac{c}{6} \left(1 + \frac{1}{n}\right) \ln \left[ \frac{L}{\pi} \sin \left( \frac{\pi l}{L} \right) \right] + g_n \cos(Kl) \left[ \sin \left( \frac{\pi l}{L} \right) \right]^{2X^{con}/n} + a_n \left[ \sin \left( \frac{\pi l}{L} \right) \right]^\nu + b_n \left[ \sin \left( \frac{\pi l}{L} \right) \right]^{-2(X^I-2)} + d_n, \quad (5.15)$$

where  $K$  gives the spacial period of the oscillation,  $X^{con}$  is related to the scaling dimension of the energy operator of the model, and  $X^I$  is the dimension of the standard scaling operator. Because we do not know the underlying Hamiltonian of 1D AP states with different critical amplitudes, we combine the two terms of  $\sin(\frac{\pi l}{L})$  in Eq.(5.15) into one to reduce the fitting complexity. The scaling of the second order REE therefore can be simplified as

$$S_2(l) = \frac{c}{4} \ln \left[ \frac{L}{\pi} \sin \left( \frac{\pi l}{L} \right) \right] + a_2 \cos(Kl) \left[ \sin \left( \frac{\pi l}{L} \right) \right]^{X^{con}} + b_2 \left[ \sin \left( \frac{\pi l}{L} \right) \right]^{e_2} + d_2. \quad (5.16)$$

We test the correctness of Eq. (5.16) on 1D Heisenberg model, as demonstrated in Fig. 5.5. The REE  $S_2$  was calculated by the density matrix renormalization group (DMRG) for  $L = 128$  Heisenberg chain (the DMRG data was kindly offered by Roger G. Melko). The red solid line is the fit done through Eq.(5.16), which captures all details in the oscillation and gives the expected central charge  $c = 1.00(1)$  accurately. From the observation of the data, we have set the periodicity parameter  $K = \pi$ , and downsized the number of fitting parameters from seven to six.

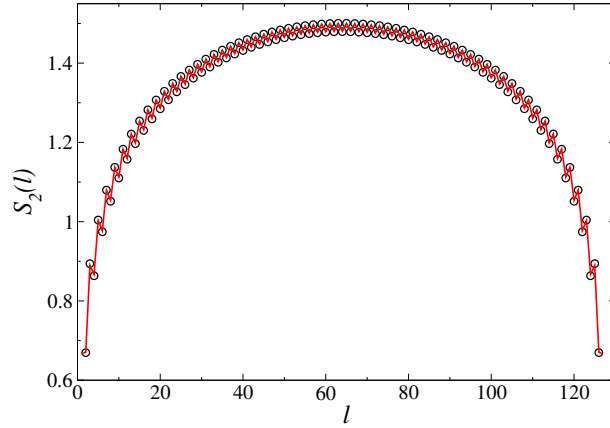


Figure 5.5: Second Rényi entanglement entropy calculated by using the DMRG method for the 1D Heisenberg chain. The solid line is the fit by the scaling function in Eq. (5.15).

To avoid complicated and ill-converging operations in the least-square fits of these six parameters, in practice, we employ a simple and effective fitting method for this study: We randomly choose a point in a six-dimensional parameter space, with each coordinate corresponding to one fitting parameter in Eq. (5.16). We repeatedly do this millions of times and find out a point whose six coordinates give the smallest reduced  $\chi^2$  among all trials. Initializing these six parameters with good approximations, and assigning reasonable ranges to draw the point help to reach the minimum  $\chi^2$  efficiently. Since fitting errors might be correlated, in order to calculate correct error bars of fitting parameters, we implement the bootstrapping method [161]. We apply our fitting method repeatedly over the bootstrapped data sets from MC bin data, then we calculate standard error bars over all bootstrapping steps.

The oscillation separates the  $S_2$  measurement into two branches, on even and odd sites respectively. These two branches scale similarly and each can be described by Eq. (5.14) with different constant  $d$ . After extracting data points out of one branch, we could further simplify the fitting procedure by using the scheme introduced above with Eq. (5.14), which only has two fitting parameters, i.e.  $c$  and  $d_2$ . In addition, since there is no explicit size dependence of  $S_2$  for moderately large systems (which agrees with the results from the Heisenberg chain [159]), we can fit all data together with the fixed central charge  $c$  and

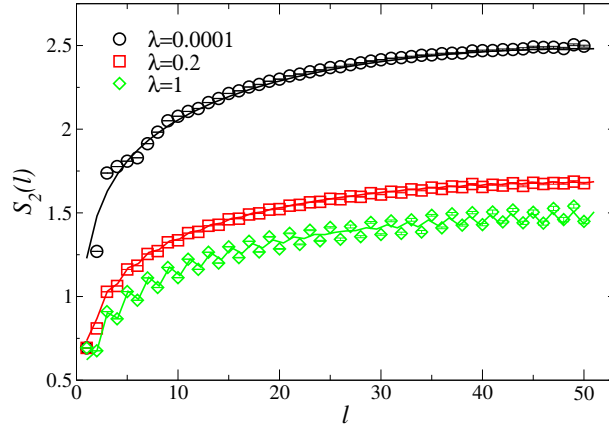


Figure 5.6: Second Rényi entanglement entropy calculated by QMC for AP states. The solid lines are fits done by the scaling function in Eq. (5.16). The oscillation increases with increasing  $\lambda_c$ .

different nonuniversal constants  $d_2$ . The fitting function can be written as

$$F(l) = \frac{c}{4} \ln\left[\frac{L}{\pi} \sin\left(\frac{\pi l}{L}\right)\right] + \sum_{i=1}^M d_2^i, \quad (5.17)$$

where  $M$  is the number of different sizes. The fitting results will be discussed in the following subsection.

### 5.3.2 Results

In this subsection, we present our results of the second REE of AP states. Because of the periodic condition, the second half of the  $S_2$  is the mirror image of the first half. Therefore, for system with length  $L$ , the  $S_2$  is calculated with the subsystem ranging from 1 to  $L/2$  (the half range of the system) at each critical point  $(K_c, \lambda_c)$ . A few examples are illustrated in Fig. 5.6. In AP states, strong oscillations are observed when  $\lambda_c$  is large, in which a strong VBS state is easily obtained close to the critical points.

By the fitting method we described above, we have successfully captured these oscillations by Eq.(5.16), as shown in Fig. 5.6. These oscillations have also been observed in 1D spin chains with open boundary condition [159, 162], some cases with PBC in higher order REE [158, 160], and in 2D RVB spin liquids [40]. In our case, when the short-bond

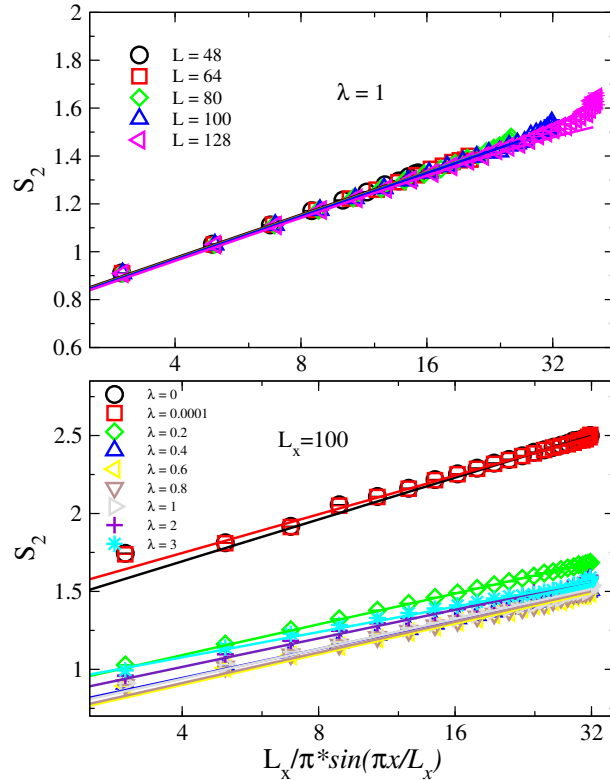


Figure 5.7: Second Rényi entropy versus the chord length  $[L_x/\pi \sin(\pi l/L_x)]$  when  $l$  is an even number. Solid lines are fitting lines in the form of Eq.(5.14). In the top panel, all fits are done together with the same central charge  $c = 1.04(1)$  and different  $d_2$  on different sizes at  $\lambda = 1$ . In the lower panel, the fitting function works well for all  $\lambda$ , with different  $c$  and  $d_2$  values. All  $c$  values are plotted in Fig. 5.8.

amplitude  $\lambda$  is small and the system inclines more to the AFM order, the oscillation can be ignored. However, when  $\lambda$  is big and system is prone to VBS order, oscillations are strong. Similar to the 2D RVB spin liquid study [40], where the dimer order parameter decays in the form of a power-law, when  $\lambda$  is large in AP states, we have strong  $S_2$  oscillations with the power-law decaying dimer order parameter as well. This oscillation might be caused by the quasi-dimer-order in critical states (i.e., very slowly decaying power-law form), which might be related to the dimension of energy operator as stated in Ref. [158].

We also plotted the upper branches of the  $S_2$  oscillation, together with fitting lines produced by Eq.(5.17) in Fig. 5.7. The top panel of Fig. 5.7 shows that there is no explicit

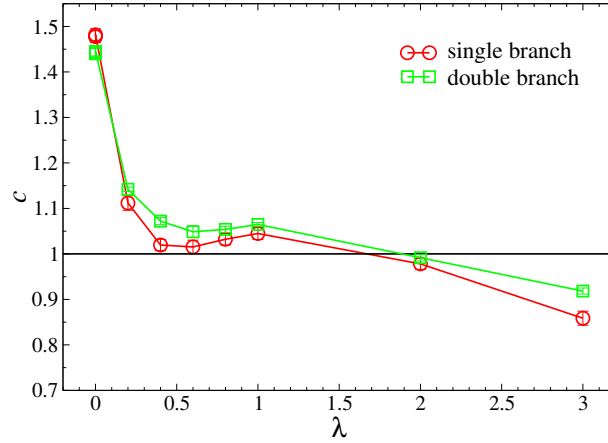


Figure 5.8: Central charge values versus the short-bond amplitude  $\lambda$ . The  $c$  values calculated from single-branch fittings are represented by red circles, and  $c$  values calculated from double-branch fittings are shown in green squares. Both values agree with each other within error bars. We find  $c = 1$  for  $\lambda > 0.2$ , and  $c > 1$  for  $\lambda \leq 0.2$ . When  $\lambda$  is near zero,  $c \approx 3/2$ .

size-dependence of the slope of single branches of  $S_2$ , therefore it is more efficient to fit all data with one fixed  $c$  and varying constant parameters  $d_2$  at the same time. The fitting results for several critical amplitudes for  $L = 100$  chain are shown in the lower panel of the Fig. 5.7.

By our fitting schemes described above for both the whole region (double branches) and the single branch of REE, we can extract the central charge  $c$  independently from each scheme. The  $c$  values are plotted in Fig. 5.8, with red-circle markers from the double-branch fittings and green-square markers from single-branch fittings respectively. The two fitting schemes give similar  $c$  values. We observe two main regions from this graph: 1. For  $\lambda \leq 0.2$ ,  $c > 1$ ; in particular, when  $\lambda \approx 0$ ,  $c \approx 3/2$ , which remarkably has the same value as the AFM model given by spin-1 Fateev-Zamolodchikov quantum chain [158] and 1D coupled dipolar boson tubes [163], 2. For  $\lambda > 0.2$ , the  $c$  values stay around 1, which is the same value as the Heisenberg  $S = 1/2$  chain. For very large  $\lambda$ , it is not clear to us if  $c = 1$  still holds true. In the large  $\lambda$  region, the accuracy of the measurement is affected severely by the noisy data, therefore the  $c$  value extracted is not very reliable there. Based on our results and by the fact there are known  $(1+1)$  CFTs with  $c = 1$  and  $c = 3/2$ , we conjecture that  $c = 3/2$  for  $\lambda$

exactly 0, and  $c = 1$  for  $\lambda > 0$ , i.e., there is a discontinuous jump in  $c$ . The rapid cross-over seen in Fig. 5.8 is most likely caused by effects of finite size and limited precision of the data. We also want to address the relation between  $c$  values and continuously varying critical exponents in our studies. It was first expected that the continuously varying exponents only exist at  $c = 1$  [164]. Later on, Cardy pointed out in Ref. [165] that though  $c = 1$  is the most natural case for continuously varying critical exponents, it is also possible to have the same continuously changing exponents under certain complicated situations when  $c > 1$ . Based on our findings here,  $c = 1$  still appears most likely for the 1D AP states, except at a special point with  $c = 3/2$ . Clearly, it would be good to repeat these calculations with larger systems in the future.

## 5.4 Summary and future work

In conclusion of this chapter, we have discussed 1D AP states and associated quantum phase transitions. VBS states appear naturally within the standard 1D AP states, and we have here characterized the continuous AFM-VBS transition in such a class of states with amplitudes decaying as a power-law of the bond length. We have obtained a group of continuously changing critical exponents by tuning two amplitudes, i.e.,  $\kappa$  the exponent of the power-law decaying form of amplitudes with  $r > 1$ , and  $\lambda$ , the amplitude at  $r = 1$ , at the critical points of AFM-VBS phase transitions. We further use the central charge  $c$  measured from Rényi entanglement entropy to classify the 1D critical AP states. We find two classes of AP states: AP states with  $\lambda > 0.2$  correspond to  $c = 1$  class, which has the same  $c$  value as the Heisenberg model; when  $\lambda \leq 0.2$ , especially at special points when  $\lambda \approx 0$ , AP states fall into the  $c = 3/2$  category, to which the AFM model in spin-1 Fateev-Zamolodchikov quantum chain belong. However, this conjecture might not be relevant since the underlying Hamiltonian might have the long-range interaction as we have the AFM order in 1D spin system.

Nevertheless, for future applications, it will be interesting to use the 1D AP states as initial states to search for ground states of the corresponding Hamiltonians (with the same

c) and check the convergence via variational MC algorithms. In more versatile generalizations of AP states—the *correlated amplitude product* (CAP) states—interesting quantum phase transitions from AFM state into non-magnetic VBS and spin liquid states have been detected [166]. In order to find a good ansatz to study interesting 2D physics, it is worth carrying out the classification of 2D CAP states via the calculation of the REE as well.

# Chapter 6

## Conclusion

This thesis is dedicated to studying the quantum criticality in low-dimensional quantum spin systems, which is an important research area in strongly-correlated systems.

### 6.1 Summary of highlights

Inspired by the interesting deconfined quantum criticality (DQC) theory that predicts the deconfinement of spinons at certain critical points, I developed a technique to quantitatively define the  $S = 1/2$  emergent excitation spinons at quantum phase transitions (QPTs) in quantum spin models. Though the method only works with the valence-bond basis, I have illustrated that the measured spinon size  $\lambda$  and confinement length  $\Lambda$  are inherited in the spin-spin correlation functions as well. Therefore, these two lengths appear to be basis-independent physical observables. My test results in 1D have demonstrated that, spinons are not well-defined in the Néel states, marginally-defined at the critical point and well-defined in the valence-bond solid state, which agree well with theoretical expectations. The main purpose of this work is to test the spinon deconfinement in the 2D AFM—VBS phase transition, which violates the transitional Landau-Ginzburg-Wilson theory. I have successfully demonstrated that spinons are deconfined in 1D spin systems. I have also observed that spinons become confined in the dimerized 1D spin chain or ladder systems. In 2D system, by simulating the  $J - Q_3$  model, which holds the AFM to VBS QPT with the spontaneous

symmetry broken, clear features of deconfinement at zero temperature were not observed. My results have indicated that, due to the weak interaction caused by the emergent  $U(1)$  field at the critical point, spinons have an effective attractive potential binding them weakly to each other. At the finite energy and temperature, a clearer observation of deconfinement are expected.

Resonating-valence-bond spin liquids are another important research focus of this thesis. RVB spin liquids have been drawing much attention for decades because of their exotic physical properties and their potential to explain the cuprate high-temperature superconductors with doping. As a pioneering work, I conducted a comprehensive study of RVB spin liquids with both the nearest bonds and long bonds. Together with a parallel work done by Albuquerque and Alet [46], RVB spin liquids are classified as quantum critical VBS states after our studies. In addition, together with collaborators, I also found a plausibility that the quantum RVB states could be mapped to classical dimer models. Our hypothesis was later successfully proved by the Damle group using a direct microscopic mapping [167].

As a generalized form of valence-bond states, amplitude product states are VB states with adjustable wave-function expansion coefficients. In this thesis work, I studied phase transition in this class of states by tuning parameters and found a transition from AFM order to VBS order. I also implemented the entanglement-entropy calculation for AP states, and measured the central charge for several critical points and classified the universal groups of these AP states for future use, e.g. constructing initial ground states for certain Hamiltonians in variational methods.

## 6.2 Future prospects

The  $J$ - $Q$  model is a simple “toy model” with a lot of physics to explore. Though there is no material directly related to this model, there might be in the future (e.g., in implementations of Hamiltonians with ultracold atoms in optical lattices). As a next step it will be very interesting to study the hole-doped versions of the model in the context of high- $T_c$  superconductivity. Besides that,  $J$ - $Q_3$  model itself plays a significant role in fundamental theoretical

studies. The  $J$ - $Q$  model might provide insightful predictions of physical properties to real magnetic materials, especially those that undergo unconventional phase transitions. And also, it will be worth seeing some dynamic properties of spinons in deconfined QPT, which might provide many new perspectives to the study of the theory. In addition, a Higgs boson mode should be observed in the excitation spectrum of the  $J$ - $Q$  model in the AFM state close to the critical point [168], and this mode should be interacting with the emergent gauge field from the VBS side and make another mass (gap) visible. Investigating these phenomena are very interesting and can serve well to connect condensed matter physics to high energy theories.

In addition, in the thesis I only carried out the entanglement-entropy calculations for 1D spin states. It will be interesting to study entanglement-entropy in 2D correlated AP states as well [166]. Combined with the conformal field theory and a variety of spin models, the measurement of entanglement can be applied further to study the universal class and the hidden order (i.e. topological order) of critical states, and even for detecting new properties of ordered states (e.g, VBS states).

# Appendices

# Appendix A

## Four-spin correlators in the valence-bond basis

In this appendix we work out the loop expression for four-spin correlators, analogous to the well-known two-spin expression (2.12).

It is useful to consider the singlet projectors

$$C_{ij} = -(\mathbf{S}_i \cdot \mathbf{S}_j - \frac{1}{4}). \quad (\text{A.1})$$

When acting on a valence bond, this operator is diagonal with eigenvalue 1. Denoting a singlet on sites  $a$  and  $b$  as  $(a, b)$ , we have

$$C_{ab}(a, b) = (a, b), \quad (\text{A.2})$$

whereas acting on a pair of different valence bonds leads to a simple reconfiguration of those bonds, e.g.,

$$C_{bc}(a, b)(c, d) = \frac{1}{2}(c, b)(a, d), \quad (\text{A.3})$$

$$C_{bd}(a, b)(c, d) = \frac{1}{2}(a, c)(b, d), \quad (\text{A.4})$$

which can be shown easily by going back to the basis of  $\uparrow$  and  $\downarrow$  spins. Note the order of the indices within the singlets in (A.3), which reflects consistently the chosen convention in the valence-bond state definition (2.1) when the sites  $a, c$  are on sublattice  $A$  and  $b, d$  on sublattice  $B$ . We will also have to consider operations on two spins belonging to the same

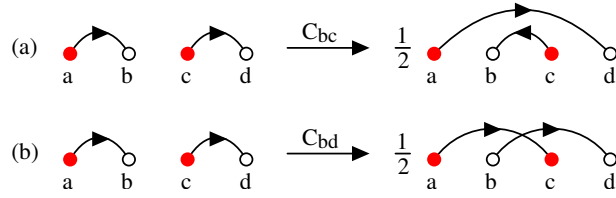


Figure A.1: Action of a singlet projection operator in two different cases; (a) when the sites  $b, c$  are on different sublattices and (b) when  $b, d$  belong to the same sublattice. The arrows indicate the order of the spins in a singlet;  $(a, b) = (|\uparrow_a \downarrow_b\rangle - |\downarrow_a \uparrow_b\rangle)/\sqrt{2}$ , and, in the case of spins on different sublattices, conforms with the definition (2.1) of bipartite valence bond states.

Figure A.2: Illustration of the equivalence (A.5), due to overcompleteness, between a state formed by two non-bipartite valence bonds and a superposition of two states involving only bipartite bonds.

sublattice, as in (A.4). We have not specified a convention for the order of the spins in singlets formed between two spins on the same sublattice, therefore, it is important to keep track of the signs, which depends on the order in which the singlets are written.

Figure A.1 illustrates the two different types of singlet projector outcomes in Eq. (A.3) and Eq. (A.4). In Fig. A.1(a), both the initial and the final bond pairs are bipartite whereas in Fig. A.1(b) the bonds after the operator has acted are non-bipartite. The non-bipartite bonds do not belong to the restricted basis of bipartite valence-bond basis in which we normally work. However, when generating non-bipartite bonds such as this (which can happen in the course of calculations), we can always rewrite them in terms of bipartite bonds. One can easily verify the following equivalence between valence bond pairs;

$$(a, c)(b, d) = (a, b)(c, d) - (a, d)(c, b), \quad (\text{A.5})$$

which is illustrated in Fig. A.2. This relationship is particularly useful when sites  $a, c \in A$  and  $b, d \in B$ , but it of course holds irrespective of sublattices.

As in (2.11), we can take advantage of the spin-rotational symmetry also when consid-

ering a four-spin correlation function, writing the corresponding matrix element as

$$\langle V_\beta | (\mathbf{S}_k \cdot \mathbf{S}_l)(\mathbf{S}_i \cdot \mathbf{S}_j) | V_\alpha \rangle = 3 \langle V_\beta | S_k^z S_l^z (\mathbf{S}_i \cdot \mathbf{S}_j) | V_\alpha \rangle. \quad (\text{A.6})$$

Note, however, that we cannot further reduce this expression to a correlation function involving only  $z$ -spin components, because if  $\gamma \neq z$ ,

$$\langle V_\beta | S_k^z S_l^z S_i^\gamma S_j^\gamma | V_\alpha \rangle \neq \langle V_\beta | S_k^z S_l^z S_i^\gamma S_j^\gamma | V_\alpha \rangle. \quad (\text{A.7})$$

It is easy to see that the matrix element (A.6) is non-zero only if all four indices  $i, j, k, l$  belong to the same loop, or if there are two indices in each of two loops. To carry out the calculations for these cases, it is convenient to make use of the singlet projection operator (A.1) and write the matrix element as

$$\begin{aligned} \langle V_\beta | S_k^z S_l^z (\mathbf{S}_i \cdot \mathbf{S}_j) | V_\alpha \rangle = \\ \frac{1}{4} \langle V_\beta | S_k^z S_l^z | V_\alpha \rangle - \langle V_\beta | S_k^z S_l^z C_{ij} | V_\alpha \rangle. \end{aligned} \quad (\text{A.8})$$

We only go through the calculation in detail for the case where all four indices belong to the same loop, which is the most complicated situation.

The procedure is illustrated in Fig. A.3. Acting first with the singlet projector  $C_{ij}$ , the loop is split into two separate loops if  $i, j$  are on different sublattices, as shown in Figs. A.3(a) and A.3(b). If these sites are on the same sublattice, as in Fig. A.3(c), the loop instead becomes “twisted” by two non-bipartite bonds. This loop can be re-cast in terms of two different contributions containing only bipartite bonds, by using the valence-bond equality illustrated in Fig. A.2. In each case, after  $C_{ij}$  has acted, we can return to the spin representation of the valence bonds and evaluate the average of the remaining operator  $S_k^z S_l^z$  exactly as we did for the two-spin correlation function. Here the result depends on whether  $k, l$  are in the same loop (giving a non-zero correlation) or different loops (giving a zero average) after the loop-splitting with  $C_{ij}$  has been enacted; these two different cases are illustrated in Fig. A.3(a) and A.3(b) for the case  $i, j$  in different sublattices [while for  $i, j$  on the same sublattice, Fig. A.3(c) only shows the case of  $k, l$  in different parts of the

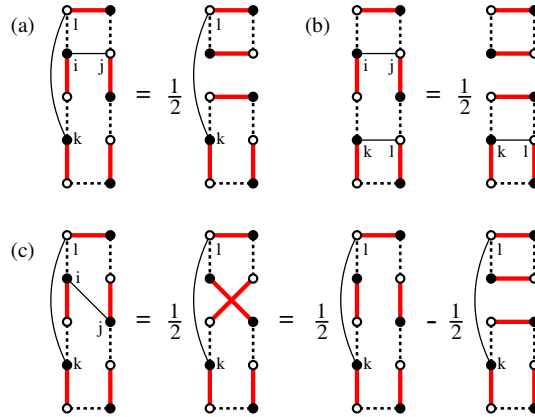


Figure A.3: Operations for evaluating the four-spin matrix element  $\langle V_\beta | (\mathbf{S}_k \cdot \mathbf{S}_l) (\mathbf{S}_i \cdot \mathbf{S}_j) | V_\alpha \rangle$  when all the sites  $i, j, k, l$  are in the same loop of the transition graph. The thin lines connecting labeled sites refer to the operator components  $S_k^z S_l^z$  and  $C_{ij}$  in (A.8). The solid and dashed bonds belong to  $|V_\alpha\rangle$  and  $\langle V_\beta|$ , respectively.

split loop]. In all cases, the matrix element ratio  $\langle V_\beta | S_k^z S_l^z C_{ij} | V_\alpha \rangle / \langle V_\beta | V_\alpha \rangle$  is now easy to compute using Fig. A.3 and keeping in mind that an increased number of loops after a split by  $C_{ij}$  increases the corresponding matrix element by a factor 2 according to the loop expression (2.6) for the overlap. The four-spin correlation can then be extracted using Eqs. (A.6) and (A.8).

In order to write the final result in a compact unified form for all the different cases, it is useful to introduce the concept of *subloops* with respect to the operator  $C_{ij}$  of a loop containing sites  $i, j$ , or  $(i, j)$ -subloops. As seen in Fig. A.3, regardless of whether  $i, j$  are on the same or different sublattices, the loop is split in the same way by  $C_{ij}$  in all cases where such split loops appear. This can be formalized by the following convention: The splitting of a loop into  $(i, j)$ -subloops is accomplished using the bonds in the ket  $|V_\alpha\rangle$  (the solid bonds in Fig. A.3, on which  $C_{ij}$  acts), i.e., the two  $V_\alpha$ -bonds on which  $i, j$  are located are those that are reconfigured in such a way that the loop splits into two. The subloops then always contain only bipartite bonds. This definition is illustrated in Fig. A.4. We also introduce a symbol to distinguish between the cases of  $k, l$  in the same subloop or different

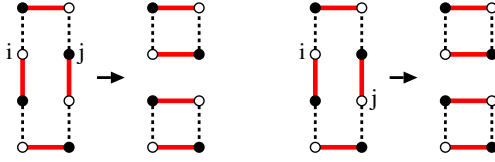


Figure A.4: Subloops of a valence-bond loop with respect to two sites  $i, j$ . The “cuts” splitting the loop into subloops are at the solid bonds connected to  $i$  and  $j$  (which belong to the ket  $|V_\alpha\rangle$ ; the state on which  $C_{ij}$  acts), irrespective of the two possible locations of  $i, j$  within these bonds. When  $i, j$  are sites in the same bond in  $|V_\alpha\rangle$ , there is only a single subloop (the whole loop).

subloops;

$$\delta_{ij}^{kl} = \begin{cases} 0, & \text{for } k, l \text{ in the same } (i, j)\text{-subloop,} \\ 1, & \text{for } k, l \text{ in different } (i, j)\text{-subloops.} \end{cases} \quad (\text{A.9})$$

If  $i, j$  are on the same bond of  $|V_\alpha\rangle$ ,  $C_{ij}$  does not change the loop and there is then only a single subloop (the intact original loop) and  $\delta_{ij}^{kl} = 0$  for all  $k, l$ .

The remaining cases of non-zero four-spin matrix elements involve two loops (with two indices in each loop). These calculations are easier than the case of all indices in the same loop, because there are no subloops to consider, and we just list the results. The full final result for all non-zero four-spin matrix elements is given in the main text as Eq. (2.15).

Note that whereas the sign of the two-spin correlation (2.12) is always dictated by the staggered phase factor, the sign of the four-spin correlation is different from the four-site staggered phase  $\phi_{ij}\phi_{kl}$  if all the indices are in the same loop and  $k, l$  belong to different  $(i, j)$ -subloops.

The concept of subloops may seem unnecessarily complicated in the definition of  $\delta_{kl}^{ij}$  in (A.9), since this number (0 or 1) is essentially also determined by the order in which the indices  $i, j, k, l$  appear when traversing a loop. If only one of the indices  $k, l$  appear between  $i, j$ , then, in most cases,  $k, l$  are in different subloops and  $\delta_{kl}^{ij} = 1$ . There are, however, special cases where the definition based on the order of indices is ambiguous, e.g., when they are all on the same valence bond in the ket  $|V_\alpha\rangle$ . In that case,  $k, l$  are in the same subloop and  $\delta_{kl}^{ij} = 0$ , as also explained in Fig. A.4.

## Appendix B

# Calculations based on height representation

Any *complete* covering of a bipartite planar lattice (such as the square lattice) by dimers can be mapped into a configuration of “heights” representing a kind of interface model. Often, the ensemble weighting corresponds to the “rough” phase of the interface. In this case, many statistical properties may be derived from a simple (Gaussian) classical field theory in terms of the coarse-grained height function, using the “Coulomb-gas” formalisms introduced in the Kosterlitz-Thouless theory of the two-dimensional XY model [169, 170]. Bipartite dimer coverings are a subset of a larger class of “height” models treated by this formalism, which also include random-tiling quasicrystals [139, 140].

The CDM is known to be in this “rough” phase. In the case of the RVB wave function, for which this property had not been known, it is shown in this paper that all statistical behaviors are consistent with a rough height model. It should be emphasized that this is an emergent behavior, since there is no exact way to map spin states to dimer coverings (the dimers to spins mapping is not invertible). We might hypothesize the existence of some hidden, nonlocal way to define winding numbers and perhaps height fields from the spins; however, the nonzero overlap between configurations in different winding-number sectors (see Fig. 4.3) shows that there can not be an exact mapping of that sort.

The starting point of the height treatment is that the probability of a (coarse-grained)

height field  $\{\bar{h}(\mathbf{r})\}$  is given by  $\exp[-F_{\text{tot}}(\{\bar{h}(\mathbf{r})\})]$ , where

$$F_{\text{tot}} = \int d^2\mathbf{r} \frac{1}{2} K |\nabla \bar{h}(\mathbf{r})|^2. \quad (\text{B.1})$$

We here study various consequences following from this.

## B.1 Relation of height field and dimer operators

There are two closely related ways to define a height function, for a dimer model, as laid out in Ref. [136]. The microscopic height  $h(\mathbf{r})$  is defined on dual vertices (centers of plaquettes); we set

$$\begin{aligned} h(x + \frac{1}{2}, y + \frac{1}{2}) - h(x - \frac{1}{2}, y + \frac{1}{2}) \\ = (-1)^{x+y} [4n_y(x, y) - 1], \end{aligned} \quad (\text{B.2a})$$

$$\begin{aligned} h(x + \frac{1}{2}, y + \frac{1}{2}) - h(x + \frac{1}{2}, y - \frac{1}{2}) \\ = (-1)^{x+y} [4n_x(x, y) - 1]. \end{aligned} \quad (\text{B.2b})$$

Thus  $h$  takes a step  $\pm 3$  across a dimer, or  $\mp 1$  across an unoccupied bond, where the sign alternates between even and odd vertices of the lattice. If one takes four steps around a vertex, one crosses a dimer once and an unoccupied bond three times such that the net difference is zero, ensuring a well-defined height field.

A second, locally averaged height function  $\bar{h}(x, y)$  is defined on the original vertices, being the mean of  $h$  on the four surrounding plaquettes. [Note the locally averaged  $\bar{h}(x, y)$  is not quite identical to the fully coarse-grained height function assumed in the field theory, although we use the same notation  $\bar{h}(\mathbf{r})$ .] This  $\bar{h}(x, y)$  is uniform in any one of the four special domains in which the dimers are aligned on opposite sites of plaquettes; it shifts by one unit on crossing a domain wall to the next domain. A change of  $\pm 4$  in  $\bar{h}$  brings us back to the same domain.

Thus, the dimer occupation can be written as a period-four function of the local height

variable,

$$n_x(\mathbf{r}) = \frac{1}{2} \left[ \cos\left(\frac{2\pi\bar{h}}{4}\right)^2 + (-1)^x \cos\left(\frac{2\pi\bar{h}}{4}\right) \right], \quad (\text{B.3a})$$

$$n_y(\mathbf{r}) = \frac{1}{2} \left[ \sin\left(\frac{2\pi\bar{h}}{4}\right)^2 + (-1)^y \sin\left(\frac{2\pi\bar{h}}{4}\right) \right]. \quad (\text{B.3b})$$

The configurations with a given winding number may be visualized as fluctuating domains with smoothed domain walls. For winding number  $W = (W_x, 0)$ , a net number of domain walls  $4W_x$  must be crossed as the system is traversed in the  $x$  direction. There is no long-range dimer order, so the domain walls thereby enforced are delocalized; indeed, in a snapshot of the configuration, they are lost in the dense array of random domain walls which are part of the inherent fluctuations even in the  $W = (0, 0)$  sector.

## B.2 Effects of long dimers

In the present simulations, sometimes dimers are permitted (both in CDM and RVB models) between sites separated by a  $(2, 1)$  type vector with a fugacity  $Z_2$ . This requires us to modify the height construction. Say this dimer extends from  $(0,0)$  to  $(2,1)$ . The height changes across the lattice edges  $(0,0)$ – $(1,0)$  and  $(1,1)$ – $(2,1)$  as if there were ordinary dimers occupying both edges (i.e.  $-1$  times the height change if those edges were vacant.) As for the lattice edge  $(1,0)$ – $(1,1)$  bisected by the long dimer, the height change is  $+5$  times the height change the vacant edge would have had. Around the vertex  $(1,0)$  or  $(1,1)$ , the net height changes are  $3 + 3 - 5 - 1 = 0$ , showing the modified construction is well defined.

It can be seen that long dimers allow larger differences in height between adjacent sites. In the coarse-grained picture this means that height gradients are penalized less and thus  $K$  is decreased. Indeed, it was observed in previous work [66] that in the CDM when *only* long dimers are present,  $K$  is reduced by a factor of  $2/9$ .

## B.3 Dimer correlations: dipolar term

It seems as if (B.2) and (B.3) express contradictory relations between the height field and the dimer configuration. The proper resolution is that the dimer field has two slowly varying

parts that are modulated in different ways with respect to the lattice,

$$n_x(x, y) - \frac{1}{4} \approx (-1)^{x+y} \frac{d\bar{h}}{dy} + \frac{(-1)^x}{2} \cos\left(\frac{2\pi\bar{h}}{4}\right), \quad (\text{B.4a})$$

$$n_y(x, y) - \frac{1}{4} \approx (-1)^{x+y+1} \frac{d\bar{h}}{dy} + \frac{(-1)^y}{2} \sin\left(\frac{2\pi\bar{h}}{4}\right), \quad (\text{B.4b})$$

which is equivalent to Eq. (2.4) of Ref. [132]. It turns out that the  $n_x$ - $n_x$  dimer occupation correlation, as a function of displacement  $\mathbf{r} = (x, y)$ , breaks up into two slowly decaying terms,  $D_{xx}(\mathbf{r}) = D_{xx}^{\text{dip}}(\mathbf{r}) + D_{xx}^{\text{crit}}(\mathbf{r})$ , which are due to the two kinds of terms in Eqs. (B.4).

Consider the first kind of term. Equation (B.1) implies, for the Fourier transform of the height field,  $\langle |\tilde{h}(\mathbf{q})|^2 \rangle \approx 1/K|\mathbf{q}|^2$  for small wavevectors  $\mathbf{q}$ . Combining with the  $\bar{h}$  gradient terms in (B.4), we find

$$S(\mathbf{Q} + \mathbf{k}) \approx \frac{k_y^2}{K|\mathbf{k}|^2} \quad (\text{B.5})$$

for the  $x$ -dimer structure factor near  $\mathbf{Q} = (\pi, \pi)$ . Taking the Fourier transform of (B.5) gives the (two-dimensional) pseudo-dipolar correlations

$$D_{xx}^{\text{dip}}(\mathbf{r}) \approx (-1)^{x+y} \text{Const} \frac{x^2 - y^2}{2\pi K |\mathbf{r}|^4}. \quad (\text{B.6})$$

The radial dependence of this is  $1/r^2$  in any direction, irrespective of the value of  $K$ .

## B.4 Dimer correlations: Critical term

We now turn to the second kind of term in Eqs. (B.4), the terms periodic in  $\bar{h}$ . By a calculation standard in height-model literature [136, 138], they imply the Coulomb gas (critical) term,

$$D_{xx}^{\text{crit}}(\mathbf{r}) \propto \frac{(-1)^x}{|\mathbf{r}|^\alpha}, \quad (\text{B.7})$$

where

$$\alpha = \frac{(2\pi/4)^2}{2\pi K} \equiv \frac{\pi}{8K}. \quad (\text{B.8})$$

It is a peculiarity of the CDM, with nearest-neighbor dimers and equally weighted configurations, that  $\alpha = 2$ . Thus *both* terms have the same decay exponent and in fact they cancel exactly on certain sites. Modifying the relative weighting of dimer configurations normally changes  $\alpha$ . If  $\alpha < 1/4$ , the height configuration locks into a flat state (roughening transition) which means that the dimers lock into a long-range ordered state. However, in this study,  $\alpha$  is reduced from the CDM value of 2 by a relatively modest amount.

The same kind of calculation implies that

$$D_{xx}^{\text{crit}}(L/2, L/2) \propto \frac{1}{L^\alpha}, \quad (\text{B.9})$$

with the same  $\alpha$  as in (B.7), but a different prefactor. Note that (so long as the elasticity is isotropic) the dipolar contribution  $D_{xx}^{\text{dip}}(\mathbf{r})$  is exactly zero along the lines  $x = \pm y$  (even as its asymptotic  $r$  dependence breaks down) and therefore does not contribute to  $D_{xx}(L/2, L/2)$ .

## B.5 Topological (monomer) defects and their correlations

If a site is uncovered, the height differences do *not* cancel in going around it, but change by  $b = \pm 4$  (where the sign depends on whether the vertex is even or odd). Such defects can only be created in pairs of opposite charge, and play the same role as vortices in the Kosterlitz-Thouless theory. The  $K$  values in our simulations are small enough that we are above the Kosterlitz-Thouless unbinding transition, i.e., if there were nonzero fugacity to have defects, they would destroy the critical state at sufficiently long length scales. However, the fugacity is in fact zero (except that in some simulations, one pair is inserted by hand as a probe).

The presence of a defect at (say) the origin enforces a background gradient in the height field with  $|\nabla \bar{h}| = b/2\pi r$ . When substituted into Eq. (B.1), that would give a logarithmically divergent total, except that the divergence gets cut off by another defect at distance  $R$ . The result is that the effective potential cost for the defects to be separated by  $R$  is  $(K/2\pi)b^2 \ln R$ , and the pair distribution is given by

$$M(R) \propto \frac{1}{R^\beta}, \quad (\text{B.10})$$

with

$$\beta = \frac{Kb^2}{2\pi} = \frac{8K}{\pi}, \quad (\text{B.11})$$

and in particular  $\beta = 1/2$  for the basic CDM.

## B.6 Sector probabilities

We now turn to the effects of enforcing net winding numbers  $W_x, W_y$ . This is equivalent to a boundary condition that  $\bar{h}(L, y) \equiv \bar{h}(0, y) + 4W_x$  and  $\bar{h}(x, L) \equiv \bar{h}(x, 0) + 4W_y$ . In light of Eq. (B.3), no discontinuity is implied in the actual dimer pattern, since that depends on  $\bar{h}(\mathbf{r})$  with period 4. It would be exactly analogous to enforcing, in an  $XY$  model, angle differences  $(2\pi W_x, 2\pi W_y)$  across the system.

Thus the effect of winding number  $(W_x, W_y)$  is to impose a uniform “background” height tilt  $(m_x, m_y) = 4(W_x, W_y)/L$ . We write

$$\bar{h}(\mathbf{r}) = m_x x + m_y y + \bar{h}'(\mathbf{r}), \quad (\text{B.12})$$

separating the height field into the background plus a (smaller) deviation  $\bar{h}'(\mathbf{r})$  that satisfies periodic boundary conditions.

If we substitute the free energy Eq. (B.1) into Eq. (B.12), we see that

$$F_{\text{tot}}(\{\bar{h}\}) = F_{\text{tot}}(\{\bar{h}'\}) + \Delta F(W_x, W_y), \quad (\text{B.13})$$

where

$$\Delta F(W_x, W_y) = \frac{1}{2}KL^2(m_x^2 + m_y^2) = 8K(W_x^2 + W_y^2). \quad (\text{B.14})$$

Since  $F_{\text{tot}}$  in (B.13) is exactly the same function as before, it follows that when we integrate over all configurations of  $\{\bar{h}'(\mathbf{r})\}$  to obtain the partial partition function  $Z(W_x, W_y)$  for a given sector,  $Z(W_x, W_y) = Z(0, 0) \exp[-\Delta F(W_x, W_y)]$ . We conclude that the relative probabilities of different sectors are given by

$$P(W_x, W_y) = P(0, 0) e^{-8K(W_x^2 + W_y^2)}. \quad (\text{B.15})$$

In checking the normalization of  $P(W_x, W_y)$ , it should be remembered that e.g. the (1,0) sector is fourfold degenerate [the possible winding numbers are  $(\pm 1, 0)$  and  $(0, \pm 1)$ ], as are the (1,1) and (2,0) sectors.

## B.7 Correlation modulation due to winding number

To calculate the critical contribution in the presence of a background  $\bar{h}$  gradient associated with a winding number, we merely need to substitute Eq. (B.12) into Eqs. (B.4), remembering that the rightmost terms are the ones contributing to the desired correlation. The result is that we get the correlation due to the  $\bar{h}'$  field (i.e. the same as before) times  $\cos[\frac{2\pi}{4}(m_x x + m_y y)]$ , where  $(x, y)$  is the vector connecting the two points. In other words,

$$D_{xx}^{\text{crit}}(\mathbf{r}; W) = D_{xx}^{\text{crit}}(\mathbf{r}; 0) \cos(\delta\mathbf{Q} \cdot \mathbf{r}), \quad (\text{B.16})$$

where  $D_{xx}^{\text{crit}}(\mathbf{r}; W)$  means  $D_{xx}^{\text{crit}}(\mathbf{r})$  given winding numbers  $W$ , and

$$\delta\mathbf{Q} \equiv \frac{2\pi}{4}(m_x, m_y) = 2\pi(W_x, W_y)/L. \quad (\text{B.17})$$

Since  $D_{xx}^{\text{crit}}(\mathbf{r}; 0)$  already includes a  $(-1)^x$  modulation, it follows that the structure factor singularity of  $D_{xx}^{\text{crit}}(\mathbf{r}; W)$  gets shifted to

$$\mathbf{Q} = (\pi, 0) \pm \delta\mathbf{Q}. \quad (\text{B.18})$$

## B.8 Anisotropic effects due to winding number

In a height model, the free-energy density is a function of  $\nabla\bar{h}(\mathbf{r})$  and its derivatives, satisfying all lattice symmetries. The free-energy density in Eq. (B.1) is the lowest term of its Taylor expansion in  $\nabla\bar{h}$ . The next terms consistent with the square lattice are quartic, thus, the free-energy density becomes

$$\begin{aligned} f(\nabla\bar{h}) = \frac{1}{2}K|\nabla\bar{h}|^2 &+ g_{11} \left[ \left(\frac{d\bar{h}}{dx}\right)^4 + \left(\frac{d\bar{h}}{dy}\right)^4 \right], \\ &+ 2g_{12} \left(\frac{d\bar{h}}{dx}\right)^2 \left(\frac{d\bar{h}}{dy}\right)^2. \end{aligned} \quad (\text{B.19})$$

If we insert Eq. (B.19) into Eq. (B.12) The effective free energy density to lowest order in  $\bar{h}'$  is

$$f = \frac{1}{2}K_x \left(\frac{d\bar{h}}{dx}\right)^2 + \frac{1}{2}K_y \left(\frac{d\bar{h}}{dy}\right)^2 + K_{xy} \left(\frac{d\bar{h}}{dx}\right) \left(\frac{d\bar{h}}{dy}\right), \quad (\text{B.20})$$

where

$$K_x \equiv K + 12g_{11}m_x^2 + 2g_{12}m_y^2, \quad (\text{B.21a})$$

$$K_y \equiv K + 12g_{11}m_y^2 + 2g_{12}m_x^2, \quad (\text{B.21b})$$

$$K_{xy} \equiv 4g_{12}m_x m_y. \quad (\text{B.21c})$$

The nonlinear terms of a background tilt were considered and measured from simulations in the quasicrystal random tiling context [140]. It is possible, in principle, to extract analytical expressions for the nonlinear terms from the exact solutions.

Next we consider how this modifies correlations. For simplicity, consider the case  $m_y = 0$ . We make a change of variables

$$x' \equiv \gamma x; \quad y' \equiv \gamma^{-1}y, \quad (\text{B.22})$$

where

$$\gamma \equiv (K_x/K_y)^{1/4}. \quad (\text{B.23})$$

In the new coordinates, the free energy density is

$$f = \frac{1}{2}K' \left[ \left(\frac{d\bar{h}'}{dx'}\right)^2 + \left(\frac{d\bar{h}'}{dy'}\right)^2 \right], \quad (\text{B.24})$$

with an effective stiffness  $K' \equiv \sqrt{K_x K_y}$ . In these new coordinates, Eq. (B.24) looks isotropic again and the same results must follow for the behavior of all correlations. In particular, the dimer and monomer correlation decay exponents,  $\alpha$  and  $\beta$ , depend on  $K'$  in the same way they previously did on  $K$ . In the general case that  $m_x m_y \neq 0$ , the effective stiffness is

$$K' \equiv \sqrt{K_x K_y - K_{xy}^2}. \quad (\text{B.25})$$

For small  $W/L$ , i.e. small  $(m_x, m_y)$ , this reduces in light of Eqs. (B.21) to  $K' \approx K + 96(g_{11} + g_{12})(W_x^2 + W_y^2)/L^2$ . Hence large  $L$ , and a winding number  $W$  the corrections to exponents scale the same way,  $\delta\alpha \sim \delta\beta \sim W^2/L^2$ .

Notice that the decay exponent is the same in all spatial directions. The way the anisotropy gets expressed in the correlations with variable exponents is that (e.g.) dimer correlations do not fall off exactly as  $1/r^\alpha$ , but rather as  $1/r'^\alpha$ , where  $r' \equiv \sqrt{\gamma^2 x^2 + \gamma^{-2} y^2}$ , and similarly for monomer pair separations. It would be interesting to see whether the anisotropy of *spin* correlations, as shown in Fig. 4.4, is expressed by the same ratio  $\gamma$ .

# List of Journal Abbreviations

AIP Conf. Proc	AIP Conference Proceedings
Ann. Phys	Annals of Physics
Ark. Mat. Astron. Fys	Arkiv for Matematik, Astronomi Och Fysik
Bull. Am. Phys. Soc	Bulletin of the American Physical Society
Eur. Phys. J. B	European Physical Journal B
Europhys. Lett	Europhysics Letters
JETP	Journal of Experimental and Theoretical Physics
J. Chem. Phys	Journal of Chemical Physics
J. Math. Phys	Journal of Mathematical Physics
J. Phys. A	Journal of Physics A
J. Phys. A: Math. Gen	Journal of Physics A: Mathematical and General

J. Phys. A: Math. Thoer	Journal of Physics A: Mathematical and Theoretical
J. Phys. : Cond. Mat	Journal of Physics: Condensed Matter
J. Phys. Rep	Physics Reports
J. Physique I	Journal de Physique I
J. Stat. Mech	Journal of Statistical Mechanics
J. Stat. Phys	Journal of Statistical Physics
Mater. Res. Bull	Materials Research Bulletin
Nature Mater	Nature Materials
Nucl. Phys. B	Nuclear Physics B
Philos. Mag	Philosophical Magazine
Phys. A: Math. Gen	Journal of Physics A: Mathematical and General
Phys. Rev	Physical Review
Phys. Rev. B	Physical Review B
Phys. Rev. Lett	Physical Review Letter

Proc. Roy. Soc

Proceedings of the Royal Society

Prog. Theor. Phys

Progress of Theoretical Physics

Rev. Mod. Phys

Review of Modern Physics

Z. Phys

Zeitschrift für Physik

# Bibliography

- [1] J. G. Bednorz, K. A. Müller, and Zeitschrift für. Possible high  $T_c$  superconductivity in the balacuo system. *Physik B*, 64, 1986.
- [2] P. W. Anderson. The resonating valence bond state in  $La_2CuO_4$  and superconductivity. *Science*, 235, 1987.
- [3] D. Dagotto and A. Moreo. Phase diagram of the frustrated spin-1/2 heisenberg anti-ferromagnet in 2 dimensions. *Phys. Rev. Lett*, 63, 1989.
- [4] H. J. Schulz, T. A. L. Ziman, and D. Poilblanc. Magnetic order and disorder in the frustrated quantum heisenberg antiferromagnet in two dimensions. *J. Physique I*, 6, 1996.
- [5] P. W. Anderson. Resonating valence bonds: A new kind of insulator? *Mater. Res. Bull*, 8, 1973.
- [6] Ch. Rüegg, B. Normand, M. Matsumoto, A. Furrer, D. F. McMorrow, K. W. Krämer, H. U. Güdel, S. N. Gvasaliya, H. Mutka, and M. Boehm. Quantum magnets under pressure: controlling elementary excitations in  $tlcucl_3$ . *Phys. Rev. Lett*, 100, 2008.
- [7] R. Coldea, D. A. Tennant, E. M. Wheeler, E. Wawrzynska, D. Prabhakaran, M. Telling, K. Habicht, P. Smeibidl, and K. Kiefer. Quantum criticality in an ising chain: experimental evidence for emergent  $E_8$  symmetry. *Science*, 327, 2010.

- [8] Y. Shimizu, H. Akimoto, H. Tsujii, A. Tajima, and Reizo Kato. Reentrant mott transition from a fermi liquid to a spin-gapped insulator in an organic spin-1/2 triangular-lattice antiferromagnet. *J. Phys: Cond. Mat*, 19, 2007.
- [9] Subir Sachdev. *Quantum Phase Transitions*. Cambridge University Press, Cambridge, UK, 1999.
- [10] S. L. Sondhi, S. M. Girvin, J. P. Carini, and D. Shahar. Continuous quantum phase transitions. *Rev. Mod. Phys*, 69, 1997.
- [11] L. D. Landau, E. M. Lifshitz, and E. M. Pitaevskii. *Statistical Physics*. Butterworth-Heinemann, New York, 1999.
- [12] K. G. Wilson and J. Kogut. The renormalization group and the  $\epsilon$  expansion. *J. Phys. Rep*, 12C, 1974.
- [13] Z. Y. Meng, T. C. Lang, S. Wessel, F. F. Assaad, and A. Muramatsu. Quantum spin liquid emerging in two-dimensional correlated dirac fermions. *Nature*, 464, 2010.
- [14] S. Sorella, Y. Otsuka, and S. Yunoki. Absence of a spin liquid phase in the hubbard model on the honeycomb lattice. *Nature Scientific Reports*, 2, 2012.
- [15] H.-C Jiang, H. Yao, and L. Balents. Spin liquid ground state of the spin-1/2 square  $J_1$ - $J_2$  heisenberg model. *Phys. Rev. B*, 86, 2012.
- [16] L. Wang, Z-C. Gu, F. Verstraete, and X-G. Wen. Spin-liquid phase in spin-1/2 square  $J_1 - J_2$  heisenberg model: A tensor product state approach. arXiv:1112.3331.
- [17] S. Yan, D. A. Huse, , and S. R. White. Spin-liquid ground state of the  $S = 1/2$  kagome heisenberg antiferromagnet. *Science*, 332, 2011.
- [18] T-H. Han, J. S. Helton, S. Chu, D. G. Nocera, J. A. Rodriguez-Rivera, C. Broholm, and Y. S. Lee. Fractionalized excitations in the spin-liquid state of a kagome-lattice antiferromagnet. *Nature*, 492, 2012.

- [19] S. Chakravarty, B. I. Halperin, and D. R. Nelson. Two-dimensional quantum heisenberg antiferromagnet at low temperatures. *Phys. Rev. B*, 39, 1989.
- [20] A. V. Chubukov, S. Sachdev, and J. Ye. Theory of two-dimensional quantum heisenberg antiferromagnets with a nearly critical ground state. *Phys. Rev. B*, 49, 1994.
- [21] A. W. Sandvik. Computational studies of quantum spin systems. *AIP Conf.Proc*, 1297, 2010. arXiv:1101.3281.
- [22] F. F. Assaad, M. Imada, and D. J. Scalapino. Quantum transition between an antiferromagnetic mott insulator and  $d_{x^2-y^2}$  superconductor in two dimensions. *Phys. Rev. Lett*, 89, 2002.
- [23] A. W. Sandvik, S. Daul, R. R. P. Singh, and D. J. Scalapino. Striped phase in a quantum xy model with ring exchange. *Phys. Rev. Lett*, 89, 2002.
- [24] A. W. Sandvik. Continuous quantum phase transition between an antiferromagnet and a valence-bond-solid in two dimensions; evidence for logarithmic corrections to scaling. *Phys. Rev. Lett*, 104, 2010.
- [25] R. K. Kaul and R. G. Melko. Large-n estimates of universal amplitudes of the  $CP^{N-1}$  theory and comparison with a  $S = 1/2$  square-lattice model with competing four-spin interactions. *Phys. Rev. B*, 78, 2008.
- [26] P. Coleman, C. Pepin, Q. Si, and R. Ramazashvili. How do fermi liquids get heavy and die? *J. Phys: Condens. Matt*, 13, 2001.
- [27] G. R. Stewart. Non-fermi-liquid behavior in d- and f -electron metals. *Rev. Mod. Phys*, 73, 2001.
- [28] T. Senthil, A. Vishwanath, L. Balents, S. Sachdev, and M. P. A. Fisher. Deconfined quantum critical points. *Science*, 303, 2004.
- [29] T. Senthil, L. Balents, S. Sachdev, A. Vishwanath, and M. P. A. Fisher. Quantum criticality beyond the landau-ginzburg-wilson paradigm. *Phys. Rev. B*, 70, 2004.

- [30] M. Levin and T. Senthil. Deconfined quantum criticality and néel order via dimer disorder. *Phys. Rev. B*, 70, 2004.
- [31] K. S. D. Beach and A. W. Sandvik. Some formal results for the valence bond basis. *Nucl. Phys. B*, 750, 2006.
- [32] L. Balents. Spin liquids in frustrated magnets. *Nature*, 464, 2010.
- [33] S. T. Bramwell and M. J. P. Gingras. Spin ice state in frustrated magnetic pyrochlore materials. *Science*, 294, 2001.
- [34] C. Castelnovo, R. Moessner, and S. L. Sondhi. Magnetic monopoles in spin ice. *Nature*, 451, 2008.
- [35] L. D. C. Jaubert and P. C. W. Holdsworth. Signature of magnetic monopole and dirac string dynamics in spin ice. *Nature physics*, 5, 2009.
- [36] X. G. Wen. *Quantum field theory of many-body systems*. Oxford University Press, New York, 2004.
- [37] F. Alet, A. M. Walczak, and M. P.A. Fisher. Exotic quantum phases and phase transitions in correlated matter. *Physica A*, 369, 2006.
- [38] N. Read and S. Sachdev. Large-n expansion for frustrated quantum antiferromagnets. *Phys. Rev. Lett*, 66, 1991.
- [39] Y. Tang and A. W. Sandvik. Confinement and deconfinement of spinons in two dimensions. *Phys. Rev. Lett*.
- [40] H. Ju, A. B. Kallin, P. Fendley, M. B. Hastings, and R. G. Melko. Entanglement scaling in two-dimensional gapless systems. *Phys. Rev. B*, 85, 2012.
- [41] A. W. Sandvik. Finite-size scaling and boundary effects in two-dimensional valence-bond solids. *Phys. Rev. B*, 85, 2012.

- [42] S-S. Gong, W. Zhu, D. N. Sheng, O. I. Motrunich, and M. P. A. Fisher. Plaquette ordered phase and quantum spin liquid in the spin-1/2  $j_1$ - $j_2$  square heisenberg model. arXiv:1311.5962.
- [43] D. S. Rokhsar and S. A. Kivelson. Superconductivity and the quantum hard-core dimer gas. *Phys. Rev. Lett*, 61, 1988.
- [44] J. Cano and P. Fendley. Spin hamiltonians with resonating-valence-bond ground states. *Phys. Rev. Lett*, 105, 2010.
- [45] Y. Tang, A. W. Sandvik, and C. L. Henley. Properties of resonating-valence-bond spin liquids and critical dimer models. *Phys. Rev. B*, 84, 2011.
- [46] A. F. Albuquerque and F. Alet. Critical correlations for short-range valence-bond wave functions on the square lattice. *Phys. Rev. B*, 82, 2010.
- [47] L. Amico, R. Fazio, A. Osterloh, and V. Vedral. Entanglement in many-body systems. *Rev. Mod. Phys*, 2008.
- [48] S. V. Isakov, M. B. Hastings, and R. G. Melko. Topological entanglement entropy of a bose-hubbard spin liquid. *Nature physics*, 2011.
- [49] H.-C. Jiang, Z. Wang, and L. Balents. Identifying topological order by entanglement entropy. *Nature physics*, 2012.
- [50] M. B. Hastings, I. González, A. B. Kallin, and R. G. Melko. Measuring renyi entanglement entropy in quantum monte carlo simulations. *Phys. Rev. Lett*, 104, 2010.
- [51] P. Calabrese and J. L. Cardy. Entanglement entropy and conformal field theory. *J. Phys. A: Math. Thoer*, 42, 2009.
- [52] J. Eisert, M. Cramer, and M. B. Plenio. Colloquium: Area laws for the entanglement entropy. *Rev. Mod. Phys*, 82, 2010.

- [53] S. Liang, B. Doucot, and P. W. Anderson. Some new variational resonating-valence-bond-type wave functions for the spin-1/2 antiferromagnetic heisenberg model on a square lattice. *Phys. Rev. Lett*, 61, 1988.
- [54] N. Metropolis, A. W. Rosenbluth, M. N. Rosenbluth, and A. H. Teller. Equation of state calculations by fast computing machines. *J. Chem. Phys*, 21, 1952.
- [55] N. Metropolis. The beginning of the monte carlo method. *Los Alamos Science*, 12, 1987.
- [56] M. H. Kalos and P. A. Whitlock. *Monte Carlo methods*. Wiley-VCH Verlag GmbH & Co, Weinheim, 2008.
- [57] R. P. Feynman. Atomic theory of the  $\lambda$  transition in helium. *Phys. Rev*, 91, 1953.
- [58] S. R. White, D. J. Scalapino, R. L Sugar, E. Y. Loh, J. E.Gubernatis, and R. T. Scalettar. Numerical study of the two-dimensional hubbard model. *Phys. Rev. B*, 40, 1989.
- [59] P. Henelius and A. W. Sandvik. Sign problem in monte carlo simulations of frustrated quantum spin systems. *Phys. Rev. B*, 62, 2000.
- [60] W. M. C. Foulkes. Quantum monte carlo simulations of solids. *Rev. Mod. Phys*, 73, 2001.
- [61] W. Marshall. Antiferromagnetism. *Proc. Roy. Soc. A*, 232, 1955.
- [62] B. Sutherland. Systems with resonating-valence-bond ground states: Correlations and excitations. *Phys. Rev. B*, 37, 1988.
- [63] B. Sutherland. Monte carlo investigation of the resonating-valence-bond ground state and a lattice statistical model. *Phys. Rev. B*, 38, 1988.
- [64] A. W. Sandvik and H. G. Evertz. Loop updates for variational and projector quantum monte carlo simulations in the valence-bond basis. *Phys. Rev. B*, 82, 2010.

- [65] D. H. Adams and S. Chandrasekharan. Chiral limit of strongly coupled lattice gauge theories. *Nucl. Phys. B*, 662, 2003.
- [66] A. W. Sandvik and R. Moessner. Correlations and confinement in nonplanar two-dimensional dimer models. *Phys. Rev. B*, 73, 2006.
- [67] N. Read and B. Chakraborty. Statistics of the excitations of the resonating-valence-bond state. *Phys. Rev. B*, 40, 1989.
- [68] L. Wang and A. W. Sandvik. Low-energy excitations of two-dimensional diluted heisenberg quantum antiferromagnets. *Phys. Rev. B*, 81, 2010.
- [69] A. Banerjee and K. Damle. Generalization of the singlet sector valence bond loop algorithm to antiferromagnetic ground states with total spin  $S_{tot} = 1/2$ . *J. Stat. Mech*, 2010.
- [70] N. V. Prokofév, B. V. Svistunov, and I. S. Tupitsyn. Exact, complete, and universal continuous-time worldline monte carlo approach to the statistics of discrete quantum systems. *Soviet Physics - JETP*, 87, 1998.
- [71] O. F. Syljuåsen and A. W. Sandvik. Quantum monte carlo with directed loops. *Phys. Rev. E*, 66, 2002.
- [72] L. D. Faddeev and L. A. Takhtajan. What is the spin of a spin wave. *Phys. Lett*, 85A, 1981.
- [73] F. M. D. Haldane. spinon gas description of the  $S = 1/2$  heisenberg chain with inverse-square exchange: Exact spectrum and thermodynamics. *Phys. Rev. Lett*, 66, 1991.
- [74] B. S. Shastry and B. Sutherland. Excitation spectrum of a dimerized next-neighbor antiferromagnetic chain. *Phys. Rev. Lett*, 47, 1981.
- [75] J. Van Kranendonk and J. H. Van Vleck. Spin waves. *Rev. Mod. Phys*, 30, 1958.

- [76] G. Müller, H. Thomas, H. Beck, , and J. Bonner. Quantum spin dynamics of the antiferromagnetic linear chain in zero and nonzero magnetic field. *Phys. Rev. B*, 24, 1981.
- [77] P. A. Lee. An end to the drought of quantum spin liquids. *Science*, 321, 2008.
- [78] Y. Tang and A. W. Sandvik. Method to characterize spinons as emergent elementary particles. *Phys. Rev. Lett*, 107, 2011.
- [79] H. Bethe. Zur theorie der metalle. i. eigenwerte und eigenfunktionen der linearen atomkette (on the theory of metals. i. eigenvalues and eigenfunctions of the linear atom chain). *Z. Physik*, 71, 1931.
- [80] A. Luther and I. Peschel. Calculation of critical exponents in two dimensions from quantum field theory in one dimension. *Phys. Rev. B*, 12, 1975.
- [81] J. des Cloizeaux and J. J. Pearson. Spin-wave spectrum of the antiferromagnetic linear chain. *Phys. Rev*, 128, 1962.
- [82] T. Yamada. Fermi-liquid theory of linear antiferromagnetic chains. *Prog. Theor. Phys*, 41, 1969.
- [83] M. B. Stone, D. H. Reich, C. Broholm, K. Lefmann, C. Rischel, C. P. Landee, and M. M. Turnbull. Extended quantum critical phase in a magnetized  $spin - 1/2$  antiferromagnetic chain. *Phys. Rev. Lett*, 91, 2003.
- [84] B. Lake, D. A. Tennant, C. D. Frost, and S. E. Nagler. Quantum criticality and universal scaling of a quantum antiferromagnet. *Nature Mater*, 4, 2005.
- [85] D. C. Dender, P. R. Hammar, D. H. Reich, C. Broholm, and G. Aeppli. Direct observation of field-induced incommensurate fluctuations in a one-dimensional  $S = 1/2$  antiferromagnet. *Phys. Rev. Lett*, 79, 1997.
- [86] M. Kenzelmann, Y. Chen, C. Broholm, D. H. Reich, and Y. Qiu. Bound spinons in an antiferromagnetic  $S = 1/2$  chain with a staggered field. *Phys. Rev. Lett*, 93, 2004.

- [87] B. Thielemann, Ch. Rüegg, H. M. Ronnow, A. M. Läuchli, J. S. Caux, B. Normand, D. Biner, K. W. Krämer, H. U. Güdel, J. Stahn, K. Habicht, M. Boehm, D. F. McMorrow, and J. Mesot. Bound spinons in an antiferromagnetic  $S = 1/2$  chain with a staggered field. *Phys. Rev. Lett*, 102, 2009.
- [88] Y. Zhou and P. A. Lee. Spinon phonon interaction and ultrasonic attenuation in quantum spin liquids. *Phys. Rev. Lett*, 106, 2011.
- [89] R. L. Doretto and M. Vojta. Quantum magnets with weakly confined spinons: Multiple length scales and quantum impurities. *Phys. Rev. B*, 80, 2009.
- [90] T. Giamarchi and H. J. Schulz. Correlation functions of one-dimensional quantum systems. *Phys. Rev. B*, 39, 1989.
- [91] I. Affleck, D. Gepner, H. J. Schulz, and T. Ziman. Critical behaviour of spin- $s$  heisenberg antiferromagnetic chains: analytic and numerical results. *J. Phys. A: Math. Gen*, 22, 1989.
- [92] S. Sanyal, A. Banerjee, and K. Damle. Vacancy-induced spin texture in a one-dimensional  $S = 1/2$  heisenberg antiferromagnet. *Phys. Rev. B*, 84, 2011.
- [93] S. Eggert. Numerical evidence for multiplicative logarithmic corrections from marginal operators. *Phys. Rev. B*, 54, 1996.
- [94] T. Giamarchi. (private communication).
- [95] N. D. Mermin and H. Wagner. Absence of ferromagnetism or antiferromagnetism in one- or two-dimensional isotropic heisenberg models. *Phys. Rev. Lett*, 17, 1966.
- [96] N. Laflorencie, I. Affleck, and M. Berciu. Critical phenomena and quantum phase transition in long range heisenberg antiferromagnetic chains. *J. Stat. Mech*, 2005.
- [97] F. D. M. Haldane. Continuum dynamics of the  $1 - D$  heisenberg antiferromagnet: identification with the  $O(3)$  nonlinear sigma model. *Phys. Lett. A*, 93, 1983.

- [98] F. D. M. Haldane. Nonlinear field theory of large-spin heisenberg antiferromagnets: semiclassically quantized solitons of the one-dimensional easy-axis néel state. *Phys. Rev. Lett*, 50, 1983.
- [99] B. Lake, A. M. Tsvelik, S. Notbohm, D. A. Tennant, T. G. Perring, M. Reehuis, C. Sekar, G. Krabbes, and B. Büchner. Confinement of fractional quantum number particles in a condensed-matter system. *Nature Physics*, 6, 2010.
- [100] T. Barnes, E. Dagotto, J. Riera, , and E. S. Swanson. Excitation spectrum of heisenberg spin ladders. *Phys. Rev. B*, 47, 1993.
- [101] N. Read and S. Sachdev. Spin-peierls, valence-bond solid, and nel ground states of low-dimensional quantum antiferromagnets. *Phys. Rev. B*, 42, 1990.
- [102] G. Murthy and S. Sachdev. Action of hedgehog-instantons in the disordered phase of the  $2 + 1$  dimensional  $CP^{N-1}$  model. *Nucl. Phys. B*, 344, 1990.
- [103] O. I. Motrunich and A. Vishwanath. Emergent photons and transitions in the  $O(3)$  sigma model with hedgehog suppression. *Phys. Rev. B*, 70, 2004.
- [104] F.-J. Jiang, M. Nyfeler, S. Chandrasekharan, and U.-J. Wiese. From an antiferromagnet to a valence bond solid: Evidence for a first order phase transition. *J. Stat. Mech*, 2008.
- [105] A.B. Kuklov, N.V. Prokofév, B.V. Svistunov, and M. Troyer. Deconfined criticality, runaway flow in the two-component scalar electrodynamics and weak first-order superfluid-solid transitions. *Ann. Phys*, 321, 2006.
- [106] A.B. Kuklov, M. Matsumoto, N.V. Prokofév, B.V. Svistunov, and M. Troyer. Deconfined criticality: Generic first-order transition in the  $SU(2)$  symmetry case. *Phys. Rev. Lett*, 101, 2008.
- [107] A. W. Sandvik. Evidence for deconfined quantum criticality in a two-dimensional heisenberg model with four-spin interactions. *Phys. Rev. Lett*, 98, 2007.

- [108] J. Lou, A. W. Sandvik, and N. Kawashima. Antiferromagnetic to valence-bond-solid transitions in two-dimensional  $su(n)$  heisenberg models with multispin interactions. *Phys. Rev. B*, 80, 2009.
- [109] A. Chaves, F. M. Peeters, G. A. Farias, and M. V. Milošević. Vortex-vortex interaction in bulk superconductors: Ginzburg-landau theory. *Phys. Rev. B*, 83, 2011.
- [110] A. Chaves, private communication.
- [111] E. Babaev, J. Jäykkä, and M. Speight. Magnetic field delocalization and flux inversion in fractional vortices in two-component superconductors. *Phys. Rev. Lett*, 103, 2009.
- [112] Y. Tang and A. W. Sandvik. Quantum monte carlo studies of spinons in one-dimensional spin systems. (in preparation).
- [113] A. W. Sandvik, V. N. Kotov, and O. P. Sushkov. Thermodynamics of a gas of deconfined bosonic spinons in two dimensions. *Phys. Rev. Lett*, 106, 2011.
- [114] N. E. Bonesteel. Valence bonds and the lieb—schultz—mattis theorem. *Phys. Rev. B*, 40, 1989.
- [115] P. Fazekas and P. W. Anderson. On the ground state properties of the anisotropic triangular antiferromagnet. *Philos. Mag*, 30, 1974.
- [116] C. L. Henley. Relaxation time for a dimer covering with height representation. *J. Stat. Phys*, 89, 1997.
- [117] C. L. Henley. From classical to quantum dynamics at rokhsarkivelson points. *J. Phys. Condens. Matt.*, 16, 2004.
- [118] C. Castelnovo, C. Chamon, C. Mudry, and P. Pujol. From quantum mechanics to classical statistical physics: Generalized rokhsarkivelson hamiltonians and the stochastic matrix form decomposition. *Ann. Phys*, 318, 2005.

- [119] M. E. Fisher and J. Stephenson. Statistical mechanics of dimers on a plane lattice. ii. dimer correlations and monomers. *Phys. Rev*, 132, 1963.
- [120] J. Stephenson. Isingmodel spin correlations on the triangular lattice. *J. Math. Phys*, 5, 1964.
- [121] R. Moessner and S. L. Sondhi. Resonating valence bond phase in the triangular lattice quantum dimer model. *Phys. Rev. Lett*, 86, 2001.
- [122] D. Schwandt, M. Mambrini, and D. Poilblanc. Generalized hard-core dimer model approach to low-energy heisenberg frustrated antiferromagnets: General properties and application to the kagome antiferromagnet. *Phys. Rev. B*, 81, 2010.
- [123] K. S. Raman, R. Moessner, and S. L. Sondhi.  $SU(2)$ -invariant spin-1/2 hamiltonians with resonating and other valence bond phases. *Phys. Rev. B*, 72, 2005.
- [124] Y. Tang and A. W. Sandvik. Topological properties of two-dimensional resonating-valence-bond states. *Bull Am. Phys. Soc*, 55, 2010.
- [125] Y. Tang and A. W. Sandvik. Properties of resonating-valence-bond spin liquids and critical dimer models. come back to check to arxiv number!!
- [126] W. Zheng and S. Sachdev. Sine-gordon theory of the non-néel phase of two-dimensional quantum antiferromagnets. *Phys. Rev. B*, 40, 1989.
- [127] L. S. Levitov. Equivalence of the dimer resonating-valence-bond problem to the quantum roughening problem. *Phys. Rev. Lett*, 64, 1990.
- [128] L. B. Ioffe and A. I. Larkin. Superconductivity in the liquid-dimer valence-bond state. *Phys. Rev. B*, 40, 1989.
- [129] H. W. J. Blöte and H. J. Hilhorst. Roughening transitions and the zero-temperature triangular ising antiferromagnet. *J. Phys. A*, 15, 1982.

- [130] B. Nienhuis, H.J. Hilhorst, and H.W. Blöte. Triangular sos models and cubic-crystal shapes,. *J. Phys. A*, 17, 1984.
- [131] S. Papanikolaou, K. S. Raman, and E. Fradkin. Devils staircases, quantum dimer models, and stripe formation in strong coupling models of quantum frustration. *Phys. Rev. B*, 75, 2007.
- [132] E. Fradkin, D. A. Huse, R. Moessner, V. Oganesyan, and S. L. Sondhi. Bipartite rokhsarkivelson points and cantor deconfinement. *Phys. Rev. B*, 69, 2004.
- [133] In the CDM, the monomer distribution is directly given by the "end-end" separation of the loop under construction (i.e., the distance between the two defects introduced). [65,66] In the RVB, the defects generated when making the loops have spin, and the statistics of these spinful defects is not simply related to that of monomers.
- [134] K. S. D. Beach. Master equation approach to computing rvb bond amplitudes. *Phys. Rev. B*, 79, 2009.
- [135] K. S. D. Beach, F. Alet, M. Mambrini, and S. Capponi.  $Su(n)$  heisenberg model on the square lattice: A continuous-n quantum monte carlo study. *Phys. Rev. B*, 80, 2009.
- [136] C. Zeng and C. L. Henley. Zero-temperature phase transitions of an antiferromagnetic ising model of general spin on a triangular lattice. *Phys. Rev. B*, 55, 1997.
- [137] J. L. Jacobsen and J. Kondev. Field theory of compact polymers on the square lattice. *Nucl. Phys. B*, 532, 1998.
- [138] R. Raghavan, C. L. Henley, and S. L. Arouh. New two-color dimer models with critical ground states. *J. Stat. Phys*, 86, 1997.
- [139] C. L. Henley. Random tiling models. In Paul J. Steinhardt David P. DiVincenzo, editor, *Quasicrystals: The state of the art*, pages 429–524. World Scientific, second edition, 1991.

- [140] M. Oxborrow and C. L. Henley. Random square-triangle tilings: A model for twelfefold-symmetric quasicrystals. *Phys. Rev. B*, 48, 1993.
- [141] S. Sachdev. Quantum magnetism and criticality. *Nature Physics*, 4, 2008.
- [142] C. Waldtmann, H. U. Everts, B. Bernu, C. Lhuillier, P. Sindzingre, P. Lecheminant, and L. Pierre. First excitations of the spin 1/2 heisenberg antiferromagnet on the kagome lattice. *Eur. Phys. J. B*, 2, 1998.
- [143] H. C. Jiang, Z. Y. Weng, and D. N. Sheng. Density matrix renormalization group numerical study of the kagome antiferromagnet. *Phys. Rev. Lett*, 101, 2008.
- [144] P. Sindzingre and C. Lhuillier. Low-energy excitations of the kagom antiferromagnet and the spin-gap issue. *Europhys. Lett*, 88, 2009.
- [145] M. Yamashita, N. Nakata, Y. Senshu, M. Nagata, H. M. Yamamoto, R. Kato, T. Shibauchi, and Y. Matsuda. Highly mobile gapless excitations in a two-dimensional candidate quantum spin liquid. *Science*, 328, 2010.
- [146] L. Pauling. The calculation of matrix elements for lewis electronic structures of molecules. *J. Chem. Phys*, 1, 1933.
- [147] L. Hulthén. *Über das austauschproblem eines kristalles*. *Ark. Mat. Astron. Fys*, 26A, 1938.
- [148] J. Wildeboer and A. Seidel. Linear independence of nearest-neighbor valence bond states in several two-dimensional lattices. *Phys. Rev. B*, 83, 2011.
- [149] A. Banerjee, K. Damle, and F. Alet. Impurity spin texture at the critical point between néel-ordered and valence-bond-solid states in two-dimensional  $SU(3)$  quantum antiferromagnets. *Phys. Rev. B*, 83, 2011.
- [150] H. Tran and N. E. Bonesteel. Valence bond entanglement and fluctuations in random singlet phases. *Phys. Rev. B*, 84, 2011.

- [151] J. Lou and A. W. Sandvik. Variational ground states of two-dimensional antiferromagnets in the valence bond basis. *Phys. Rev. B*, 76, 2007.
- [152] M. Havelio and A. Auerbach. Superconductivity and quantum spin disorder in cuprates. *Phys. Rev. Lett*, 83, 1999.
- [153] K. Binder. Finite size scaling analysis of ising model block distribution functions. *Zeitschrift für Physik B: Condensed Matter*, 43, 1981.
- [154] A. W. Sandvik. Computational studies of quantum spin systems. In A. Avella and F. Mancini, editors, *Lectures on the Physics of Strongly Correlated Systems XIV*, volume 1297, pages 135–338, 2010.
- [155] I. Affleck. Critical behavior of two-dimensional systems with continuous symmetries. *Phys. Rev. Lett*, 55, 1985.
- [156] V. E. Korepin. Universality of entropy scaling in one dimensional gapless models. *Phys. Rev. Lett*, 92, 2004.
- [157] P. Calabrese and J. Cardy. Entanglement entropy and quantum field theory. *J. Stat. Mech*, 2004, 2004.
- [158] J. C. Xavier and F. C. Alcaraz. Finite-size corrections of the entanglement entropy of critical quantum chains. *Phys. Rev. B*, 85, 2012.
- [159] A. B. Kallin, I. Gonzalez, M. B. Hastings, and R. G. Melko. Valence bond and von neumann entanglement entropy in heisenberg ladders. *Phys. Rev. Lett*, 103, 2009.
- [160] P. Calabrese, M. Campostrini, F. Essler, and B. Nienhuis. Parity effects in the scaling of block entanglement in gapless spin chains. *Phys. Rev. Lett*, 104, 2010.
- [161] P. Young. Everything you wanted to know about data analysis and fitting but were afraid to ask. arXiv:1210.3781.

- [162] N. Laflorencie, E. S. Sorensen, M. S. Chang, and I. Affleck. Boundary effects in the critical scaling of entanglement entropy in 1d systems. *Phys. Rev. Lett*, 96, 2006.
- [163] P. Lecheminant and H. Nonne. Exotic quantum criticality in one-dimensional coupled dipolar bosons tubes. *Phys. Rev. B*, 85, 2012.
- [164] Daniel Friedan, Zongan Qiu, and Stephen Shenker. Conformal invariance, unitarity, and critical exponents in two dimensions. *Phys. Rev. Lett*, 52, 1984.
- [165] J. Cardy. Continuously varying exponents and the value of the central charge. *J. Phys. A: Math. Gen*, 20, 1987.
- [166] Y.-C. Lin, Y. Tang, J. Lou, and A. W. Sandvik. Correlated valence-bond states. *Phys. Rev. B*, 86, 2012.
- [167] Kedar Damle, Deepak Dhar, and Kabir Ramola. Resonating valence bond wave functions and classical interacting dimer models. *Phys. Rev. Lett*, 108, 2012.
- [168] Y. Huh, P. Strack, and S. Sachdev. Vector boson excitations near deconfined quantum critical points. arXiv:1307.6860.
- [169] D. R. Nelson. In C. Domb and J. L. Lebowitz, editors, *Phase transitions and critical phenomena*, volume 7. Academic Press, London, 1983.
- [170] B. Nienhuis. In C. Domb and J. L. Lebowitz, editors, *Phase transitions and critical phenomena*, volume 11. Academic Press, London, 1987.

## Curriculum Vitae

